PolyPublie
Polytechnique Montréal

POLYTECHNIQUE MONTRÉAL
UNIVERSITÉ D'INGÉNIERIE

Titre: Title:	Experimental Investigation of Linear Angled Arrays of Micro Jets in a Crossflow for Gas Turbine Applications
Auteur: Author:	Taylor Burgunder
Date:	2026
Type:	Mémoire ou thèse / Dissertation or Thesis
Référence: Citation:	Burgunder, T. (2026). Experimental Investigation of Linear Angled Arrays of Micro Jets in a Crossflow for Gas Turbine Applications [Mémoire de maîtrise, Polytechnique Montréal]. PolyPublie. https://publications.polymtl.ca/76506/

Document en libre accès dans PolyPublie
Open Access document in PolyPublie

URL de PolyPublie: PolyPublie URL:	https://publications.polymtl.ca/76506/
Directeurs de recherche: Advisors:	Étienne Robert, & Philippe Versailles
Programme: Program:	Génie aérospatial

Ce fichier a été téléchargé à partir de PolyPublie, le dépôt institutionnel de Polytechnique Montréal
This file has been downloaded from PolyPublie, the institutional repository of Polytechnique Montréal

https://publications.polymtl.ca

POLYTECHNIQUE MONTRÉAL
affiliée à l'Université de Montréal

Experimental Investigation of Linear Angled Arrays of Micro Jets in a Crossflow for Gas Turbine Applications

TAYLOR BURGUNDER
Département de génie mécanique

Mémoire présenté en vue de l'obtention du diplôme de *Maîtrise ès sciences appliquées*
Génie aérospatial

Avril 2026

© Taylor Burgunder, 2026.

POLYTECHNIQUE MONTRÉAL
affiliée à l'Université de Montréal

Ce mémoire intitulé :

Experimental Investigation of Linear Angled Arrays of Micro Jets in a Crossflow for Gas Turbine Applications

présenté par **Taylor BURGUNDER**
en vue de l'obtention du diplôme de *Maîtrise ès sciences appliquées*
a été dûment accepté par le jury d'examen constitué de :

Frédérick GOSSELIN, président
Etienne ROBERT, membre et directeur de recherche
Philippe VERSAILLES, membre et codirecteur de recherche
Patrizio VENA, membre

DEDICATION

À Natacha et ma famille,
merci.

ACKNOWLEDGEMENTS

First and foremost, I express my sincere gratitude to my research supervisor, Etienne Robert, for his guidance and support throughout my master's studies. Beyond providing me with a research topic that perfectly matched the specialization I aimed to pursue, he guided me through the various possible trajectories of the thesis objectives while helping me structure and focus the many directions explored. His mentorship was invaluable not only for the scientific aspects of this work but also for project management. I am deeply grateful for his insightful advice, and the trust he placed in me throughout this research.

My sincere thanks to Professor Philippe Versailles for his valuable assistance with the technical aspects across the different fields covered in this master research. His thoughtful advice and his questions, both challenging and essential, greatly contributed to strengthening the scientific rigor of this work and to deepening my understanding of the studied phenomena.

Special recognition is due to Marie Meulemans for the invaluable support provided during this master's program. I am grateful for her patience in answering my many questions, for her guidance throughout my learning process, and for her coaching during the more challenging moments, without mentioning the countless hours spent together in the laboratory.

I also wish to thank Gabriel Dodier, formerly a master's research student, for his help in getting started with the experimental setup, the associated software tools, and for his constant good humor in the laboratory, which greatly contributed to a motivating work environment.

I acknowledge the collaborators of the Hydromix project, in particular, Marc Füri (Siemens Energy), Professor Bruno Savard (PolyMtl), Dr Gilles Bourques, PhD (McGill), Professor Jeffrey Bergthorson (McGill) and Professor Swetaprovo Chaudhuri (University of Toronto - Institute for Aerospace Research) and the National Research Council (NRC) of Canada for their interest in my work. Their questions regarding methodology, their insights into the physical phenomena involved, and the richness and diversity of their expertise were a significant source of enrichment. The presentations of their respective teams' work fostered engaging discussions on related topics, broadening the scope of this research.

I also thank my colleagues and friends from the LEMUR laboratory for the consistently positive atmosphere, stimulating scientific exchanges, and the many extracurricular activities that made my time during this master's program both enjoyable and memorable.

Finally, I would like to express my deepest gratitude to Natacha for her unwavering support, patience, and understanding since the very beginning of this journey.

RÉSUMÉ

La combustion de l'hydrogène reste limitée industriellement en raison du risque de retour de flamme en configurations prémélangées. Les flammes de diffusion constituent une alternative plus sûre, au détriment des émissions. Le concept de micromélange, basé sur l'injection de micro-jets en écoulement transverse, vise à améliorer le mélange tout en limitant la formation d'oxydes d'azote. Bien que les jets en écoulement transverse soient largement étudiés, les réseaux de multiples micro-jets restent principalement limités à des géométries simples, telles que quelques jets disposés côte à côte ou l'un derrière l'autre. Dans ce contexte, cette étude analyse le mélange d'un alignement d'une ligne de huit jets en écoulement transverse, en faisant varier l'angle d'alignement entre l'écoulement et la ligne de jets. Quatre angles sont considérés (30°, 45°, 60° et 90°), ce dernier servant de référence. Des jets d'un diamètre de 0,7 mm injectent de l'hélium, d'une faible densité pour approcher le comportement de l'hydrogène, dans un écoulement transverse de vitesse $U_\infty = 1.2$ m/s ($Re_\infty = 4060$). Les expériences couvrent des rapports de vitesse $R = 6$ à 13.5, un rapport de densité constant $S = 0.14$, des rapports de quantité de mouvement $J = 5$ à 25 et des nombres de Reynolds de jet $Re_j = 42$ à 96.

Les résultats montrent que le rapport de flux de quantité de mouvement J et l'angle de la ligne de jets gouvernent fortement la dynamique jet–écoulement transversal. L'augmentation de J et la diminution de l'angle renforcent la pénétration des jets et déplacent progressivement le régime dominant d'un comportement de type refroidissement par jet mural vers un mélange plus intense, tout en entraînant la dégradation progressive des grandes structures cohérentes en turbulence à plus petite échelle. La pénétration des jets suit la loi d'échelle attendue en Rd, mais l'angle du réseau introduit un effet de bouclier : des angles plus faibles réduisent l'obstacle frontal pour l'écoulement transversal, ce qui conduit à une pénétration plus profonde et à des interactions jet–jet plus marquées. Les caractéristiques du mélange résultent de ces interactions et la paire de vortex contrarotatifs (CVP). Cette dernière domine le mélange dans le champ lointain, tandis que le mélange proche est retardé par la persistance du coeur des jets marquée pour des J élevés et des angles faibles. En conséquence, la dilution dans le champ lointain est améliorée pour les faibles angles, avec des concentrations plus faibles et une homogénéité spatiale plus uniforme. L'analyse temporelle montre également que les faibles angles suppriment les instabilités périodiques de la couche de cisaillement, conduisant à un mélange plus stable dans le temps, tandis que la CVP reste temporellement stable et favorise un mélange.

ABSTRACT

Hydrogen combustion remains limited in industrial applications due to the risk of flashback in premixed configurations. Diffusion flames offer a safer alternative, at the expense of mixing quality and emissions. The micromix concept, based on the injection of micro-jets in a transverse crossflow, aims to enhance local mixing while limiting nitrogen oxides formation. Although jets in crossflow have been extensively studied, networks of multiple micro-jets remain mostly limited to simple geometries, such as a few jets arranged side-by-side or one behind the other. In this context, the present study analyzes the mixing of a linear array of eight jets in a transverse crossflow, varying the alignment angle between the crossflow and the array of jets. Four angles are considered (30°, 45°, 60°, and 90°), the latter serving as the reference. Jets 0.7 mm in diameter inject helium, used as a hydrogen proxy, into a transverse flow of air at a velocity $U_\infty = 1.2$ m/s ($Re_\infty = 4060$). The experiments cover velocity ratios $R = 6$ to 13.5, a constant density ratio $S = 0.14$, momentum flux ratios $J = 5$ to 25, and jet Reynolds numbers $Re_j = 42$ to 96.

The results show that both the momentum flux ratio J and the array angle strongly govern the jet–crossflow dynamics. Increasing J and lowering the array angle enhances jet penetration and shifts the dominant regime from attached cooling-type jets to strong jet–crossflow mixing, while progressively breaking down large coherent structures into smaller-scale turbulence. Jet penetration follows the expected Rd scaling, but the array angle introduces a shielding effect: lower angles reduce the frontal blockage to the crossflow, resulting in deeper penetration and stronger jet–jet interactions. Mixing characteristics depend on the interplay between these interactions and the counter-rotating vortex pair (CVP). The latter dominated the mixing in the far field, while the near mixing is delayed by a strong potential core at high J and low array angles. Ultimately, the dilution reached is better for lower angles in the far field, with a lower concentration and more uniform spatial homogeneity. Temporal analysis further shows that low array angles suppress periodic shear-layer instabilities, leading to more temporally stable mixing behavior while CVP is time stable, improving the mixing.

TABLE OF CONTENTS

DEDICATION iii

ACKNOWLEDGEMENTS iv

RÉSUMÉ v

ABSTRACT vi

LIST OF TABLES x

LIST OF FIGURES xi

LIST OF ACRONYMS xiv

LIST OF SYMBOLS xvi

CHAPTER 1 INTRODUCTION 1
- 1.1 Energy consumption and global emissions 1
- 1.2 Hydrogen application in industrial gas turbines 2
  - 1.2.1 Gas turbine operation and combustor concepts 2
  - 1.2.2 Pollutant formation 3
  - 1.2.3 Hydrogen versus natural gas combustion characteristics 4
- 1.3 Micromixing technology 5
- 1.4 Research objective 6
- 1.5 Thesis outline 7

CHAPTER 2 LITTERATURE REVIEW 8
- 2.1 Mixing 8
  - 2.1.1 Governing equations and transport of scalars 8
  - 2.1.2 Mixing metrics 9
- 2.2 Single jet in crossflow 11
  - 2.2.1 Jet structure 12
  - 2.2.2 Main parameters 13
  - 2.2.3 Additional influential parameters 16
- 2.3 Multiple jets arrangement 18
  - 2.3.1 Side-by-side configuration 19
  - 2.3.2 Back-to-back configuration 24

2.3.3 Swirling crossflow . . . 27
2.4 Research Gaps . . . 28

CHAPTER 3 METHODOLOGY . . . 29
3.1 Experimental methods . . . 29
3.1.1 Crossflow rig . . . 29
3.1.2 Injection array plates . . . 30
3.2 Particle Image Velocimetry (PIV) . . . 32
3.2.1 Oil droplets seeding . . . 33
3.2.2 Laser sheet: generation, waist and intensity profile . . . 36
3.2.3 Inter-frame delay time . . . 38
3.2.4 Interrogation zone configuration and outlier detection methods . . . 39
3.2.5 Particle density . . . 41
3.3 Flow Characterization . . . 42
3.3.1 Crossflow velocity profile and boundary layer . . . 42
3.3.2 Advection and diffusion regimes . . . 44
3.4 Postprocessing techniques . . . 45
3.4.1 Frame intensity correction . . . 45
3.4.2 Operations on images . . . 45
3.4.3 3D Reconstruction . . . 47
3.4.4 Unmixedness parameter . . . 48
3.4.5 POD and spectral analysis . . . 49
3.5 Parameter space covered . . . 50

CHAPTER 4 RESULTS & DISCUSSION . . . 52
4.1 Qualitative assessment of the jets–crossflow interaction . . . 52
4.1.1 Profile view . . . 52
4.1.2 Top view . . . 54
4.1.3 Front view . . . 56
4.2 3D reconstruction . . . 57
4.3 Jet penetration . . . 59
4.3.1 Penetration along the arrays . . . 59
4.3.2 Influence of the array angle . . . 61
4.3.3 Influence of the momentum flux ratio . . . 63
4.4 Velocity field analysis . . . 68
4.4.1 Streamlines of the flow . . . 68
4.4.2 Reverse flow and recirculation zones . . . 69

4.5 Jet–crossflow mixing 73
4.5.1 Mixing field 74
4.5.2 Mixing Variation 83

CHAPTER 5 CONCLUSION 90
5.1 Summary 90
5.2 Design rules for enhanced mixing 91
5.3 Future Research 92

REFERENCES 94

LIST OF TABLES

Table 1.1	Comparison of key combustion properties of hydrogen and methane .	4
Table 3.1	Jet flow and crossflow parameters with the corresponding non-dimensional ratios	30
Table 3.2	Jet spacings s_x/d and s_y/d and swirl number Sw evolution across the array angles	32
Table 3.3	Slice positions for front, profile and top planes of view	51

LIST OF FIGURES

Figure 1.1	Growth rate of the annual global mean atmospheric CO_2	2
Figure 1.2	Schematic representation of a gas turbine	3
Figure 1.3	Schematic and photographic views of the micromix burner geometry developed at Aachen University.	5
Figure 2.1	Three possible mixing states for a "black" scalar ($\phi = 1$) with diffusivity D mixed with a "white" fluid ($\phi = 0$) within a closed system	10
Figure 2.2	Three examples of jets in crossflow observed in nature and engineering	11
Figure 2.3	Main structures of a JICF	12
Figure 2.4	Jet trajectories for various R.	14
Figure 2.5	Schematic representation of the double-deck structure induced by a rectangular jet exit.	17
Figure 2.6	Windward and leeward edges of a nitrogen jet into an air crossflow for $R = 10$.	19
Figure 2.7	Instantaneous laser-induced fluorescence images of a single and twin JICFs	20
Figure 2.8	Cross-sectional images and schematic of vortex structures for side-by-side jets in crossflow	21
Figure 2.9	Cross-sectional average streamlines of the flow at $x/d = 4$ downstream of the jet exit for side-by-side jets	22
Figure 2.10	Comparison of mean jet trajectories determined from PIV measurements for parallel TJICF	23
Figure 2.11	Streamwise velocity fields and corresponding streamlines for a single jet and tandem jets	25
Figure 2.12	Concentration evolution for different tandem jet configurations	26
Figure 3.1	Experimental setup rig	29
Figure 3.2	Piping and instrumentation diagram	31
Figure 3.3	Experimental setup with laser representation within the profile view configuration	31
Figure 3.4	Injection configurations of the linear jet arrays	32
Figure 3.5	Schematic comparison of the fluid motion, the actual particle response, and the particle trajectory estimated by the measurement technique	34
Figure 3.6	Characterization of the laser sheet geometry and intensity distribution	37

Figure 3.7 Crossflow velocity profiles and their sensitivity for different inter-frame delay time 39
Figure 3.8 Illustration of the cross-correlation process used in PIV 40
Figure 3.9 Schematic representation of boundary layer theory showing laminar-to-turbulent transition and the associated velocity profile 43
Figure 3.10 Measured crossflow velocity profile at the jet exit and averaged along the linear array 44
Figure 3.11 Centerline extraction from time-averaged velocity fields for all array angles at the 5^{th} jet exit for $J = 25$ 46
Figure 3.12 Spread calculation illustration from time-averaged intensity fields for the 90° case on at the 5^{th} jet exit and $J = 25$ 47
Figure 3.13 Concept of Proper Orthogonal Decomposition (POD) 49
Figure 4.1 Typical profile view of JICF for the 5th jet of the 90° angle array. Positions of KH instabilities and the CVP are shown qualitatively . . 52
Figure 4.2 Instantaneous flow profiles in the xz-plane for different array angles and momentum flux ratios (J) 53
Figure 4.3 Instantaneous top view ($xy-$plane) at various heights for different array angles at $J = 10$ 55
Figure 4.4 Instantaneous front views at various axial positions for different array angles at $J = 10$. 56
Figure 4.5 3D reconstruction of the time-average intensity fields and the recirculation zones 58
Figure 4.6 Time-averaged images of the 5^{th} jet of the array for different injection angles at $J = 25$. 60
Figure 4.7 Fittings of the jet centerline penetration measured at each jet exit . . 61
Figure 4.8 Comparison of centerline trajectories in the plane aligned with jet #5 for different array angles and momentum flux ratios ($J = 5$ to 25) . . 62
Figure 4.9 Centerline trajectories in the plane aligned with jet #5 for the 30° array, for momentum flux ratios $J = 5$–25 64
Figure 4.10 Scaled trajectories of the 5^{th} jet across different array angles and momentum ratios J 66
Figure 4.11 Evolution of the scaling coefficients A and B for the different trajectory scalings (d, Rd, Jd) as functions of the array angle and J 67
Figure 4.12 Top-view time-averaged streamlines overlaid on an instantaneous corresponding image at $z/d = 7$ for $J = 25$ and all array angles. 69

Figure 4.13 3D reconstruction of the time-averaged recirculation zone at $J = 25$ for all array angles. The color map represents the vertical velocity component, w. 70
Figure 4.14 Recirculation area in the xz-plane as a function of the spanwise position (y) for different angles and values of J. The area is normalized by that of the 90° case at $J = 25$. 72
Figure 4.15 Time-averaged images of the 5^{th} jet exit plane at $J = 25$ for the different array angles. The jet centerline (red) and the intensity distributions measured along the normals to the centerline (yellow) are shown for $J = 25$. 75
Figure 4.16 Intensity distributions measured at $J = 25$ along the normals to the centerline of the 5^{th} jet for all array angles. 76
Figure 4.17 Spread along the downstream distance for angles and J 78
Figure 4.18 $Rd-$scaled spread along the downstream distance for angles and J . . 79
Figure 4.19 Evolution of the normalized maximal intensity per branch along the centerline coordinate ξ 80
Figure 4.20 Spatial evolution of the time-averaged unmixedness parameter $\mathcal{U}_{yz}$ computed over cross-sections in the yz-plane for the 90° array configuration 83
Figure 4.21 Spatial evolution of the time-average unmixedness parameter, $\mathcal{U}_{yz}$, calculated over cross sections (yz-plane) for all array angles at $J = 5$ and 20 84
Figure 4.22 Temporal fluctuations and the associated spectrum of the unmixedness parameter evaluated at various downstream positions for the 90° configuration and for $J = 5$ and 20 86
Figure 4.23 POD spatial modes with their associated spectrum for the 90° array at $J = 5$ from a profile view 87
Figure 4.24 Spectrum of the unmixedmess parameter evaluated on the cross section $x/d = 8.5$ for $J = 5$ and 20 across all configurations 88

LIST OF ACRONYMS

CH_4 Methane

CO Carbon Monoxide

CO_2 Carbon Dioxide

CVP Counter-rotating Vortex Pair

DEHS Di-Ethyl-Hexyl-Sebacate

DLE Dry Low Emission

FFT Fast Fourier Transform

FWHM Full Width at Half of the Maximum

FWTM Full Width at 10% of the Maximum

GAW Global Atmosphere Watch

GDP Gross Domestic Product

He Helium

H_2 Hydrogen

JICF Jet In Cross-Flow

KH Kelvin-Helmholtz

LES Large Eddy Simulation

LIF Laser Induced Fluorescence

N_2O Nitrous Oxide

NO_x Nitrogen Oxides

OEMs Original Equipment Manufacturers

PIV Particle Image Velocimetry

POD Proper Orthogonal Decomposition

ppp Particles Per Pixel

RMS Root Mean Square

RQL Rich-Quench-Lean

RT Rayleigh-Taylor

SJICF Single Jet In a Cross-Flow

SO_x Sulfur Oxides

STP Standard Temperature and Pressure

TJICF Twin Jets In a Cross-Flow

UHC Unburned Hydrocarbons

WLE Wet Low Emission

WMO World Meteorological Organization

WVP Windward Vortex Pair

LIST OF SYMBOLS

Symbol	Description	Unit
A	Trajectory scaling factor	∅
AR	Jet exit aspect ratio	∅
A_r^*	Normalized recirculation zone	∅
α	Intensity decay rate	∅
B	Trajectory curvature exponent	∅
C	Jet spacing–momentum parameter	∅
C_c	Cunningham slip factor	∅
D	Molecular diffusivity	[m^2/s]
d	Jet diameter	[m]
d_p	Particle diameter	[m]
d_∞	Molecular diameter of air	[m]
δ	Boundary layer height	[m]
δ_t	Inter-frame delay time	[s]
f	Focal length	[m]
H	Duct height	[m]
I	Pixel light intensity	∅
J	Jet-to-crossflow momentum flux ratio	∅
Kn	Knudsen number	∅
L	Core length of the intensity decay	[m]
L_c	Characteristic flow length scale	[m]
L_S	Stroke length	[m]
$\mathcal{L}$	Mean free path of gas molecules	[m]
l	Needle length	[m]
λ	Wavelength	[m]
M	Molar mass	[kg/mol]
$\dot{m}$	Mass flow rate	[kg/s]
μ	Dynamic viscosity	[Pa s]
N_{ppp}	Number of particles per pixel	∅
n	Molecular number density	[m^{-3}]
$\mathcal{N}_\mathrm{A}$	Avogadro number	[mol^{-1}]
ν	Kinematic viscosity	[m^2/s]
Pe	Péclet number	∅

R	Jet-to-crossflow velocity ratio	$\varnothing$
Re_j	Jet Reynolds number	$\varnothing$
Re_∞	Crossflow Reynolds number	$\varnothing$
Re_p	Particle Reynolds number	$\varnothing$
Ro	Rossby number	$\varnothing$
ρ_j	Jet density	[kg/m^3]
ρ_∞	Crossflow density	[kg/m^3]
ρ_p	Particle density	[kg/m^3]
S	Jet-to-crossflow density ratio	$\varnothing$
s	Jet spacing	[m]
Sc	Schmidt number	$\varnothing$
St	Strouhal number	$\varnothing$
Stk	Stokes number	$\varnothing$
Sw	Swirl number	$\varnothing$
σ	Root mean square	Undefined
τ	Characteristic time	[s]
$\mathcal{U}$	Unmixedness parameter	$\varnothing$
U_j	Streamwise jet velocity	[m/s]
U_∞	Streamwise crossflow velocity	[m/s]
$\mathbf{u} = (u, v, w)$	Velocity vector and its cartesian components	[m/s]
V_θ	Tangential velocity	[m/s]
ϕ	Scalar field	$\varnothing$
Ω	Angular velocity	[rad/s]
ω	Source term	Undefined
(x, y, z)	Cartesian coordinate system	[m]
(ξ, w)	Centerline coordinate system in the xz-plane	[m]

CHAPTER 1 INTRODUCTION

1.1 Energy consumption and global emissions

In 2024, 87% of the global demand for energy is still met by fossil fuels such as coal, oil, and natural gas [1]. These energy sources have historically enabled rapid industrial expansion and improvements in living standards, owing to their high energy density and the ease of storage. However, their combustion releases large amounts of Carbon Dioxide (CO_2), the dominant greenhouse gas, responsible for nearly 79% of anthropogenic global emissions, followed by Methane (CH_4) (19%) and Nitrous Oxide (N_2O) (4%) [2]. The World Meteorological Organization (WMO), through its Global Atmosphere Watch (GAW) scientific program, reported that CO_2 concentrations have continued to rise in recent years, with average growth rates of 1–2 ppm per year, as shown in Fig. 1.1 [3]. In addition to CO_2, fossil fuel combustion also produces substantial amounts of Nitrogen Oxides (NO_x), N_2O, Sulfur Oxides (SO_x), Unburned Hydrocarbons (UHC), such as CH_4, and particulate matter. All of these contribute to air pollution and have significant impacts on human health, ecosystems and the economy, with a relative cost of 6% to the world Gross Domestic Product (GDP) [4]. Notably, the social costs of the main greenhouse gases have been calculated per tonne emitted into the atmosphere, amounting to US$185 for CO_2, US$2,000 for CH_4, and US$65,000 for N_2O in 2020 [5–7]. The power generation sector, dominated by fossil-fuel power plants, is a major contributor: gas-fired plants remain central in the global electricity mix, with gas turbines widely used for both baseload and peaking power due to their flexibility and efficiency [8]. Recognizing these environmental impacts, international regulations have set reduction targets, such as the Göteborg Protocol, which requires a 42% reduction in NO_x and 58% reduction in SO_x emissions by 2035 relative to 2005 levels [9].

Following this dynamic, a transition towards cleaner power generation is essential. Hydrogen (H_2) has emerged as a promising alternative to fossil fuels for gas turbines, as its combustion does not produce CO_2. However, the so-called hydrogen economy must be carefully evaluated, depending on the method of hydrogen production. In 2021, only 0.04% of the total hydrogen used was produced via water electrolysis using renewable energy, while 83% was derived from fossil fuels [10, 11].

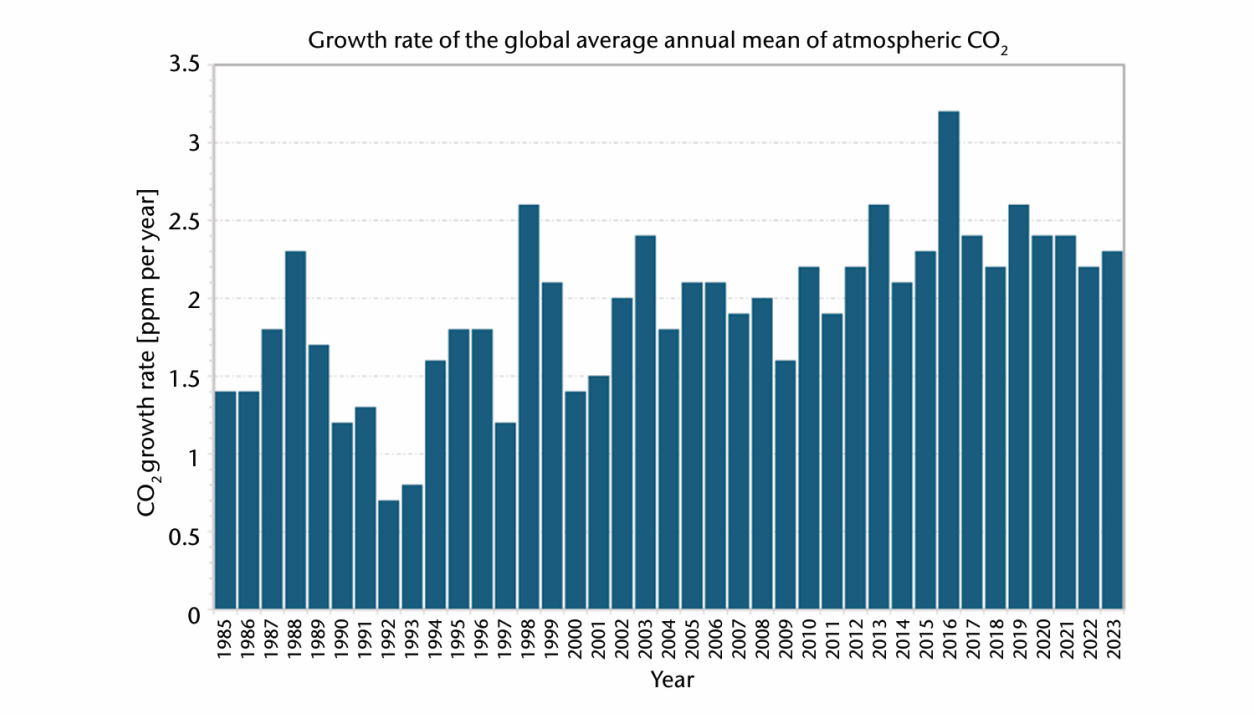


Figure 1.1 Growth rate of the annual global mean atmospheric CO_2, calculated from WMO GAW network observations for 1985–2023, with permission [3]

1.2 Hydrogen application in industrial gas turbines

Beyond production and supply considerations, the integration of hydrogen into industrial gas turbines raises significant challenges regarding combustion dynamics, pollutant formation, and system stability.

1.2.1 Gas turbine operation and combustor concepts

Modern stationary gas turbines, whether aeroderivative (gas turbines initially developped for aircraft jet engine propulsion and adapted for industrial and power-generation use) or heavy-duty industrial machines, are based on the same thermodynamic principle. A schematic representation is presented in Fig. 1.2. Compressed air is first delivered by a multi-stage compressor, then mixed with fuel and burnt in the combustion chamber. The resulting high-temperature gases expand through the turbine, where part of their energy is redirected through the shaft to drive the compressor. The remaining energy released by the combustion is converted either into mechanical power, as in turboshafts and turboprops, or into thrust by accelerating the exhaust gases, as in turbojets and turbofans for aeronautical applications.

Continuous improvements have shaped gas turbine design over the decades, including ad-

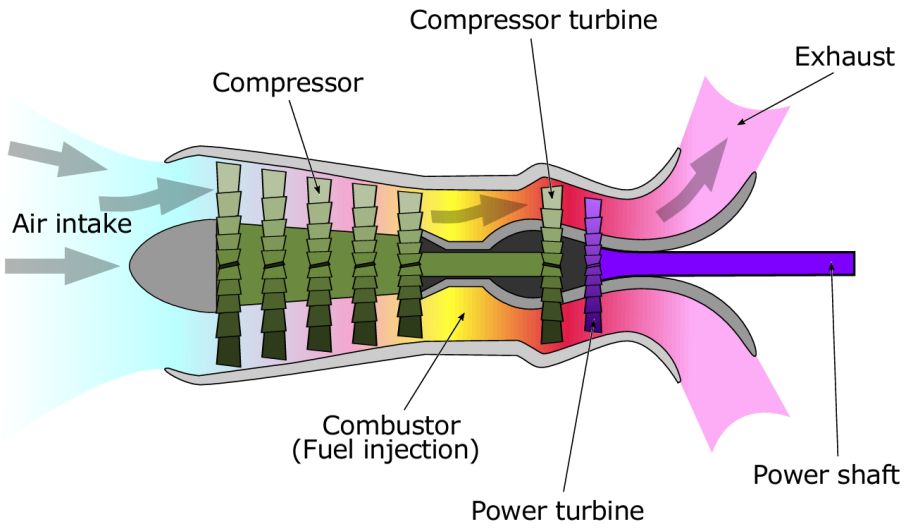


Figure 1.2 Schematic representation of a gas turbine, adapted from Wikimedia Commons, CC BY 4.0

vanced airfoil aerodynamics, multi-stage high-pressure compressors and turbines, cooling technologies, and cycle innovations such as gas pre-heating or reheating. Nevertheless, the combustion chamber remains the most critical component, both for performance and for compliance with emission regulations. To meet these requirements, various combustor architectures have been developed: Dry Low Emission (DLE) systems relying on lean premixing, Wet Low Emission (WLE) concepts based on water or steam injection, sequential (two-stage) combustion, such as Rich-Quench-Lean (RQL) staging, for reduced pollutant formation and improved performance [12]. Each of these strategies aims at shaping the temperature distribution, since this parameter largely dictates the level of NO_x formed during combustion.

1.2.2 Pollutant formation

Pollutants formation in gas turbines is primarily governed by flame temperature and by the spatial and time distribution of the fuel–air mixture. Incomplete combustion occurring in fuel-rich regions can lead to the formation of Carbon Monoxide (CO) and unburned fuel when hydrocarbons are used. NO_x emissions arise primarily from the thermal (Zeldovich) mechanism, which involves the dissociation of the strong triple bond of molecular nitrogen at high temperatures [12]. Consequently, localized hot spots or near-stoichiometric regions play a decisive role in increasing NO_x production. This explains why premixed combustors operated with lean mixtures, which promote a more homogeneous temperature field, generally lead to lower NO_x emissions. In contrast, non-premixed configurations tend to produce locally

rich zones and higher temperature gradients, which are associated with increased pollutant formation [12].

Alternative approaches aim at reducing the effective flame temperature or the residence time of gases in high-temperature regions. For instance, WLE systems inject water or steam to absorb heat and lower the peak temperature of the flame. Sequential or staged combustors split the combustion process into multiple steps separated by intermediate cooling, which reduces the residence time during which the gases remain at high temperature and consequently limits NO_x formation.

1.2.3 Hydrogen versus natural gas combustion characteristics

H_2 exhibits combustion characteristics that differ strongly from methane and other hydrocarbons traditionally used in gas turbines. Its lower volumetric energy density, $11\,\mathrm{MJ/m^3}$ for hydrogen compared to about $35\,\mathrm{MJ/m^3}$ for natural gas at $P = 1\,\mathrm{atm}$ and $T = 0\,^{\circ}\mathrm{C}$ [14], implies that significantly larger storage volumes and higher compression pressures are required to store equivalent amounts of energy. This limitation complicates storage and transport, thereby making stationary power generation a more practical application than transportation for H_2 usage [15]. Furthermore, its wide flammability range ($4.1 - 75\%$ vol. for hydrogen with air vs. $5.3 - 15\%$ for methane with air at Standard Temperature and Pressure (STP) $T = 298\,\mathrm{K}$ and $P = 1\,\mathrm{atm}$ [16]) and high laminar flame speed ($3.1\,\mathrm{m/s}$ vs. $0.4\,\mathrm{m/s}$ for methane at stoichiometric conditions [13]) render hydrogen flames more prone to flashback, (*i.e.* the upstream propagation of the flame into the premixing section when the local flow velocity falls below the flame speed) and thermo-acoustic instabilities (*i.e.* self-excited pressure oscillations resulting from constructive coupling between unsteady heat release and acoustic waves in the combustion chamber) especially in premixed combustors [12]. Hydrogen also has a low ignition energy and high diffusivity, which on one hand facilitates rapid mixing and ignition, but on the other hand makes the flame more susceptible to uncontrolled igni-

Table 1.1 Comparison of key combustion properties of hydrogen and methane [13]

Properties	**Hydrogen (H_2)**	**Methane (CH_4)**
Lower heating value [MJ/kg]	120	48
Lower heating value [MJ/m^3]	11	35
Density at STP [kg/m^3]	0.09	0.72
Flammability limits in air [vol.%]	4.1–75	5.3–15
Laminar flame speed at stoichiometry [m/s]	3.1	0.4
Ignition energy [mJ]	0.02	0.28
Diffusion coefficient [cm^2/s]	0.61	0.16

tion events and local instabilities [12]. The hydrogen and methane properties are listed in Tab. 1.1 [13].

These properties impose significant constraints on the design of hydrogen-fueled gas turbines. Conventional lean premixed flames, which are widely used to achieve low NO_x emissions in natural-gas turbines, become difficult to stabilize without risking flashback into the injection system. This has motivated extensive research into alternative burner concepts, such as staged combustion, distributed injection, and micromix technology which aim to maintain locally lean conditions, enhance fuel–air mixing, and mitigate the risk of flashback, while still ensuring a sufficient level of mixing to limit pollutant formation.

1.3 Micromixing technology

The micromix concept relies on arrays of small injectors (typically with jet diameters $d < 1$ mm), as illustrated in Fig. 1.3. In this configuration, the fuel is injected perpendicularly into the main oxidizer stream through the Jet In Cross-Flow (JICF) approach, generating strong shear layers and characteristic vortical structures that promote rapid and intense mixing. The spatial separation of the reactants prior to mixing inherently mitigates the risk of flashback. However, pollutant formation then depends strongly on the rapidity and uniformity of the mixing process.

Reducing the jet diameter enhances the mixing efficiency while simultaneously decreasing the residence time at high temperatures, thereby limiting NO_x formation [18]. However, excessively small jets may lead to increased flame instability, indicating the existence of an optimal injector scale [19]. Promising experimental results have demonstrated that hydrogen

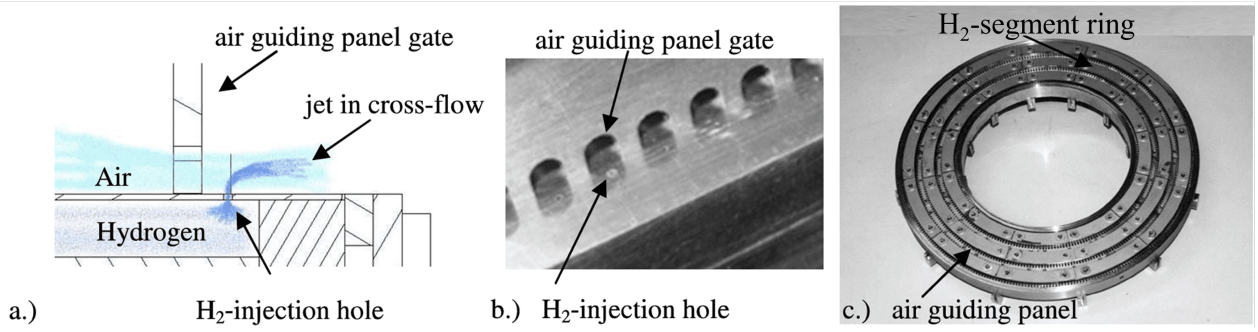


Figure 1.3 Schematic and photographic views of the micromix burner geometry developed at Aachen University. (a) Schematic of the hydrogen jet in crossflow. (b) Close-up of hydrogen injection holes and air guiding panels. (c) Overall view of the annular micromix injection system; adapted with permission [17]

micromix combustors, operating with jet diameters below one millimeter, achieved NO_x emissions as low as 2.5 ppm (corrected at 15 vol.% O_2) [20].

Despite this potential, relatively little research has been devoted to micromixing combustors for hydrogen applications. The existing literature remains limited, particularly from an experimental perspective, where the characterization of mixing processes and flow interactions within injector arrays is still scarce. Moreover, even fewer studies address the problem from a fundamental standpoint, focusing on the underlying fluid-mechanical mechanisms governing mixing and jet interactions. Previous work by G. Dodier [21] has highlighted the importance of geometric parameters in micromix injector configurations. In particular, it was shown that the spacing between jets in an array perpendicular to the crossflow direction, can significantly influence both the mixing efficiency and the interaction between neighboring jets. These interactions directly affect the development of the flow field and the resulting scalar transport [21].

However, while the role of jet spacing has been investigated, other key geometric parameters remain largely unexplored in micromix configurations. In particular, the influence of the jet array angle relative to the crossflow has received little attention, despite its potential impact on jet interaction, mixing enhancement, and overall injector performance. Addressing this question therefore represents an important step toward a deeper understanding of micromixing mechanisms in multi-jet injector configurations.

1.4 Research objective

Building on the context presented above, the present work aims to experimentally investigate the influence of the array angle on the mixing behavior of low-density micro-jet arrays discharged into a crossflow. In this configuration, the jets are arranged in arrays oriented at prescribed angles relative to the crossflow direction. The study focuses on the fundamental investigation of the jet–crossflow and jet–jet interactions arising in these configurations and their impact on the mixing process. To characterize the mixing, several metrics are employed, including jet penetration, velocity fields, jet dilution and spatial and temporal mixing uniformity. The analysis is conducted over a range of jet-to-crossflow momentum ratios in order to encompass different regimes relevant to practical applications, from film cooling to rapid mixing.

1.5 Thesis outline

This master's thesis begins with a review of mixing phenomena, examining both large- and small-scale structures, and discussing the respective roles of diffusivity and advection. Metrics commonly used to quantify mixing are introduced, providing the foundation for subsequent analyses. The review then turns to previous works on JICF, before extending the discussion to multiple-jet arrangements. The following chapter describes the experimental methodology, including the jet geometries investigated. Particular emphasis is placed on laser-based optical diagnostics, such as Particle Image Velocimetry (PIV), as well as on the post-processing techniques employed to extract relevant flow and mixing parameters. The results are organized into four main parts. Firstly, a description of the jet structures into the crossflow across the different injection configuration is provided. Secondly, jet trajectories are examined for the different injector configurations and compared with reference data from the literature. Thirdly, velocity-field analyses are conducted to understand flow dynamics. Finally, the mixing performance is quantified across the various geometries, such as the jet spread downstream and the jet intensity decay. A particular attention is applied to the spatio-temporal variations of the mixing. The key findings are summarized in the conclusion, highlighting the influence of multi-jet arrangements on jet–crossflow interactions and mixing efficiency. Design guidelines and recommendations for future research are also provided to enhance hydrogen micromixing. In particular, these guidelines serve as a valuable resource for Original Equipment Manufacturers (OEMs), highlighting the practical relevance of the different injector configurations.

CHAPTER 2 LITTERATURE REVIEW

2.1 Mixing

Mixing processes play a central role in fluid mechanics and combustion, as they govern how momentum, energy, and scalars such as species concentrations are distributed within a flow. In the context of jet-in-crossflow configurations, understanding the underlying mechanisms of mixing is essential to control flame stability, pollutant formation, and overall system efficiency. This section first recalls the governing equations of fluid motion and scalar transport, from which the relevant dimensionless parameters controlling mixing behavior are derived. Particular emphasis is given to the interplay between advection and diffusion processes, which respectively govern macroscopic mixing through large-scale transport and microscopic mixing through molecular diffusion. Finally, the main quantitative metrics used to characterize mixing are introduced, enabling comparison across different flow conditions and injector designs.

2.1.1 Governing equations and transport of scalars

Mixing processes in turbulent flows can be described starting from the transport equation for a scalar field ϕ, such as species concentration or temperature. The scalar transport (i.e. convection) equation reads:

$$\frac{\partial(\rho\phi)}{\partial t} + \nabla \cdot (\rho \mathbf{u}\phi) = \nabla \cdot (\rho D \nabla \phi) + \dot{\omega}_\phi, \tag{2.1}$$

where ρ is the local density, $\mathbf{u}$ the local velocity vector, D the molecular diffusivity of the scalar in its environment, and $\dot{\omega}_\phi$ a source term accounting for chemical production or destruction. Since the current study is non-reactive, $\dot{\omega}_\phi = 0$. The left-hand side describes advection, characterizing the transport of the scalar by the bulk motion of the fluid itself, while the right-hand side accounts for diffusion, which tends to homogenize concentration gradients, starting at molecular scales. These two mechanisms, advection and diffusion, govern the mixing process. The Péclet number, Pe, defined as the ratio of advection to molecular diffusion in scalar transport in Eq. 2.2, indicates which phenomenon dominates:

$$Pe = \frac{\tau_{\text{diff}}}{\tau_{\text{adv}}} = \frac{U L_c}{D} = Re \times Sc, \tag{2.2}$$

where τ_{diff} and τ_{adv} are respectively the characteristic time of diffusion and advection, and U and L_c denote characteristic velocity and length scales, respectively. A large Pe signifies that advection prevails over diffusion. The Péclet number can be expressed by the product of the Reynolds number Re and the Schmidt number Sc that are commonly employed in gas turbine studies. In most engineering flows, such as JICF, Sc, is on the order of unity leading to a large Péclet number ($Pe \gg 1$) implying that advection dominates in mixing [22,23]. However, for very light species such as hydrogen, diffusion can still play a noticeable role, particularly near the jet exit region and within small-scale turbulent structures [24,25]. Indeed, hydrogen exhibits much higher molecular diffusivity than heavier gases, leading to lower Péclet numbers and consequently enhanced diffusive transport relative to momentum. At STP, the molecular diffusivity of hydrogen in air is $D_{\text{H}_2\text{-Air}} \approx 0.61$ cm^2/s [26], which is approximately four times that of methane in air, $D_{\text{CH}_4\text{-Air}} \approx 0.16$ cm^2/s [27].

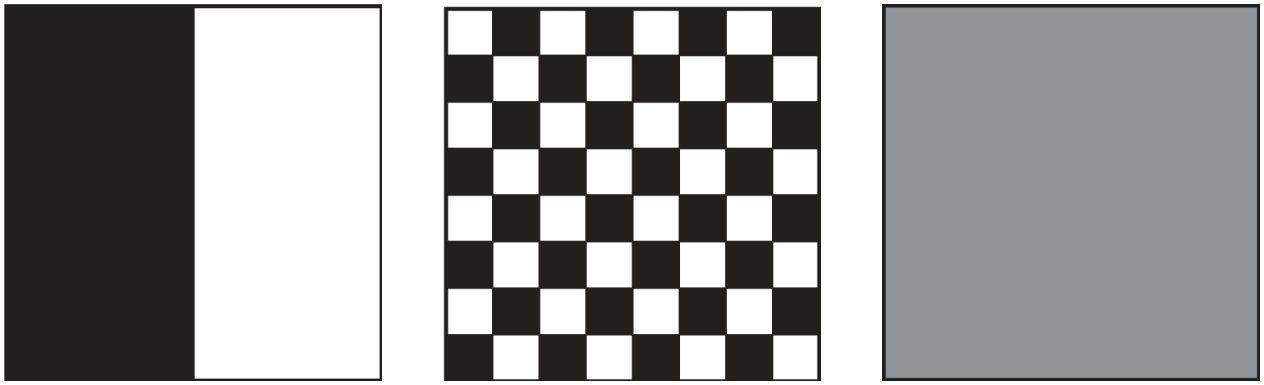
Turbulent Diffusion

Turbulent flows enhance mixing by increasing the effective diffusivity of scalar quantities beyond their molecular value, a phenomenon commonly referred to as turbulent diffusion. The turbulent diffusivity, D_t, accounts for the mean, macroscopic transport of scalars induced by velocity fluctuations, yielding an effective diffusivity $D_{\text{eff}} = D + D_t$ [28]. Higher turbulence intensity amplifies the fluctuating velocity components, thereby increasing D_t and accelerating scalar homogenization throughout the flow [29,30]. In high-Re and high-Pe flows, scalar transport is dominated by advection and turbulent fluctuations, while molecular diffusion plays a negligible role at macroscopic scales [29]. In such flows, mixing proceeds through a cascade of turbulent eddies, progressively transferring scalar fluctuations from large to smaller scales, where molecular diffusion ultimately smooths the scalar field; this effect is particularly pronounced for high-Sc fluids [30]. Turbulence theory also supports this view, with Tennekes & Lumley [31] showing that turbulent diffusivity D_t can exceed D by several orders of magnitude, highlighting the dominant role of turbulent transport in practical engineering flows such as jets in crossflow and combustors. Consequently, effective mixing in these flows is primarily controlled by turbulence intensity, eddy structures, and coherent vortical motions, with molecular diffusion serving only as a fine-scale smoothing mechanism.

2.1.2 Mixing metrics

Quantifying mixing in JICF requires a proper definition of a normalized scalar field ϕ, where $\phi = 1$ represents pure jet fluid, $\phi = 0$ pure crossflow fluid, and intermediate values indicate partial local mixing. Hewes and Mydlarski [32] illustrate different mixing states in a scalar

field in Fig. 2.1: (a) a fully unmixed state where the fluids are completely separated, (b) a stirred state with zero molecular diffusivity ($D = 0$), and (c) a fully mixed state where molecular diffusion ($D > 0$) has acted to homogenize the scalar field.



(a) Initial condition (b) Intermediate state (c) Fully mixed state

Figure 2.1 Three possible mixing states for a "black" scalar ($\phi = 1$) with diffusivity D mixed with a "white" fluid ($\phi = 0$) within a closed system: (a) initial condition; (b) intermediate state; (c) fully mixed state; with permission [32]

Variance-based mixing metrics

A common approach to characterize the mixing state is via the scalar variance $\phi'^2 = (\phi - \overline{\phi})^2$, where ϕ is the local scalar value and $\overline{\phi}$ its mean over a defined neighborhood or temporal ensemble. A classical metric derived from the variance is the intensity of segregation I_s, introduced by Danckwerts [33]. It is defined as the ratio of the variance at a given time, σ^2, to the initial variance at $t = 0$ s, σ_0^2: $I_s = \sigma^2/\sigma_0^2$.

Although widely used in closed systems, such as tank mixing applications, this measure strongly depends on the initial conditions and is therefore less suitable for open reactors, where the initial global scalar value is not representative of the final mixed state, as in jet-in-crossflow configurations [34]. To have a degree of mixing field for combustion purposes, the coefficient of variation $\phi'^2/\overline{\phi}$ can be used [35]. However, the scalar variance has a theoretical upper bound given by $\phi'^2 \leq \overline{\phi}(1-\overline{\phi})$, corresponding to a binary (fully segregated) field. When scaled by the mean scalar, the coefficient of variation is thus bounded by $0 \leq \phi'^2/\overline{\phi} \leq 1 - \overline{\phi}$. Although this metric reflects the degree of inhomogeneity, its upper limit depends on the mean scalar $\overline{\phi}$, making it less suitable for comparing mixing states across regions or flow

conditions. In contrast, the normalized variance, or unmixedness parameter [32, 36, 37]:

$$\mathcal{U} = \frac{\phi'^2}{\overline{\phi}(1-\overline{\phi})}, \tag{2.3}$$

is bounded between 0 (perfectly mixed) and 1 (completely segregated), providing a consistent and dimensionless measure of mixing. For instance, this parameter has been used to evaluate the evolution of the mixing quality along the downstream distance of a JICF [37, 38]. It has been shown that the unmixedness parameter effectively captures the enhanced local mixing induced by Kelvin–Helmholtz instabilities at the jet–crossflow interface [38]. An equivalent formulation based on mass has also been applied in gas turbine studies, where it has been shown that lower unmixedness values correlate with reduced local temperatures and, consequently, lower thermal NO_x formation [39].

2.2 Single jet in crossflow

The JICF configuration is widely encountered in fluid mechanics and occurs when a smaller jet interacts with a larger transverse flow. It has been extensively studied due to its relevance in a wide range of engineering applications. Figure 2.2 illustrates several examples, including exhaust gas dispersion from smokestacks, volcanic eruptions, and industrial applications, such as gas turbines. Jets in crossflow are used for cooling high-pressure turbine blades and for mixing fuel and air either prior to the main combustion process or within staged combustion systems, such as rich–quench–lean combustors.



(a) (b) (c)

Figure 2.2 Three examples of jets in crossflow observed in nature and engineering: (a) volcanic smoke, (b) smoke rising from an industrial smokestack, and (c) film cooling of turbine blades; in open access [40, 41]

2.2.1 Jet structure

In the canonical configuration of a jet issuing into a transverse crossflow, a rich hierarchy of coherent vortical structures develops due to the strong shear and three-dimensional interaction between the jet and the cross-flow boundary layer. These multiscale structures, shown in Fig 2.3, are described as follows :

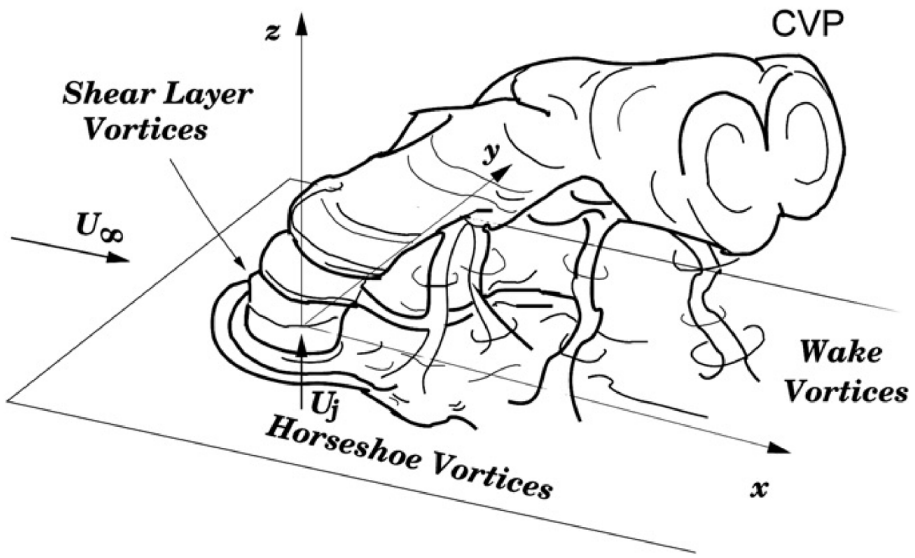


Figure 2.3 Main structures of a JICF showing key flow features such as the jet core, shear layers, and vortical structures; adapted with permission from [42]

- The dominant flow structure downstream of a jet of diameter d is the Counter-rotating Vortex Pair (CVP), which originates in the near field of the jet wake, defined as the region where $x/d \lesssim 3$, due to distortions in the shear layer. The CVP then persists and convects downstream along the jet trajectory, thereby enhancing the overall mixing efficiency [43]. It governs the jet–crossflow interaction in the far field, typically defined for $x/d \gtrsim 3$ [44], yet remains strongly influenced by near-field conditions, including vortical structures within the jet orifice that may induce constructive or destructive interactions affecting the coherence of the CVP [45].

- Upstream of the jet exit in the crossflow, horseshoe vortices develop as the crossflow boundary layer interacts with the jet orifice, separates, and wraps around the jet base. The structure adopts a horizontal U-shape around the jet, with side extensions stretching downstream within the crossflow. This horseshoe vortex is generally considered a weak structure, contributing only marginally to the overall jet–crossflow

interaction [46]. Depending on the flow conditions, it may exhibit steady, oscillatory, or coalescing behavior [42, 47].

- Along the windward shear layer of the jet, the velocity discontinuity between the jet and the crossflow induces Kelvin–Helmholtz instabilities. The latter promote the formation of coherent vortical structures, typically in the form of vortex rings or hairpin vortices, which undergo rapid roll-up, entrain crossflow fluid, and transfer vorticity into larger-scale structures [42,45,47]. The dynamics of these shear-layer instabilities are inherently periodic and are governed by several flow parameters, including the jet exit velocity profile, the jet and crossflow Reynolds numbers (Re_j and Re_∞), and the jet-to-crossflow momentum flux ratio J [48].

- In the wake region behind the jet column, upright wake vortices or "tornado-like" vortices may form due to vorticity shed from the cross-flow boundary layer and from the jet wake interaction. Fric & Roshko [42] have found these structures are more pronounced at a jet-to-crossflow velocity ratio R equals to 4. These structure can either have stationary or oscillating modes, with a similar St as wake vortices [47].

2.2.2 Main parameters

In the analysis of a JICF, three dimensionless parameters govern the interaction between the jet and the crossflow: the velocity ratio R, the density ratio S, and the momentum flux ratio J.

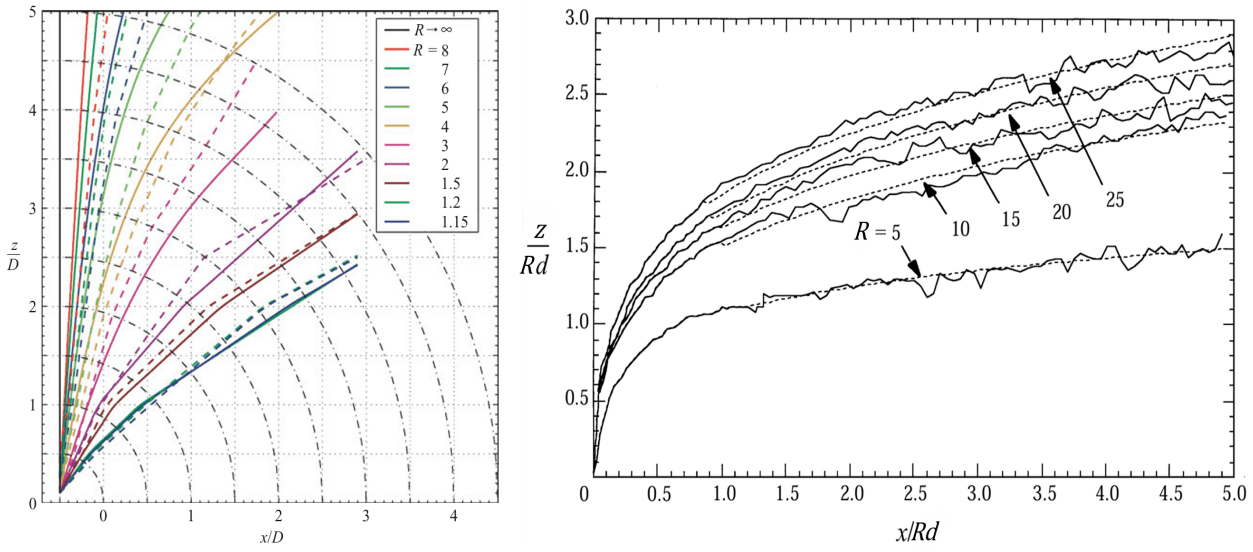
Defined in Eq. 2.4, where U_j is the jet exit velocity and U_∞ is the freestream crossflow velocity, R has historically been the principal parameter used to characterize the flow behavior, and it has been shown to primarily govern the downstream wake dynamics [49].

$$R = \frac{U_j}{U_\infty} \tag{2.4}$$

Figure 2.4 illustrates the influence of R on jet trajectories. Particularly, Fig. 2.4a focuses on the windward shear layer trajectories in the near field region at $Re_\infty = 2000$ [43]. Fig. 2.4b shows the jet centerline trajectories, normalized by Rd [50]. Both figures show that, at constant jet-to-crossflow density ratio S, increasing R enhances jet penetration into the crossflow. The velocity ratio R is known to strongly influence the jet trajectory, which is often described by the power-law relation:

$$\frac{z}{d} = A\left(\frac{x}{d}\right)^B, \tag{2.5}$$

where A and B are dimensionless coefficients that depend on the flow configuration and operating conditions. Several trajectory scalings have been proposed, including normalization by d (Eq. 2.5), Rd, and R^2d, with the objective of collapsing experimental data obtained at different values of R onto a single curve. Figure 2.4b illustrates the attempted collapse using the Rd scaling. Typical values of the trajectory coefficients for this scaling are $1.2 < A < 2.6$ and $0.28 < B < 0.34$ [51]. Despite this normalization, jet trajectories obtained for different values of R do not converge onto a universal curve. Similar conclusions were drawn when applying the R^2d scaling, further indicating that no single normalization fully captures the influence of R on jet trajectory [50]. Additional experimental studies indicate that the trajectory coefficients A and B are sensitive to the jet exit velocity profile. For the same velocity ratio R, a jet with a parabolic velocity profile penetrates more deeply into the crossflow than a jet with a mean-turbulent profile [51]. This is reflected in the trajectory coefficients: for example, New, Lim & Luo [52] report that a jet with a top-hat velocity profile typically has $A = 1.65$ and $B = 0.25$, whereas a jet with a parabolic velocity profile produces larger coefficients, $A = 1.96$ and $B = 0.31$, consistent with its deeper penetration into the crossflow. Similar conclusions were reached by Muppidi & Mahesh [53], who performed direct numerical simulations of JICF configurations. Their results suggest that an improved collapse of jet centerline trajectories can be achieved by accounting for the detailed shape of the jet exit velocity profile, rather than relying solely on the velocity ratio.



(a) (b)

Figure 2.4 Jet trajectories for various R. (a) Near field windward shear-layer trajectories normalized by d for flush jets (solid lines) and elevated jets (dashed lines) [43]. (b) Centerline trajectories normalized by Rd, with permissions [50]

Such scaling laws have been extensively reported in the literature. Early studies by Holdeman [54] demonstrated a strong correlation between increased jet penetration and improved transverse mixing in configurations dominated by crossflow. These findings were later reviewed and extended by Karagozian [55], who emphasized the relevance of penetration scaling in the context of combustor applications.

Furthermore, R governs the instability regime of the flow. Studies have demonstrated that reducing R, achieved by increasing U_∞, leads to the reinforcement of a single dominant mode of the shear layer instabilities, occurring closer to the jet exit compared to cases with higher R values [43].

In addition to the velocity ratio, the jet-to-crossflow density ratio S, defined in Eq. 2.6, also plays a crucial role in determining the jet behavior in non-equidensity flows. It is defined as :

$$S = \frac{\rho_j}{\rho_\infty}, \tag{2.6}$$

where ρ_j and ρ_∞ denote the jet and crossflow densities, respectively. The density ratio indicates the relative importance of buoyancy effects : jets lighter than the crossflow ($S < 1$) experience a predominantly upward spread, which enhances mixing with the surrounding fluid, whereas heavier jets ($S > 1$) tend to deflect downward after several downstream d, strongly influencing the far-field trajectory [56]. This behavior is commonly observed and studied in buoyant jets in the liquid phase [57], and it is also relevant in cooling applications, where temperature differences induce density variations [49]. Furthermore, both experimental and numerical studies have shown that density gradients can promote shear-layer instabilities at the fluid interface, even in the absence of strong velocity gradients [43, 58]. When $S \neq 1$ he shear layer is subject to Rayleigh-Taylor (RT) instabilities in addition to the classical Kelvin-Helmholtz (KH) instabilities, affecting the roll-up of the shear layers. In particular, study of a light jet in a heavier crossflow ($S < 1$) demonstrated that this density difference significantly increases the spatial amplification rate of shear-layer disturbances. Although the underlying physical mechanism is not fully understood, their results indicate that inertial effects associated with the density contrast dominate over viscous, buoyancy, or diffusive contributions [59].

Combining the effects of velocity and density ratios leads to the definition of the momentum flux ratio, J, which is used to characterize JICF:

$$J = SR^2 = \frac{\rho_j U_j^2}{\rho_\infty U_\infty^2}. \tag{2.7}$$

This dimensionless number quantifies the relative importance of the jet's momentum com-

pared with that of the crossflow. It has been shown to be the primary factor controlling the jet trajectory, penetration, and mixing [49, 54]. Increasing J generally results in deeper jet penetration, a straighter trajectory, and stronger entrainment of the surrounding crossflow, whereas lower J values produce jets that bend more rapidly in the direction of the crossflow and interact less with the ambient fluid [55]. Beyond these kinematic effects, J also plays a critical role in controlling shear-layer stability and vortex dynamics, which in turn strongly influence mixing processes. The resulting mixing and unmixedness do not vary monotonically with J, with optimal mixing often occurring at intermediate J values and depending strongly on density ratio, shear-layer instability regime [38] and geometrical injection factors [54]. For cooling purposes, typical values of J are below 5, enabling the jet to remain close to the surface, whereas for mixing applications, $J > 5$ [55].

The Reynolds numbers of the jet and the cross-flow are key parameters for determining the flow regime:

$$Re_{jet} = \frac{U_j d}{\nu_j}, \quad Re_\infty = \frac{U_\infty d}{\nu_\infty}, \tag{2.8}$$

where ν_j and ν_∞ are the kinematic viscosity of the fluid in the jet and the crossflow, respectively. These parameters primarily govern turbulence levels, with the transition occurring around $Re \approx 2000$ to 4000. Reynolds numbers also affect shear-layer development. Experimental observations show that the shear layer thickens as Re increases from 1000 to 2000 [60]. As discussed in Section 2.1, turbulence enhances interactions between the jet and the crossflow, thereby increasing the rate of mixing. This effect can be quantified through turbulent diffusivity, which captures the enhanced momentum and scalar transport induced by turbulent fluctuations.

2.2.3 Additional influential parameters

JICFs have been widely studied over the past decades due to their relevance in many industrial applications. In addition to the momentum flux ratio, it has been observed that geometrical configuration of injectors have a significant influence on the mixing. The following section summarizes the key studies and findings related to geometrical parameters, highlighting the existing gap in the literature regarding complex jet arrangements.

Jet-exit geometry

Although the study of Haven and Kurosaka [61] was conducted in a water tunnel, the identified mechanisms governing the formation of vortices remain relevant to gaseous jets in crossflow, as these vortex structures are inherent to the jet–crossflow interaction. However,

differences in density ratio, turbulence levels, and the absence of scalar transport limit the direct transposition of their results to reacting or variable-density flows.

Water-tunnel experiments demonstrated that the jet-exit geometry strongly governs the near-field vorticity dynamics of jets in crossflow [61]. The corresponding results are shown in Fig. 2.5. By tracking the circumferential vorticity, they identified a double-deck structure composed of a steady lower CVP, originating from the near-field region, and an intermittent upper vortex pair generated from leading-edge vorticity reoriented by crossflow entrainment. The upper layer of the double deck structure can produce either vortices with the same sense of rotation as the CVP (kidney vortices) or with opposite vorticity (anti-kidney vortices), depending on the exit geometry. Complementary experiments on elliptic jets demonstrated that aspect ratio (AR) affects only the near field: low-AR (i.e. $AR < 1$, meaning major axis of the ellipse is aligned with the crossflow) jets form two adjacent CVPs that merge downstream, while high-AR (i.e. $AR > 1$, meaning major axis of the ellipse is normal to the crossflow) jets create a single CVP and additional windward shear-layer folds that evolve into smaller Windward Vortex Pair (WVP). These WVPs can develop into kidney, anti-kidney, or newly observed interconnecting vortices. Despite these geometry-dependent near-field differences, both studies concluded that far-field structures converge toward the canonical leading-edge and lee-side vortices characteristic of circular jets in crossflow [62]. Interestingly, the time-averaged trajectory is not affected by the orifice shape [36].

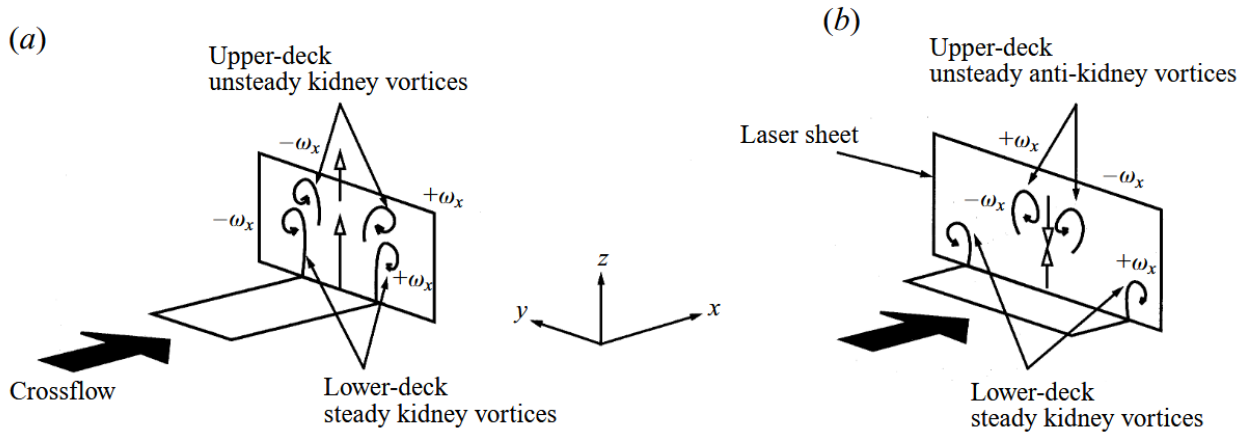


Figure 2.5 Schematic of the double-deck structure induced by a rectangular jet exit. (a) Unsteady kidney vortex pair for a low aspect ratio. (b) Hollow arrows indicate the mutually induced velocities within the upper or lower vortex pairs, with permission [61]

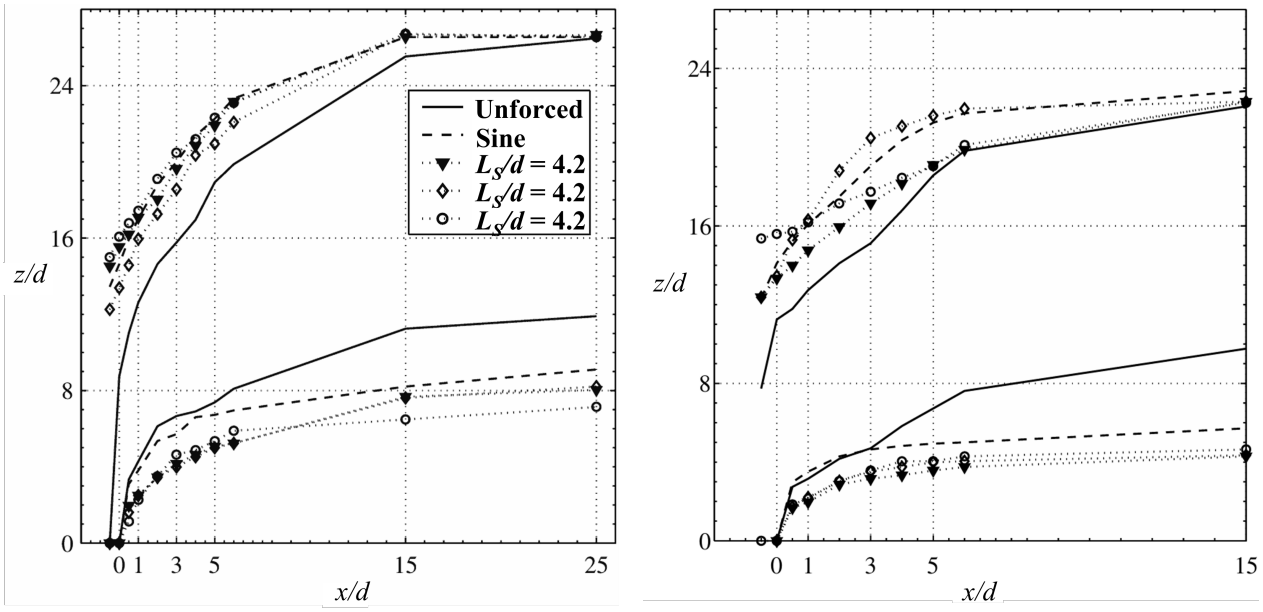
Elevated jet

For jets in crossflow, vortex dynamics are strongly influenced by both the jet and crossflow velocity profiles, shaped by the boundary layer [52]. Flush jets to the surface exhibit a horseshoe vortex system that can be stationary, oscillatory, or coalescing, with oscillation frequencies often matching the Strouhal number of wake vortices [42,47]. In contrast, elevated jets, characterized by a jet exit located at a finite distance above the surface, shed vortices at a nearly constant Strouhal number, $St_\infty \approx 0.2$, largely independent of the velocity ratio R [63], and significantly weaken near-field shear-layer instabilities [64]. This weakening delays or suppresses shear-layer roll-up and inhibits the formation of a clear, symmetric CVP, whereas flush jets under similar conditions exhibit rapid roll-up and strong CVP formation. At higher momentum flux ratios ($J \gtrsim 40$), both elevated and flush jets tend to develop convectively unstable shear layers and increasingly asymmetric vortex structures [64].

The penetration depth differs significantly between flush and elevated jets. Figure 2.6 highlights the shear layer edges on both the windward and leeward sides for each configuration. The figure also presents cases with jet flow rate modulation; however, these forced cases are not relevant to this study, which focuses solely on the unforced case (solid lines). Compared to the elevated jet, the flush jet penetrates more deeply relative to its exit height. In the flush configuration, the jet is discharged into the near-wall boundary layer, where the crossflow velocity is relatively low. This allows it to preserve its momentum and achieve greater penetration. In contrast, the elevated jet encounters higher local crossflow velocities near the exit, causing it to be deflected earlier and resulting in reduced penetration. This effect is most pronounced at relatively high momentum flux ratios ($J = 10$), whereas at lower values ($J = 3$ and $J = 1.15$) the difference in penetration between flush and elevated jets becomes negligible [38, 65].

2.3 Multiple jets arrangement

The interaction of multiple jets in crossflow has been widely investigated due to its relevance to industrial mixing devices. In such applications, multiple injection orifices are typically used to enhance mixing efficiency and control scalar distributions. Two principal configurations have been extensively studied: side-by-side (in-line) jets, where multiple jets are injected perpendicularly to the crossflow, and back-to-back configurations, where jets are aligned along the streamwise direction, for which the mutual interaction between adjacent jets strongly affects penetration, vortex dynamics, and mixing performance. A combination of these two arrangements can serve as a first approximation for gas turbine applications, where a swirling



(a) Flush jet

(b) Elevated jet ($z_{exit}/d = 3.75$)

Figure 2.6 Windward and leeward edges of a nitrogen jet into an air crossflow for $R = 10$. Unforced cases are shown with solid lines, sinusoidal forcing with dashed lines, and square-wave forcing results with corresponding effective stroke length L_S values are shown with symbols [65]

crossflow is employed to enhance flame stabilization.

2.3.1 Side-by-side configuration

In the side-by-side configuration, jet-jet interactions occur and are strongly influenced by the jet spacing s. For example, near-field interactions in water experiments for round Twin Jets In a Cross-Flow (TJICF) have been investigated for spacing ratios of $s/d = 1.5, 2$, and 3. These results were compared to the Single Jet In a Cross-Flow (SJICF) reference case, across velocity ratios of $R = 2, 4$, and 6 and constant $S = 1$, leading to $J = 4, 16$ and 36 [66]. This study shows that the jet spacing strongly governs near-field vortex dynamics and jet–jet interactions, as illustrated in Fig. 2.7.

Mutual entrainment between adjacent jets is clearly observed, as evidenced by the mixing of fluorescent dyes, and occurs for all investigated velocity ratios and jet spacings. Compared to a single JICF, leading-edge and lee-side vortices in twin jets form closer to the jet exit, which is attributed to higher initial turbulence levels in the shear layers of the twin-jet configuration. Near-field interactions are intensified for small jet spacings (s/d) and high velocity ratios. In

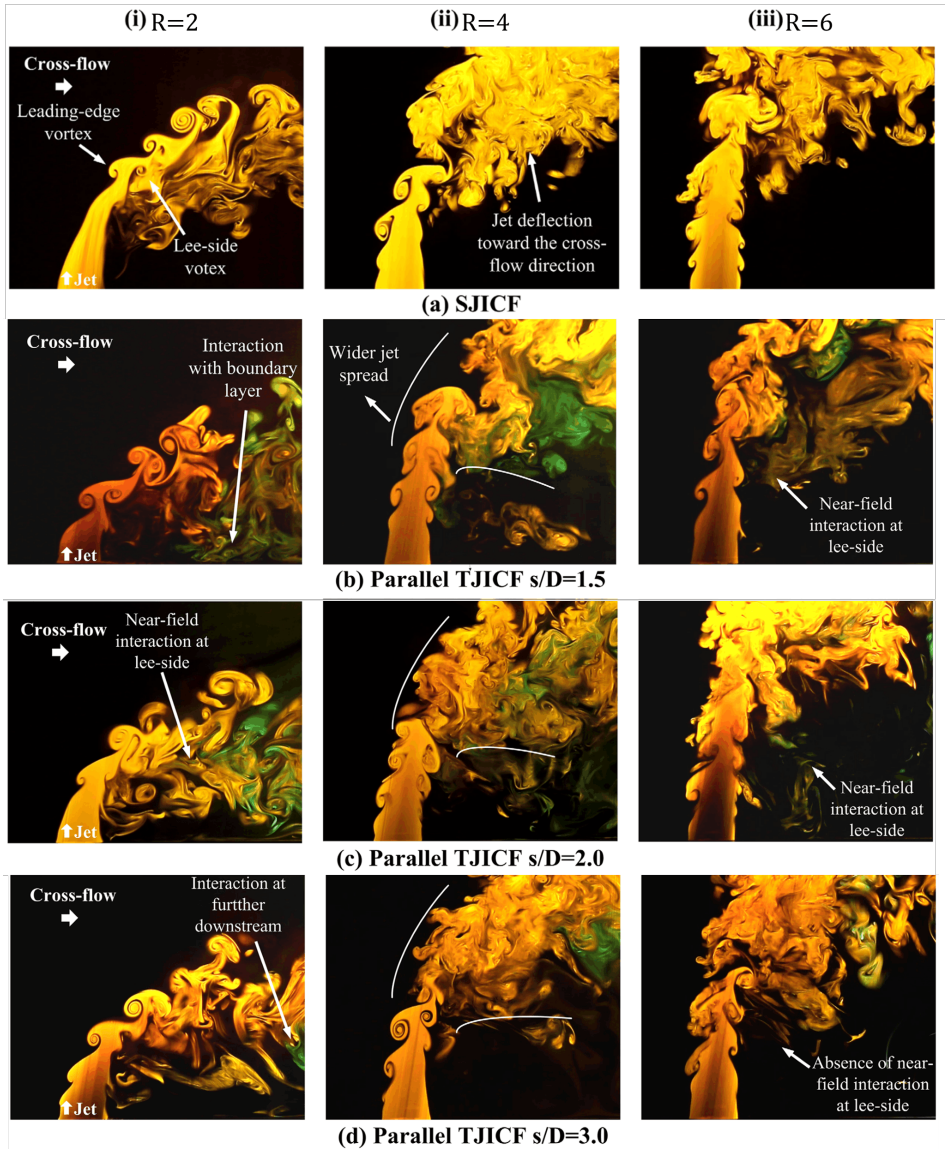


Figure 2.7 Instantaneous laser-induced fluorescence images of a SJICF (a) and side-by-side JICF (b) TJICF $s/d = 1.5$, (c) TJICF $s/d = 2.0$, and (d) TJICF $s/d = 3.0$ for $R = 2$ to 6, along the profile jet plane, adapted with permission from [66]

particular, for closely spaced jets ($s/d = 1.5$) at low velocity ratio ($R = 2$), the jet structures promote enhanced interaction with the crossflow boundary layer, suggesting a strengthened jet–boundary-layer coupling in closely spaced twin-jet configurations.

Consequently, near-field interactions between closely spaced jets strongly influence the development of vortical structures, particularly the formation and evolution of the CVP. Cross-sectional images of the same TJICF are shown in Fig. 2.8, with a schematic of the main induced vortical motion [66]. CVP formation occur at $x/d = 1$ for the single JICF case

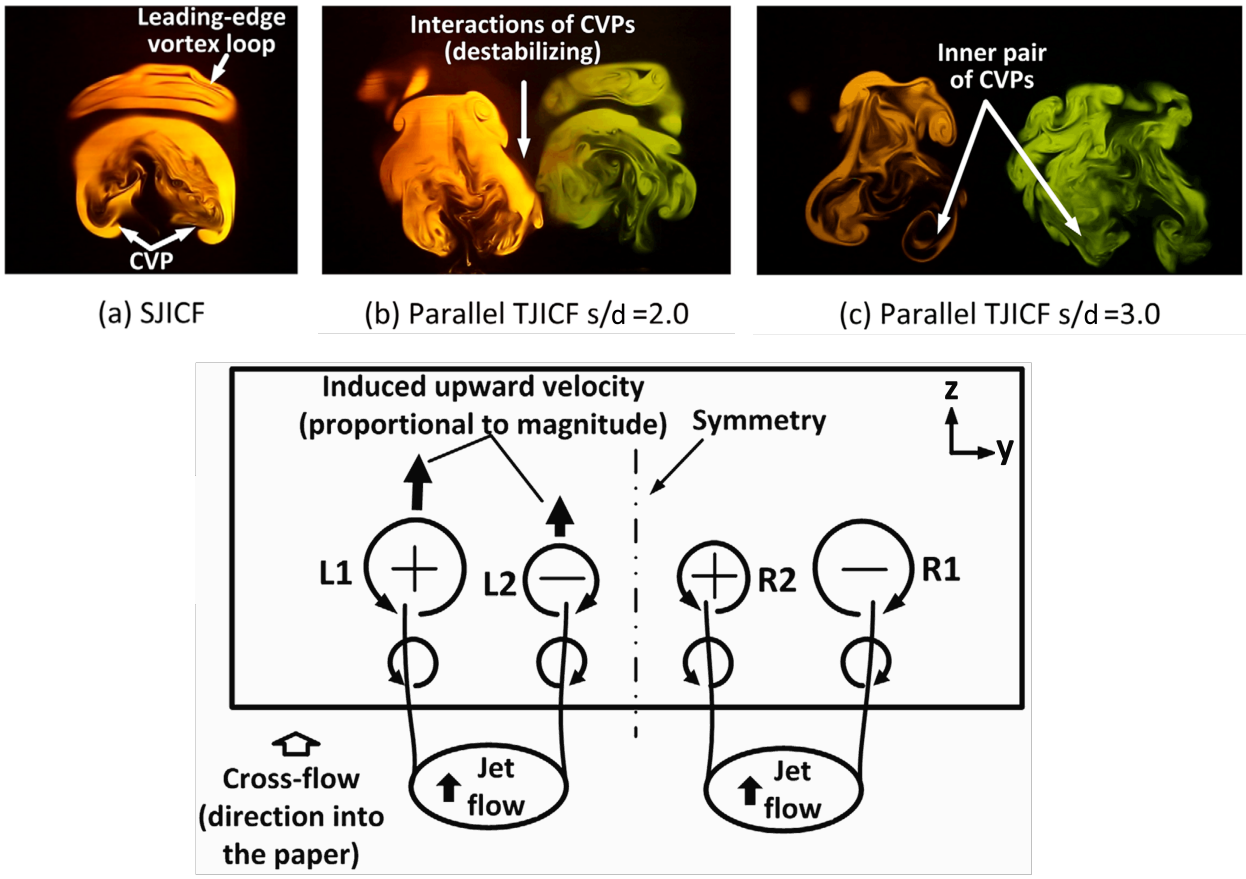


Figure 2.8 Cross-sectional images and schematic of vortex structures for side-by-side jets in crossflow at $x/d = 1$ for $R = 2$, adapted with permission from [66]

and the side-by-side JICFs at $s/d = 3.0$, while closer spacing ($s/d = 2.0$) disrupts the CVP formation.

A complementary study of twin square jets, conducted using Large Eddy Simulation (LES) [67] under jet spacing and flow conditions comparable to those investigated by [66], confirms the influence of jet spacing on vortical structures. These vortices are analyzed using cross–sectional streamlines, as illustrated in Fig. 2.9. The results demonstrate that the vortical structures are primarily governed by the jet-to-jet spacing. For sufficiently large spacings ($s/d = 8$, Fig. 2.9b), the two jets behave essentially as independent single jets, similar to the single JICF case (Fig. 2.9a). In contrast, as the spacing decreases, the inner vortex structures developing between the two jets progressively weaken (Fig. 2.9c). For the smallest spacing considered ($s/d = 2$, Fig. 2.9d), the two jets merge beyond a short downstream

distance ($x/d = 4$), and the resulting flow exhibits characteristics similar to those of a single JICF [67].

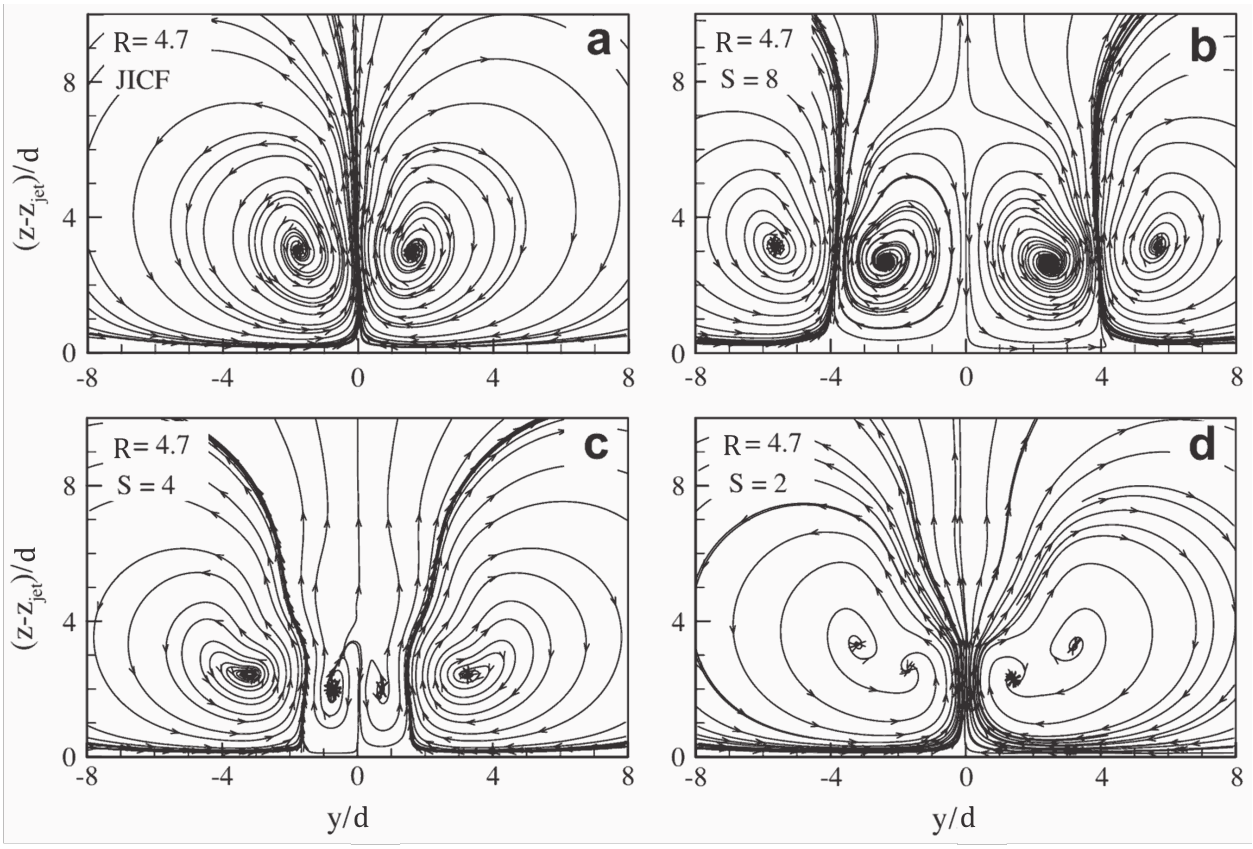
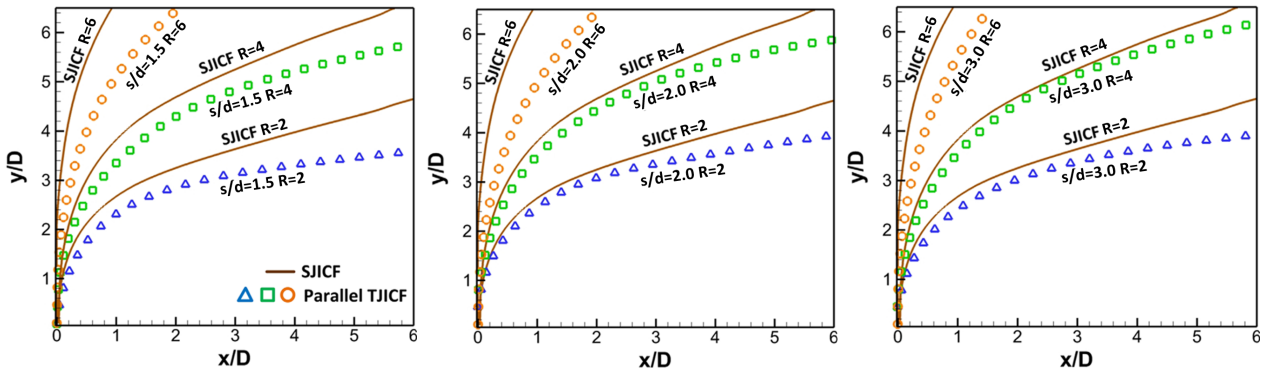


Figure 2.9 Cross-sectional average streamlines of the flow at $x/d = 4$ downstream of the jet exit for side-by-side jets, under the different R and s/d conditions, with permission [67]

The induced velocity field in the symmetry plane of the parallel TJICF exhibits distinct patterns depending on the jet spacing. For a single jet and for very closely spaced twin jets (Figs. 2.9a and d), the induced velocity is oriented upward, whereas for intermediate jet spacings (Figs. 2.9b and c) it is oriented downward. This behavior closely resembles the flow structures reported for rectangular orifices, where the orifice aspect ratio induces opposite rotational vortices in the upper deck structure of the jet (Fig. 2.5). In this sense, closely spaced side-by-side jets may be interpreted as approaching the behavior of a single orifice with a high effective aspect ratio. As a result, the downward-oriented induced velocity in the symmetry plane has been identified as a mechanism responsible for the reduced penetration of twin jets compared to single jets in crossflow [66]. A comparison of mean jet trajectories is presented in Fig. 2.10 for twin round jets under jet spacing and flow conditions similar to those of [67]. For all configurations, the single JICF exhibits a higher penetration than the corresponding parallel TJICF case. Moreover, the difference in penetration increases as the

jet spacing decreases, which is consistent with a stronger downward induced velocity acting between adjacent jet columns at smaller spacings [66].



(a) Parallel TJICF $s/d = 1.5$ (b) Parallel TJICF $s/d = 2.0$ (c) Parallel TJICF $s/d = 3.0$

Figure 2.10 Comparison of mean jet trajectories determined from PIV measurements for parallel TJICF at (a) $s/d = 1.5$, (b) $s/d = 2.0$, and (c) $s/d = 3.0$ with SJICF at similar velocity ratios as references, adapted with permission [66]

Additionally, early systematic investigations of side-by-side jets in confined ducts revealed a strong relationship between jet trajectory, jet spacing, and jet–crossflow mixing. These studies were conducted in the context of gas turbine dilution zones, where temperature fields were used as a proxy for mixing efficiency [54, 68]. Results indicate that optimal mixing is achieved when the scalar field becomes uniformly distributed across the duct's cross-section. Mathematically, this establishes a link between jet spacing and momentum flux, a relationship commonly expressed using the dimensionless parameter $C = s/H\sqrt{J}$ where H is the duct height and C a constant that depends primarily on the orifice shape and the burner design. Physically, C represents a balance between lateral spread (governed by s) and vertical penetration (driven by J), ensuring uniform mixing while preventing jet impingement on the duct walls. For a given orifice area, similar mixing distribution is obtained when C remained constant, indicating that mixing similarity between jet arrangements can be achieved over a wide range of J provided that s is adjusted accordingly. For instance, in a single-side injection configuration, the optimal mixing is achieved at $C = 2.5$. Departures from this optimum condition, either through under-penetration (low J or s) or over-penetration (high J or s), result in increased mixing non-uniformities and require longer downstream distances to reach equivalent mixing levels [54]. Better mixing uniformity can be achieved using two staggered lines of jets or by placing the second injection row on the opposite wall, with the optimum at $C = 5.0$ [54, 69], compared to a single-row arrangement. This improvement is attributed to enhanced jet interaction and more uniform momentum redistribution across

the duct cross-section, without the need for increased injection momentum.

2.3.2 Back-to-back configuration

The back-to-back jet configuration (or tandem configuration when limited to two jets), in which multiple jets are aligned sequentially in the streamwise direction, constitutes a fundamental arrangement for investigating jet-to-jet interactions in crossflow.

The flow dynamics of tandem jets have been investigated for twin circular air jets in comparison to an equivalent SJICF, at $S = 1$ [70]. The average streamwise velocity field and flow streamline for both configurations are illustrated in Fig. 2.11. The study showed that the front jet (left) exhibits penetration behavior similar to that of a SJICF, whereas the rear jet (right) penetrates further downstream. This enhanced penetration of the rear jet is accompanied by a reduction of the dispersion of the jet into the crossflow, caused by the crossflow velocity deficit and altered turbulence field generated by the leading jet.

The difference in trajectory between the front and rear jets is primarily governed by the shielding effect induced by the leading jet. This effect reduces the effective crossflow velocity experienced by downstream jets, thereby modifying their penetration and vortex structures. The presence of a strong reverse-flow region confined between the front and rear jets enhances rear-jet penetration and therefore mixing, as illustrated by the closed dark contours in Fig. 2.11. The back-flow region is larger than that observed for a single JICF and reduces the effective crossflow velocity at the rear jet interface, locally increasing the momentum flux ratio J. Consequently, this promotes penetration and lift-off of the front jet in the far field, highlighting the critical role of near-field recirculation in shaping tandem jet trajectories [70]. Additional PIV measurements on tandem TJICF [71] confirmed the shielding effect and quantified its dependence on the velocity ratio, for $R = 4$ to 15. For widely spaced jets ($s/d = 15$), the effective crossflow velocity experienced by the downstream jets is approximately 70% of U_∞, whereas for closely spaced jets ($s/d = 3$), it drops to about 30% of U_∞, highlighting the strong influence of jet spacing on the shielding effect.

Additional rear jets do not benefit from a cumulative shielding effect. Studies on multiple back-to-back JICF have shown that the trajectories of all downstream jets collapse onto a single curve that lies above the trajectory of the leading jet, indicating that the shielding effect is primarily governed by the front jet. This reduction in effective crossflow velocity was found to be independent of the number of downstream jets [71]. The non-cumulative nature of the shielding effect has been further corroborated by two-dimensional time-resolved PIV measurements [72] and semi-analytical modeling [73], which demonstrated that for velocity ratios $R \geq 2$, the leading jet provides sufficient shielding to ensure that all downstream jets

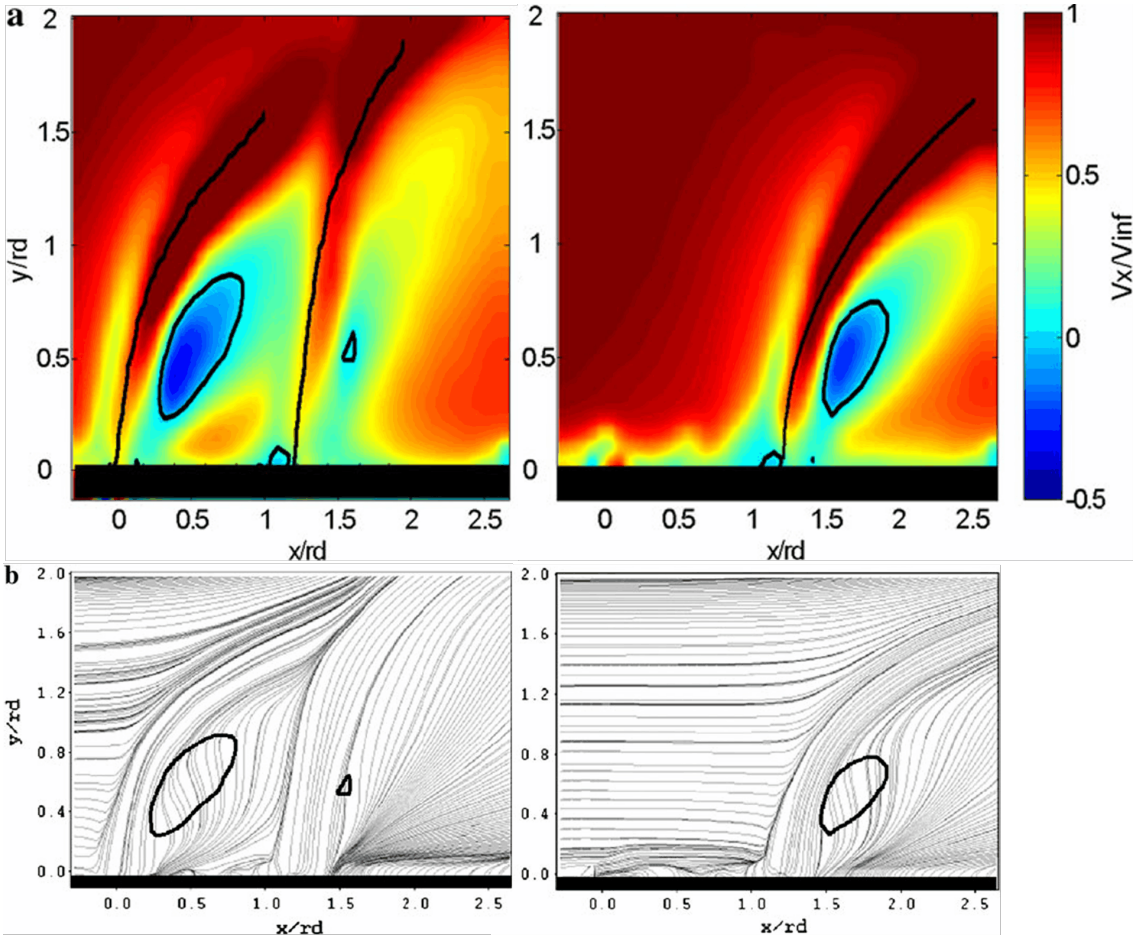
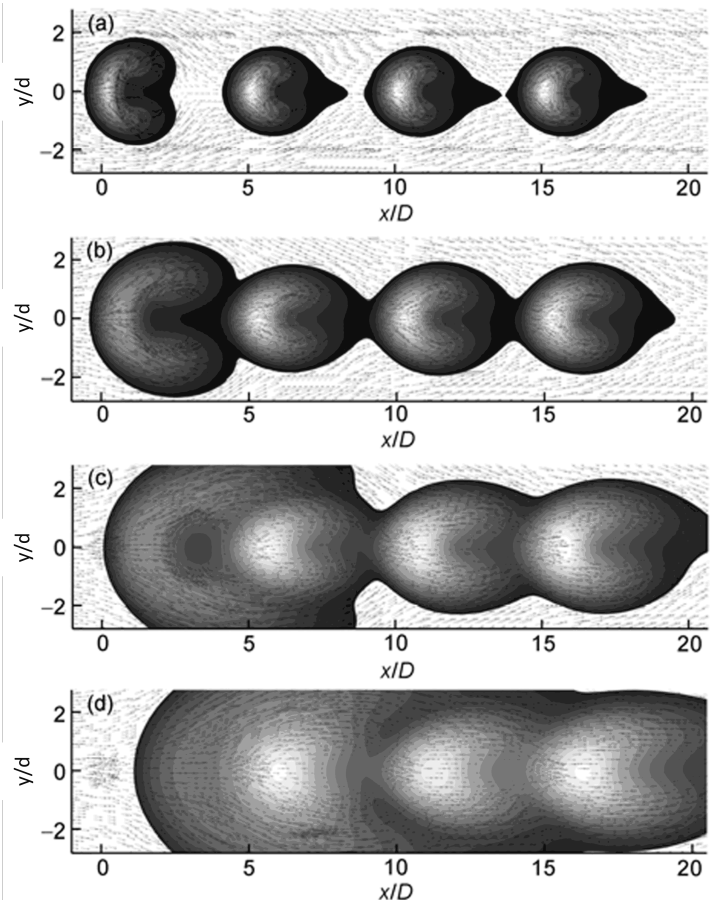


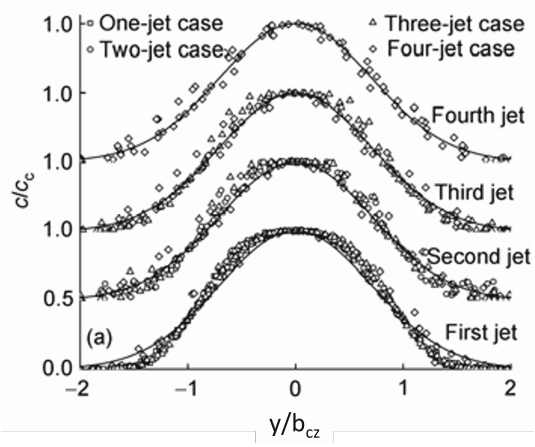
Figure 2.11 Streamwise velocity fields (top), showing jet trajectories (black lines) and regions of negative velocity (closed black contours), together with the corresponding flow streamlines (bottom), for the tandem-jet configuration (left) and the single-jet configuration (right), for $R = 3$ and $s/d = 3.55$, adapted with permission from [70]

exhibit nearly identical mean flow and unsteady characteristics.

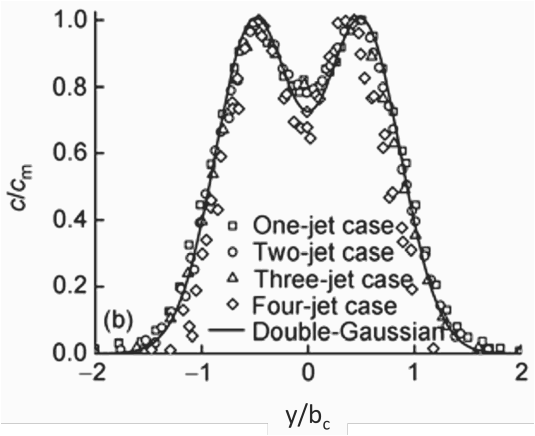
The jet concentration field of tandem jets can be divided into two distinct regimes based on the merging point, defined as the location where two adjacent jets converge [74]. The different stages of tandem jet merging are illustrated in Fig. 2.12a. In the pre-merging region, the lateral concentration distribution exhibits similar behaviors along the streamwise (x) direction for the rear jets. The lateral (spanwise, y) concentration profiles follow a Gaussian distribution, as shown in Fig. 2.12b, which is similar to a SJICF spread. This distribution is independent of the number of jets and their relative positions, indicating comparable lateral spreading characteristics for all rear jets. A slight exception occurs for the leading jet, which exhibits faster evolution and decay of concentration compared to the downstream jets, reflecting stronger interaction with the incoming crossflow. In the post-merging region,



(a) Velocity vectors and concentration contours for different top view sections : (a) $z/d = 4.5$; (b) $z/d = 6.7$; (c) $z/d = 9.0$; (d) $z/d = 11.2$.



(b) Pre-merging region ($z/d \leq 9.0$)



(c) Post-merging region ($z/d \geq 9.0$)

Figure 2.12 Concentration evolution for different tandem jet configurations: (a) top-view concentration fields of four back-to-back jets at various vertical positions; (b, c) lateral (y) concentration distributions for different numbers of back-to-back jets in the pre-merging (b) and post-merging (c) regions, adapted with permission [74]

the spanwise concentration profiles transition to a double-Gaussian distribution, as shown in Fig. 2.12c. The two maxima correspond to the centers of the CVP. Peak concentration values are 3% to 40% higher than the concentration along the jet trajectory, demonstrating that the CVP dominates scalar transport and mixing in this region. These results indicate that mixing in tandem jets is initially governed by individual jet–crossflow interactions in the pre-merging region, whereas in the post-merging region, large-scale CVP structures control lateral transport and scalar dispersion [74].

2.3.3 Swirling crossflow

In practical gas turbine combustion systems, micromix injector concepts are often implemented within a swirling crossflow to simultaneously enhance flame stabilization and promote rapid fuel–air mixing at small length scales [75]. In such configurations, the fuel is injected into a strongly stratified, rotating flow field, where both axial and tangential velocity components govern the jet development. The swirling motion significantly alters the jet trajectory and mixing mechanisms. In particular, jet penetration is reduced as the injected flow is forced to follow a helical path imposed by the crossflow rotation. This curvature enhances shear-layer development and accelerates the collapse of the jet core, leading to intensified near-field mixing [76].

The relative importance of axial and rotational effects is commonly quantified by the swirl number, Sw, defined as [75]:

$$Sw = \frac{1}{r}\frac{G_\theta}{G_x}, \tag{2.9}$$

where r is a characteristic radius of the flow, G_θ is the axial flux of angular momentum, and G_x is the axial momentum flux. Low swirl numbers ($Sw < 1$) correspond to flows dominated by axial momentum, whereas higher values indicate a growing influence of rotation. In gas turbine combustors, typical values range from $Sw \approx 0.1$ to 3.0 [77, 78].

The presence of swirl also induces a marked asymmetry in the jet cross-section. At low swirl intensity, the symmetric shape of the CVP is primarily tilted and distorted by the rotational motion. As the swirl number increases, this structure progressively transitions toward a single dominant vortex, resulting in a characteristic comma-shaped pattern [77, 78]. These observations underline the strong coupling between rotational effects, vortex dynamics, and mixing processes in jet–in–crossflow configurations subjected to swirl.

At relatively low Reynolds numbers ($Re \lesssim 10^3$) and under steady flow conditions, Sw can be approximated by the relative magnitude of the tangential and axial velocity components. A convenient dimensionless parameter to characterize this balance is the Rossby number, Ro, defined in Eq. 2.10 as the ratio of the axial velocity U to the tangential velocity $V_\theta = r\Omega$, where Ω is the angular velocity [75, 78].

$$Ro = \frac{U}{V_\theta} \tag{2.10}$$

Under these simplifying assumptions, the swirl number can be interpreted as inversely proportional to the Rossby number, i.e. $Sw \approx 1/Ro$, with low $Ro < 1$ ($Sw > 1$) for rotational dominated flows.

In micromixing applications, such as annular combustors, the penetration depth of micro-jets remains small compared to the burner diameter. As a result, the local velocity gradients induced by the stratified swirling crossflow can be reasonably neglected from the jet perspective. Under this assumption, the crossflow can be approximated as locally uniform, and a jet array angled with respect to the main flow direction provides a first-order representation of a swirling crossflow under comparable operating conditions (i.e., similar J).

Previously studied configurations such as side-by-side and back-to-back jet arrangements can be interpreted as limiting cases of the swirling crossflow. They respectively correspond to purely axial crossflow ($Ro \to \infty$, $Sw = 0$) and purely tangential crossflow ($Ro = 0$, $Sw \to \infty$). This analogy provides a useful bridge between canonical JICF configurations and more complex swirling flow environments.

2.4 Research Gaps

Despite a century of research on JICF, and several decades of studies extending these investigations to multiple-jet configurations, most fundamental work remains focused on relatively simple arrangements, such as isolated jets or twin-jet configurations. While these canonical configurations have been instrumental in establishing the fundamental physics of jet–crossflow interactions, they do not fully capture the complexity of practical injection systems encountered in propulsion and energy applications. The transition from single- or twin-jet behavior to collective multi-jet dynamics remains insufficiently characterized. These limitations are particularly pronounced for low-density micro-jets, such as hydrogen or hydrogen-enriched injections in micromix applications.

This study aims to provide a fundamental investigation of JICF geometries using configurations approaching practical conditions by :

1. analyzing jet–jet interactions, vortex dynamics, and coherent flow structures,
2. identifying scaling laws governing jet penetration for the proposed geometries,
3. quantifying the influence of injection geometry and momentum flux ratio on mixing homogeneity.

CHAPTER 3 METHODOLOGY

3.1 Experimental methods

3.1.1 Crossflow rig

To analyze and quantify JICF interactions, an experimental facility enabling optical access is used, originally designed for hypergolic combustion studies [79] and later adapted for micromix injection research [21]. The general layout is presented in Fig. 3.1.

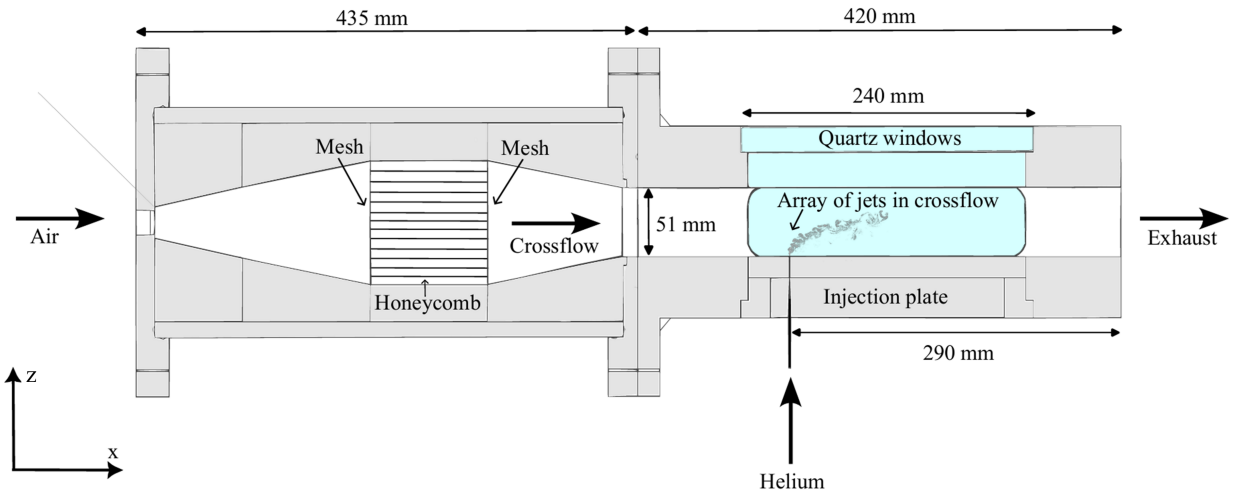


Figure 3.1 Experimental setup rig

The test rig is composed of two main sections: first a diverging-converging nozzle with a honeycomb mesh that homogenizes the crossflow and suppresses large-scale vortices, thereby ensuring a well-conditioned and uniform air flow. Second, an optically accessible square channel of 50.8×50.8 mm cross-section and 420 mm length in which the jets are injected using submillimeter medical-grade stainless steel needles (Unimed S.A., Switzerland) with an internal diameter $d = 0.7$ mm. Helium (He) is used as a surrogate for hydrogen in this non-reactive study, not only because of its diffusivity in air, which is comparable to that of hydrogen ($D_{\text{He-Air}} \approx 0.7$ cm^2/s [80], $D_{\text{H}_2\text{-Air}} \approx 0.61$ cm^2/s [26]), but also due to its similar density ratio with air. At STP, the density ratio is $S_{\text{H}_2\text{-air}} = 0.07$, while under typical gas turbine conditions ($P = 20$ bar, $T_{\text{Air}} = 750$ K and $T_{\text{H}_2} = 350$ K), it increases to $S_{\text{H}_2\text{-Air}} \approx 0.15$, which is comparable to $S_{\text{He-Air}} = 0.14$ at STP.

The mass flow rate of air in the crossflow is maintained constant at $\dot{m}_\infty = 3.72$ g/s, yielding

a theoretical velocity of $U_\infty = 1.2$ m/s, calculated at STP from the mass flow rate and the cross-sectional area of the test section. Meanwhile, the mass flow rate of a single helium jet is varied between $\dot{m}_j = 4.6 \times 10^{-4}$ g/s and 1.0×10^{-3} g/s, corresponding to jet exit velocities in the range $U_j = 7.20$ m/s to 16.2 m/s. This yields R of 6 to 13.5 and J of 5 to 25, where the lower J corresponds to applications in film cooling, and the higher J corresponds to applications in mixing [55]. Across all conditions, the jet-to-crossflow density ratio is fixed at $S = 0.14$. The Reynolds numbers achieved are $Re_\infty = 4060$ for the crossflow and $Re_j = 42$ to 96 for the jets. Key variables are summarized in Tab. 3.1.

Table 3.1 Jet flow and crossflow parameters with the corresponding non-dimensional ratios

J	S	R	Re_j	U_j (m/s)	$\dot{m}_j$ (mg/s)	U_∞ (m/s)	$\dot{m}_\infty$ (g/s)
5		6.0	42	7.20	0.46		
10		8.5	60	10.2	0.65		
15	0.14	10.4	72	12.1	0.79	1.2	3.72
20		12.0	85	14.5	0.92		
25		13.5	96	16.2	1.04		

Flow rates are controlled by two Hastings HFC-202 mass-flow controllers (±1% of full scale), calibrated with a MesaLabs ML-500 DryCal piston calibrator (±0.25% of reading), ensuring consistent and accurate operation for both air and helium. The piping and instrumentation diagram of the setup is shown in Fig. 3.2, highlighting the flow circuits, instrumentation, and main components. A picture of the experimental facility, with the laser sheet path indicated, is presented in Fig. 3.3. The translation stage supporting the final optical lenses enables spanwise (y-axis) displacement of the laser sheet via a micrometric adjustment screw, allowing repeatable acquisition of adjacent parallel planes with sub-millimeter spacing.

3.1.2 Injection array plates

The core of this study is the comparison of fuel injection patterns in terms of jet trajectories, mixing efficiency, and induced velocity fields. Particular attention is paid to the effect of the injection angle of a linear array of jets with respect to the crossflow. The array angle is varied between 30°, 45°, 60°, and 90°, the latter corresponding to a jet array perpendicular to the crossflow (side-by-side jets) while the 0° configuration represents the back-to-back jet arrangement, which is not studied here. A schematic representation of the different injection geometries is provided in Fig. 3.4a, while the actual injection plates for the different angles are shown in Fig. 3.4b.

The linear arrays consist of eight vertically aligned jets (#1 → #8). The needles used to

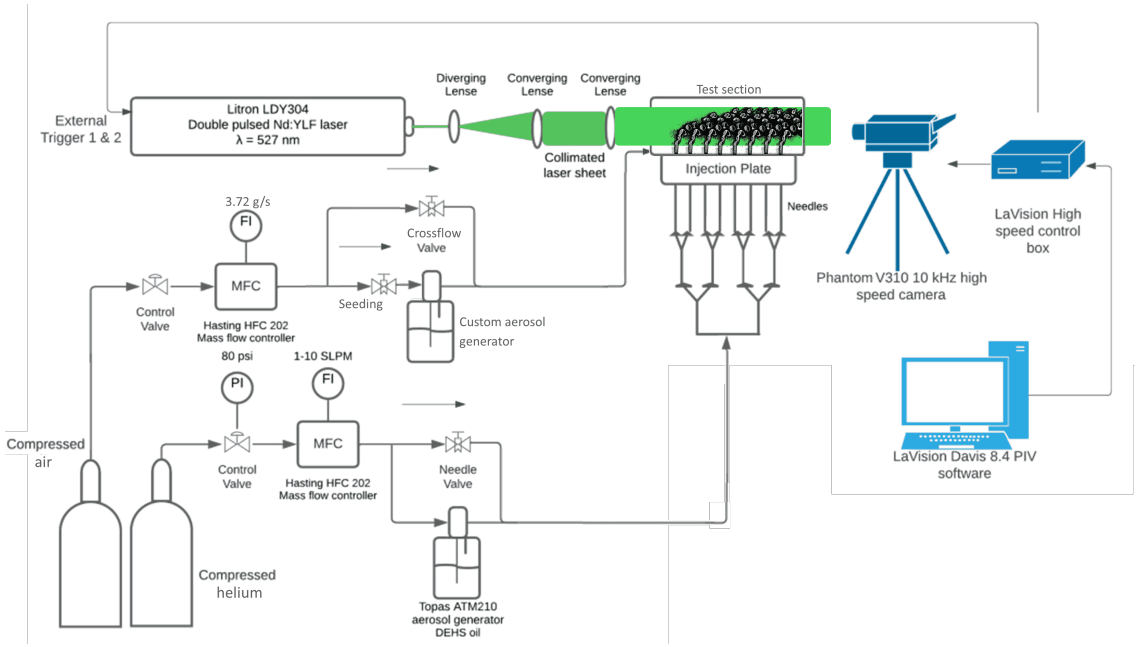


Figure 3.2 Piping and instrumentation diagram

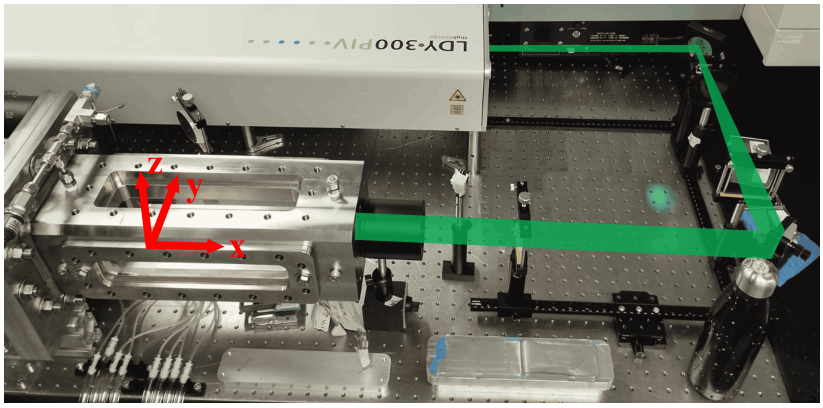
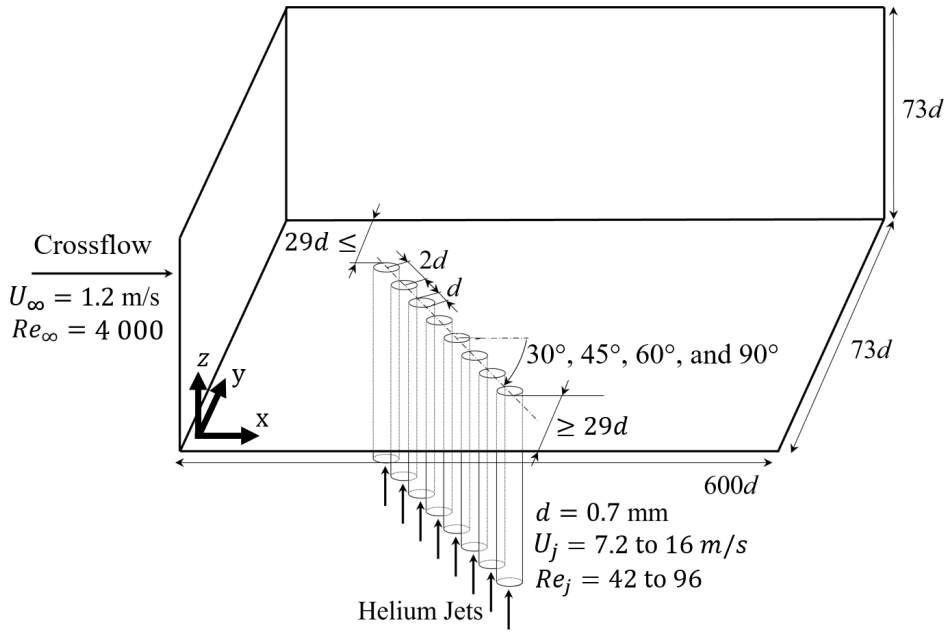
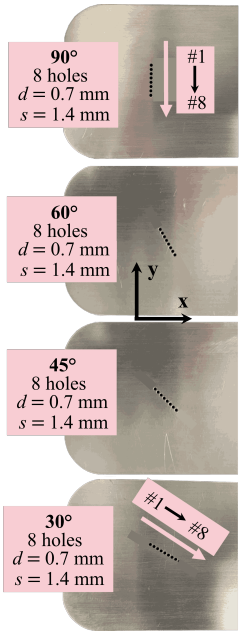


Figure 3.3 Experimental setup with laser representation within the profile view configuration

create the jets have a length-to-diameter ratio $l/d \geq 100$ ensuring that the flow inside each needle is fully developed before exiting into the crossflow. The jets are uniformly spaced ($s/d = 2$), a configuration that promotes inter-jet interactions, while preserving the integrity of individual jet structures [66]. The jet-to-jet spacing in the spanwise (y-axis) direction, s_y/d, and the corresponding streamwise (x-axis) spacing, s_x/d, are determined by the injection angle, which ranges from 30° to 90°. These relationships are detailed in Tab. 3.2. Based on subsection 2.3.3, the swirl number is also given as a function of the array angle. It is approximated as $Sw \approx 1/Ro = v/u$, where u and v denote the velocity components in the horizontal (xy) plane.



(a) Schematic linear array of jets



(b) Top-view of the linear arrays

Figure 3.4 Injection configurations of the linear jet arrays: (a) Schematic representation and (b) Top views of the experimental arrays

Table 3.2 Jet spacings s_x/d and s_y/d and swirl number Sw evolution across the array angles

Angle (°)	90	60	45	30
s_x/d	0.0	1.0	1.4	1.7
s_y/d	2.0	1.7	1.4	1.0
Sw	0.0	0.6	1.0	1.7

3.2 Particle Image Velocimetry (PIV)

Optical access to the test section is provided by three 45 mm-thick quartz windows, allowing non-intrusive laser-based diagnostics. In this study, planar mixing and velocity fields are obtained using illuminated particles and PIV. Illumination is provided by a dual-head Nd:YLF laser (Litron LDY304, $\lambda = 527$ nm), synchronized with a Phantom v310 high-speed camera equipped with a 150 mm $f/2.8$ macro lens (Sigma). The detector resolution is 1280×800 pixels, corresponding to a spatial resolution of 21.5 ± 0.1 pixels/mm over the field of view, as determined from a calibration target (R2L2S3P3, Thorlabs). Acquisition is performed at 1 kHz for most datasets, leading to a , up to 4 kHz for spectral analysis, offering both high temporal and spatial resolution of the jet–crossflow interaction. The laser beam is trans-

formed into a thin sheet, characterized in Sec. 3.2.2, by a set of cylindrical optics, enabling two-dimensional plane visualization of the flow.

The velocity fields are measured using PIV, a technique based on estimating the mean particle displacement within interrogation windows between two consecutive images. The flow is seeded with tracer droplets that must accurately follow the fluid motion. These particles are illuminated by a thin laser sheet. The recorded particle images are subdivided into interrogation windows, which must be sufficiently small to assume a nearly uniform displacement within each window, yet large enough to contain an adequate number of particles for reliable statistical analysis. The local displacement is determined through cross-correlation between corresponding interrogation windows in successive images. The resulting correlation map exhibits a peak whose position provides both the magnitude and direction of the local velocity vector. The accuracy of this method strongly depends on the particle seeding density, as sufficient particle images are required to obtain a well-defined correlation peak.

These concepts are detailed in the following subsections.

3.2.1 Oil droplets seeding

Velocity measurements in PIV rely on the presence of tracer particles dispersed in the flow, whose displacement between successive frames can be tracked to infer the local velocity field. In this study, Di-Ethyl-Hexyl-Sebacate (DEHS) oil droplets are employed, generated using a Topas ATM 210 atomizer for helium and a custom atomizer for air, as shown in Fig. 3.2, producing droplets of mean diameter $d_p \leq 1$ μm and density $\rho_p = 912$ kg m^{-3} [81, 82].

As the fluid motion is not observed directly but rather through the displacement of seeded droplets, it is crucial that the tracers faithfully follow the flow dynamics. For example, Fig. 3.5 illustrates the deviation of a poorly responding tracer particle from the fluid path line, highlighting the inability of such particles to faithfully follow the flow. This behavior is commonly assessed through the Stokes number Stk, defined as :

$$Stk = \frac{\tau_p}{\tau_f}, \tag{3.1}$$

which compares the particle response time τ_p (Eq. 3.7) to the characteristic flow time scale τ_f (Eq. 3.8). A Stokes number $Stk \ll 1$ indicates that particles closely follow the fluid motion. In practice, a threshold of $Stk < 0.1$ is commonly adopted to ensure accurate flow tracing, with associated velocity errors typically below 1% [84].

The particle response time, τ_p, can be derived under the assumptions of Stokes' drag law, i.e.,

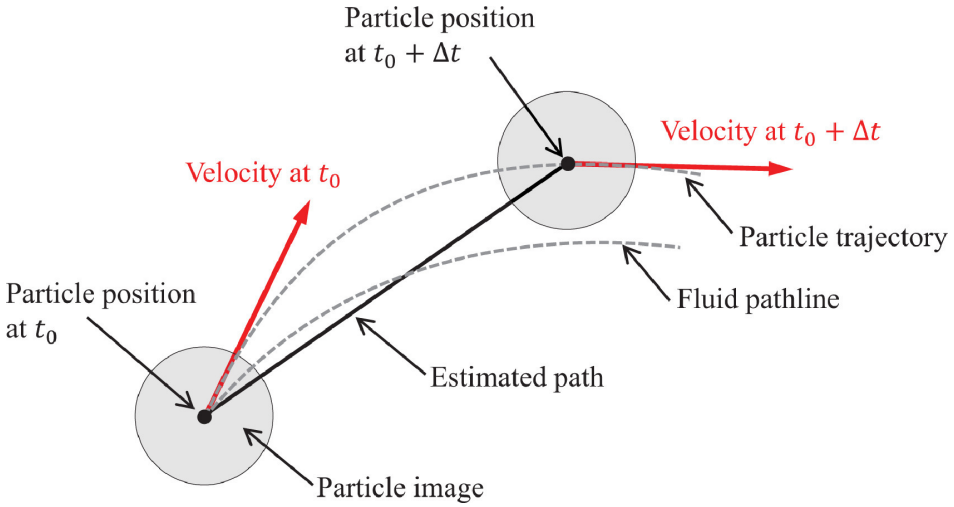


Figure 3.5 Schematic comparison of the fluid motion, the actual particle response, and the particle trajectory estimated by the measurement technique; under Creative Commons CC-BY [83]

the particle evolves in a continuum flow and inertial effects at the particle scale are negligible. The validity of the continuum assumption is quantified by the Knudsen number, Kn, defined in Eq. 3.2, as the ratio between the mean free path of the gas molecules, $\mathcal{L}$ (Eq. 3.3), and the characteristic length scale of the particle, here its diameter d_p:

$$Kn = \frac{\mathcal{L}}{d_p}. \tag{3.2}$$

The Knudsen number characterizes the flow regime: for $Kn < 0.01$, the continuum assumption holds and the Navier–Stokes equations are applicable, whereas slip-flow corrections become necessary in the range $0.01 < Kn < 0.1$. For $0.1 < Kn < 10$, the flow is partially rarefied and requires modified models than neither continuum assumptions nor free-molecular approximations; for $Kn > 10$, gas molecule interactions dominate and Stokes' law no longer applies [85, 86].

In the kinetic theory of gases, the mean free path of a particle, such as an air molecule, is defined as the average distance it travels between successive collisions with other molecules. For a simple hard-sphere gas in thermodynamic equilibrium, this is given by [87]:

$$\mathcal{L} = \frac{1}{\sqrt{2}\,\pi\, n\, d_\infty^2}, \tag{3.3}$$

where $d_\infty \approx 0.35$ nm is the molecular diameter of air [87], and n is the molecular number

density, expressed as

$$n = \frac{\rho_\infty \mathcal{N}_\mathrm{A}}{M_\infty}, \tag{3.4}$$

with $\mathcal{N}_\mathrm{A} = 6.022 \times 10^{23}\ \mathrm{mol}^{-1}$ the Avogadro number, $\rho_\infty = 1.2\,\mathrm{kg\,m}^{-3}$ the air density at STP, and $M_\infty = 28.96\ \mathrm{g\,mol}^{-1}$ the molar mass of air. This yields a mean free path of approximately $\mathcal{L} \approx 70$ nm. From this value, the Knudsen number is $Kn = 0.07$ indicating the flow is in the slip regime. Regarding corrections to Stk, the slip of gas molecules at the particle surface can no longer be neglected. To account for this effect, the dynamic viscosity of the flow, μ_∞, is replaced by μ_∞ / C_c, where C_c is the Cunningham slip factor (Eq. 3.5) [88, 89].

$$C_c = 1 + 2\,Kn\left(C_1 + C_2\, e^{-C_3/Kn}\right), \tag{3.5}$$

where $C_1 = 1.257$, $C_2 = 0.400$, and $C_3 = 0.55$ are empirical coefficients for air at STP [89]. For example, with $Kn = 0.07$, one finds $C_c = 1.18$.This modification reduces the drag force on the particle, resulting in an increased particle response time (Eq. 3.7).

To ensure that Stokes' drag regime is valid, the second criterion is that inertial forces at the particle scale are negligible. This is evaluated through the particle Reynolds number Re_p, defined in Eq. 3.6, and must satisfy $Re_p < 1$ [90].

$$Re_p = \frac{\rho_f U_{rel} d_p}{\mu_f}, \tag{3.6}$$

where ρ_f denotes the fluid density ($\rho_\infty = 1.2\,\mathrm{kg\,m}^{-3}$ for the air crossflow and $\rho_j = 0.16\,\mathrm{kg\,m}^{-3}$ for the jets), U_{rel} is the local relative velocity between the fluid and the particle, and $d_p = 1\mu$m the DEHS droplet diameter. For the present estimation, a conservative assumption is made by taking $U_{rel} = U_j$, which represents the highest velocity in the flow. Finally, μ_f represents the dynamic viscosity of the fluid ($\mu_\infty = 1.85 \times 10^{-5}\,\mathrm{Pa\,s}$ for air and $\mu_j = 1.96 \times 10^{-5}\,\mathrm{Pa\,s}$ for He in the jets).

For the highest turbulence case ($J = 25$), the jet exit velocity reaches $U_j = 16.2\,\mathrm{m\,s}^{-1}$, yielding a particle Reynolds number $Re_p = 1$ in air and $Re_p = 0.13$ in helium. However, these values are likely overestimated due to the conservative assumption of a large relative velocity ($U_{rel} = U_j$). Therefore, the Stokes's drag law can be applied to the oil droplets and their response time is :

$$\tau_p = \frac{\rho_p d_p^2}{18\mu_f} C_c = 3.1\ \mu\mathrm{s}. \tag{3.7}$$

Additionally, the characteristic flow time scale can be defined from the convective dynamics of the crossflow. Assuming turbulent eddies of characteristic length scale comparable to the

jet diameter d, and convected at the crossflow velocity U_∞, the flow time scale is given by

$$\tau_f = \frac{d}{U_\infty} = 580\,\mu\text{s}. \tag{3.8}$$

The corresponding Stokes number for DEHS is therefore $Stk = 5 \times 10^{-3} \ll 1$. Hence, DEHS droplets provide a reliable means of capturing momentum transport and resolving the velocity fields within the present JICF experiments [84, 91, 92].

Finally, to evaluate the risk of particle breakup, the ratio of aerodynamic shear forces to surface tension forces can be expressed by the Weber number We. Particle fragmentation typically occurs for high Weber number [93]. The Weber number is defined as :

$$We = \frac{\rho_f U_{\text{rel}}^2 d_p}{\sigma_{\text{DEHS}}}, \tag{3.9}$$

where $\rho_f = \rho_\infty$ (conservative case as $\rho_\infty > \rho_j$), $U_{\text{rel}} = U_j$ at $J = 25$ (conservative case), and σ_{DEHS} the surface tension of DEHS ($\sigma_{\text{DEHS}} = 0.032$ N/m [94]). Under the present experimental conditions, the estimated Weber number is $We \approx 10^{-2} \ll 1$, indicating that droplet breakup is highly unlikely.

3.2.2 Laser sheet: generation, waist and intensity profile

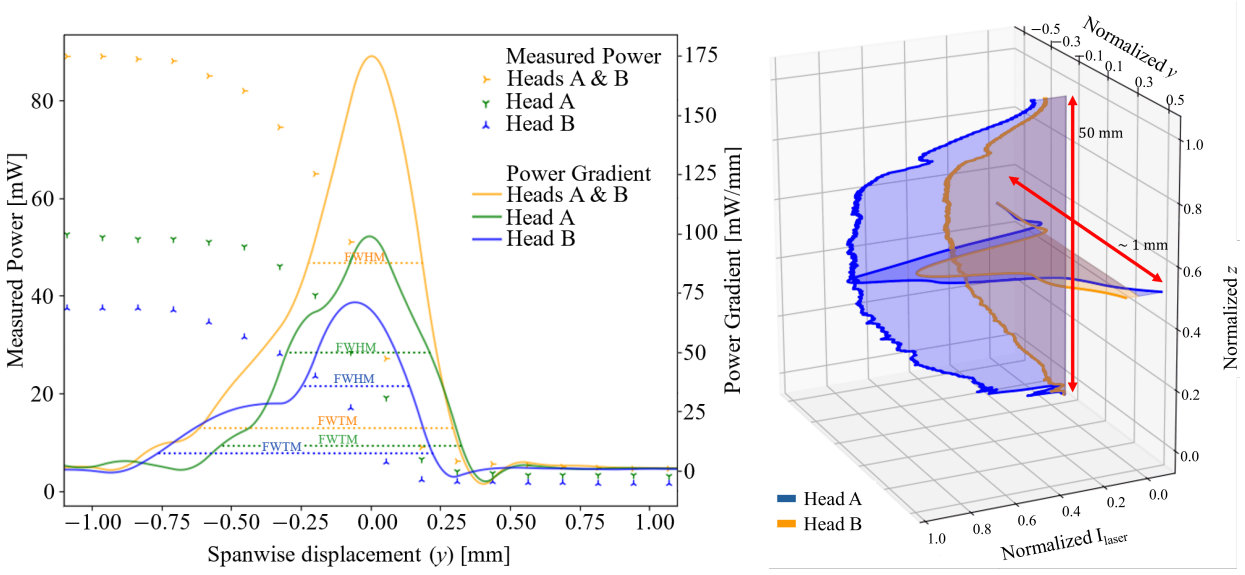
Oil droplets seeded into the jets and the crossflow are illuminated by a laser sheet to provide a planar view of the flow. The laser beam is expanded in the z-direction using a diverging–converging lens pair with focal lengths of $f_{\text{div}} = -30$ mm and $f_{\text{conv}} = 300$ mm, spanning the entire height of the channel. However, the laser sheet is blocked for approximately $3d$ at the bottom to prevent reflections from the jet injection surface.

It is well established that out-of-plane displacement constitutes one of the primary factors limiting accuracy in PIV measurements [95]. To minimize misinterpretation from of out-of-plane motion, the laser sheet must be as thin as possible. This ensures that the displacement and, therefore, the velocity of particles in the direction normal to the laser plane is not captured in the measurement. This is achieved by focusing the laser in the y direction with a lens of $f = 500$ mm, producing a thin laser waist coincident with the jet exit.

In practice, the waist cannot be made infinitely small due to diffraction, beam quality factor M^2, and imperfections in the optical components. The actual thickness of the laser sheet is determined experimentally using the knife-edge method, in which a sharp object progressively blocks the beam and the resulting energy is recorded as a function of the edge position. The measured energy for various knife-edge clippings are shown in Fig. 3.6a, fitted into a smooth

intensity curve, that is then differentiated to extract the energy distribution (solid lines), from which the effective laser waist can be quantified. Several conventions exist to define the beam waist: the Full Width at Half of the Maximum (FWHM), the Full Width at 10% of the Maximum (FWTM) [96], or the 1/e and $1/e^2$ criteria commonly used in laser safety applications [97]. In this study, the FWTM definition is adopted, as it provides the largest beam waist and therefore ensures that the full spatial extent of the laser beam, including its low-intensity tails, is taken into account. PIV measurements require a pair of images acquired from two camera exposures synchronized with the laser double pulse. Therefore, Fig. 3.6a presents the intensity distributions of both laser heads, centered on the maximum intensity of Head A. The effective laser sheet (orange curve) results from the superposition of both beams, leading to a combined waist thickness of $w_{\text{laser}} = 0.9$ mm at FWTM.

In addition, the laser profile in the xz-plane is characterized in Fig. 3.6b. The profile results from an average of the intensity of the seeded crossflow recorded by the camera and represents the laser sheet irrandiance profile as observed through the imaging system. The profile comes from the bottom to the local intensity irregularities are visible and are attributed to the camera's image quality (around $z \approx 0.8$). The observed intensity peaks in regions where the laser is typically absent, such as at $z = 0$, are attributed to laser reflections within the experimental facility. To mitigate this effect, the laser sheet is lifted, as discussed above, to not intersect the bottom of the channel.



(a) Width of the laser sheet calculated based on power measurements

(b) Normalized laser beam intensities in the y and z directions

Figure 3.6 Characterization of the laser sheet geometry and intensity distribution

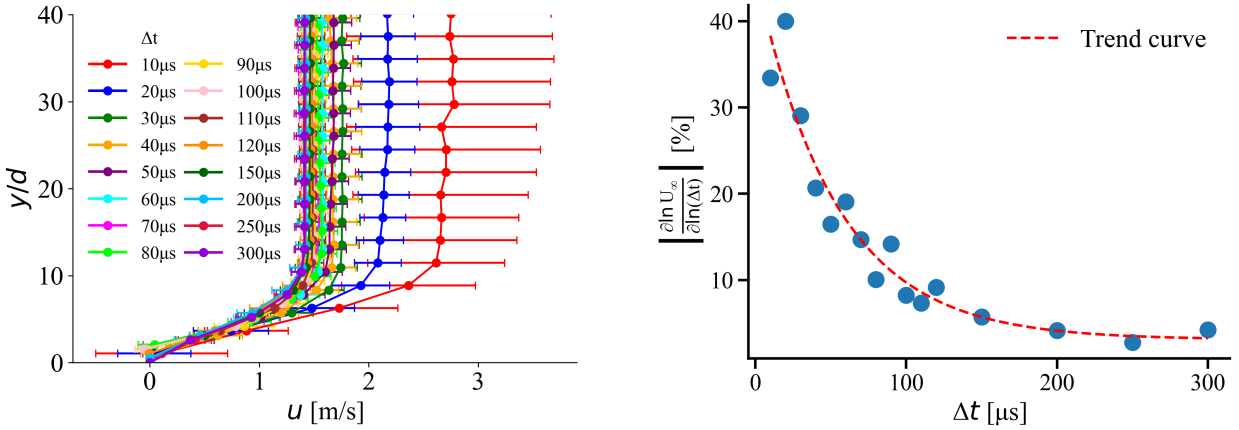
Two main phenomena are observed in the laser sheet profiles: a difference in peak intensity and a spatial offset between the two heads. First, the peak intensity of head B is approximately 25% lower than that of head A. From a PIV perspective, a uniform multiplicative change in intensity between two frames does not shift the correlation peak when particle images are well isolated; in this case, the displacement estimate remains theoretically unaffected. However, for non-Gaussian intensity distributions or when particle images overlap, relative intensity variations distort the correlation map and may shift its maximum, typically introducing a systematic bias on the order of 0.1 pixel in the Root Mean Square (RMS) displacement error [95].

Second, a spatial misalignment exists between the two laser heads. The measured profiles are not perfectly aligned: their peaks are offset by approximately 0.2 mm ($\approx 20\%$ of w_{laser}). Such misalignment promotes out-of-plane particle pair loss, thereby reducing the number of valid particle pairs contributing to the correlation and increasing the likelihood of spurious vectors [98, 99]. Accordingly, the intersection of the two normalized laser sheet areas is directly related to the expected proportion of spurious vectors. In the present study, the intersection represents about 81% of the larger area (head A) for the laser waist (along the y axis) and 84% for the vertical intensity profile (along the z axis). Under these conditions, the proportion of spurious vectors is expected to remain around 1% of the total number of vectors [98].

3.2.3 Inter-frame delay time

Another key parameter in PIV measurements is the inter-frame delay time, Δt, which defines the temporal separation between the two images of a double-frame pair. This delay controls the particle displacement between frames and directly affects the accuracy of the reconstructed velocity field. If Δt is too short, particle displacements are minimal, leading to poor correlation and higher measurement uncertainty. Conversely, if Δt is too large, fast small-scale structures may not be properly resolved, leading to a loss of high-frequency flow information. In addition, excessive delay time can result in particle pair loss and the generation of spurious vectors due to out-of-plane motion.

To select an appropriate inter-frame delay, multiple snapshots of the crossflow are recorded at different Δt values. Velocity fields are computed from each dataset, and temporal mean crossflow velocity profiles are extracted, as shown in Fig. 3.7a. Standard deviations illustrate temporal fluctuations. Significant deviations are observed for $\Delta t \leq 50$ μs, indicating insufficient particle displacement for accurate correlation. As Δt increases, profiles converge, reaching a bulk crossflow velocity of 1.4 m/s. The discrepancy with the theoretical value



(a) Measurements of the crossflow velocity profiles

(b) Crossflow velocity sensitivity relative to Δt variations across Δt

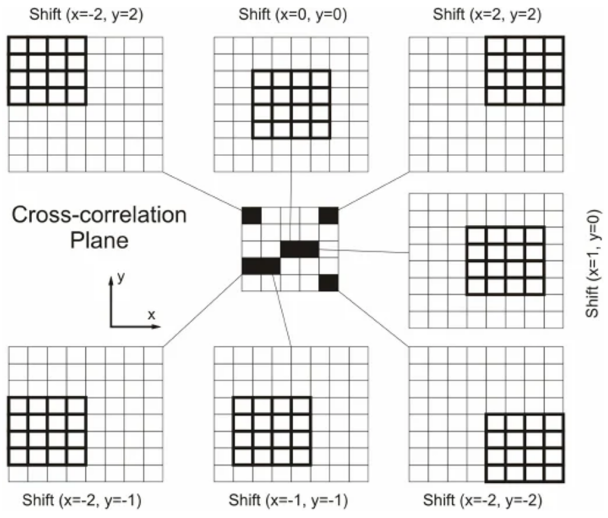
Figure 3.7 (a) Crossflow velocity profiles and (b) their sensitivity analysis, for different inter-frame delay time Δt measured at the jet exit location for an air mass flow rate of 3.72 g/s in a 52×52 mm^2 square channel

$U_\infty = 1.2$ m/s arises from velocity boundary layers causing the velocity to vary from zero at the wall (no-slip condition) to the free-stream value. Integrating the velocity profile for $\Delta t = 300$ μs yields $U_{\infty,300\mu s} = 1.15$ m/s, closer to the theoretical value $U_\infty = 1.2$ m/s. Yet, this inter-frame delay time is too long and must also be suitable for capturing the jets. The jets inject additional momentum into the crossflow, enhancing shear layers and generating small-scale vortices. Under these conditions, Δt must be short enough to resolve fast structures while ensuring sufficient particle displacement. To select the minimal Δt with low relative impact on the velocity determination: a sensitivity analysis of the crossflow velocity with respect to Δt is provided in Fig. 3.7b. The sensitivity is quantified using the logarithmic derivative and represents the relative variation of velocity for a relative variation of the interframe delay. For example, $\Delta t = 80$ μs corresponds to a sensitivity of 12%, meaning a 100% variation in Δt changes the normalized velocity by 12%. The data can be grouped into three regimes: low $\Delta t < 80$ μs with high sensitivity $> 15\%$, intermediate $80 \leq \Delta t \leq 120$ μs with sensitivity near 10%, and high $\Delta t > 120$ μs with sensitivity around 5%. Based on this analysis, $\Delta t = 80$ μs appears as an optimal choice.

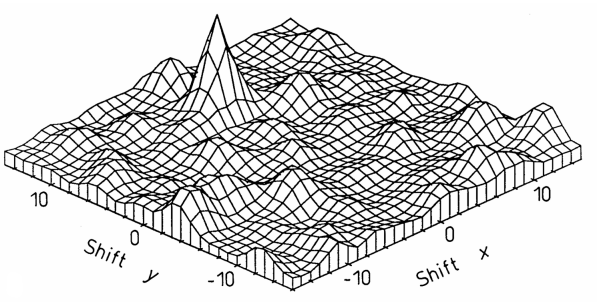
3.2.4 Interrogation zone configuration and outlier detection methods

PIV measurements also rely on the size and configuration of the interrogation zones, i.e., the sub-regions of the image in which the cross-correlation is computed. The PIV algo-

rithm discretizes the illuminated plane into interrogation windows and determines the local particle displacement by comparing the intensity patterns between corresponding regions of two consecutive frames. This process, schematically illustrated in Fig. 3.8a, relies on cross-correlation: each interrogation window of the first frame is compared to neighboring regions in the second frame, and the displacement vector is assigned according to the location of the highest correlation peak (Fig. 3.8b) [100].



(a) Construction of the cross-correlation plane : a 4×4-pixel interrogation window is correlated with an 8×8-pixel search area, yielding a 5×5-pixel correlation plane; under CC BY 4.0 [101]



(b) Example of a cross-correlation map exhibiting a single dominant peak, from which the magnitude and direction of the particle displacement vector are determined, with permission [100]

Figure 3.8 Illustration of the cross-correlation process used in PIV

The choice of the interrogation window size is critical. If the window is too small, particles may leave the region between two frames, leading to poor correlation or noise amplification. Conversely, a very large interrogation window reduces the spatial resolution and fails to resolve fine turbulent structures. A common guideline is that the average particle displacement should be approximately 1/4 of the window size [83]. In the present experiments, with an inter-frame delay of $\Delta t = 80$ μs, the average particle displacement is expected to be approximately 4–5 pixels, which is consistent with the use of interrogation windows of 16×16 pixels.

To improve the spatial density of velocity vectors across the field of view, adjacent interrogation windows are overlapped. In this study, a 50% overlap is used, which effectively doubles the number of vectors obtained in each direction. It is important to note, however, that increasing the overlap does not improve the true spatial resolution of the measurement.

Instead, it provides a denser grid of velocity vectors, although neighboring vectors are not fully independent as they include partially redundant information [102].

In addition, a multipass algorithm is applied. The computation begins with large interrogation windows of 64×64 pixels to obtain robust initial displacement estimates with a high signal-to-noise ratio, reducing the displacement error [98, 99]. This initial velocity field is then used to shift and deform the window, thereby reducing the relative displacement within each interrogation window. The process is iteratively repeated with smaller windows (down to 16×16 pixels), progressively refining the velocity field and improving the resolution in regions with strong velocity gradients such as shear layers and jet boundaries. In the end, the final velocity field corresponds to the smallest interrogation window, but its quality is enhanced by the information propagated from the larger-window passes.

Finally, spurious vectors are removed using a two-step validation procedure. First, a correlation peak ratio criterion is applied to validate the PIV vectors. This criterion relies on the relative difference between the two highest correlation peaks, defined by the peak ratio $Q = \text{peak}_1/\text{peak}_2$. Vectors with a primary-to-secondary peak ratio $Q < 2$ are systematically rejected to eliminate spurious matches. Second, a local statistical filter is applied. A velocity vector $\mathbf{u}$ is discarded if its deviation from the neighborhood exceeds three standard deviations, following the criterion $\|\mathbf{u} - \overline{\mathbf{u}}_{\mathcal{N}}\| > 3\sigma_{\mathcal{N}}$, where $\overline{\mathbf{u}}_{\mathcal{N}}$ and $\sigma_{\mathcal{N}}$ denote the mean and standard deviation computed over the neighboring vectors $\mathcal{N}$. Rejected vectors are re-evaluated iteratively over five passes and reinserted when the previous statistical criterion is satisfied.

3.2.5 Particle density

A critical aspect in PIV measurements is the seeding density, i.e., the number of Particles Per Pixel (ppp), N_{ppp}, which directly affects the reliability and robustness of the correlation process. On one hand, excessively high densities cause individual particles to overlap. When coherent illumination is used under such conditions, interference produces a random granular intensity pattern known as speckle, which significantly deteriorates the correlation process. On the other hand, too few particles lead to insufficient correlation signals, reducing the reliability of velocity measurements [102]. Although no strict maximum particle density has been established in the literature, typical reported values indicate that optimal PIV measurements require particle densities to minimize computational errors, $N_{\text{ppp}} \sim 10^{-2}$ [103]. In the present study, the flow is homogeneously seeded with DEHS oil droplets throughout the test section. The resulting average particle density in the captured images is $N_{\text{ppp}} \approx 0.1$, higher than the typical range for PIV.

A lower bound on particle density can be estimated based on the number of particles per interrogation window (16×16 pixels), $N_I = 16^2 N_{\text{ppp}}$, the in-plane correlation factor F_I (the fraction of particles staying within the interrogation window after a displacement within the laser plane), and the out-of-plane correlation factor F_O (the fraction of particles remaining within the laser sheet thickness after a spanwise displacement). To ensure a reliable identification of the correlation peak, these parameters should satisfy $N_I F_I F_O > 7$ [104].

For a mean streamwise particle displacement of 4 pixels within a 16×16 pixel interrogation window (corresponding to $\Delta x = 0.19$ mm in the bulk flow), the fraction of particles remaining in the interrogation window can be approximated as $F_I \approx 1 - 4/16 = 0.75$, assuming displacement occurs predominantly in a single direction within the window. Assuming that the spanwise displacement is similar to the streamwise displacement ($\Delta x = \Delta y$), the fraction of particles remaining within the laser sheet is $F_O \approx 1 - \Delta y / w_{\text{laser}} = 0.79$. Consequently, the product of these parameters is $N_I F_I F_O \approx 15 > 7$. Meeting this criterion ensures that the correlation peak dominates random correlation noise, providing sufficient particle density for accurate velocity vector determination.

3.3 Flow Characterization

3.3.1 Crossflow velocity profile and boundary layer

Once the PIV parameters are defined, it is essential to characterize the flow in which the JICF develops, particularly the boundary layer, which governs the initial interaction between the crossflow and the jets. The boundary layer is the region adjacent to the wall where the crossflow velocity decreases due to viscous effects, as illustrated schematically in Fig. 3.9. Previous studies have highlighted the strong influence of the boundary layer on JICF interactions [43, 55]. When the injector nozzle is flush with the wall, the jet issues directly into the boundary layer, interacting with the near-wall low-momentum region. This configuration alters the jet trajectory and promotes the development of shear-layer instabilities close to the wall. Conversely, an elevated injection position allows the jet to bypass the boundary layer, leading to a different trajectory and vortex dynamics (see section 2.2.3). The boundary-layer thickness therefore needs to be evaluated.

Figure 3.10 presents the measured crossflow velocity profile without jets, at an air mass flow rate of 3.72 g/s, corresponding to a theoretical free-stream velocity $U_\infty = 1.2$ m/s within a 50.8×50.8 mm square test section, yielding a Reynolds number of $Re_\infty = 4060$. The mean bulk flow profile was obtained by spatially and temporally averaging four independent datasets acquired along the linear jet array. Each dataset consisted of 1000 double images

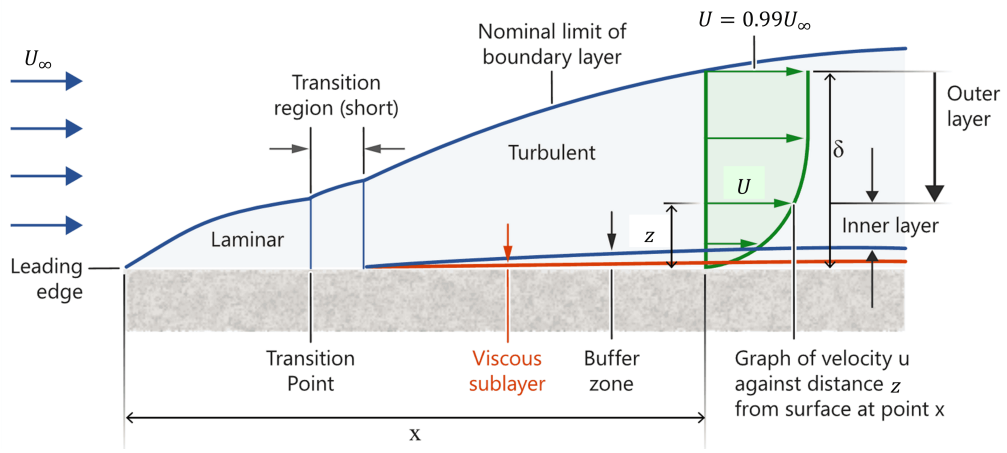


Figure 3.9 Schematic of boundary layer theory showing laminar-to-turbulent transition and the associated velocity profile, adapted with permission from [105]

captured over one second (1 kHz) using PIV, ensuring that the resulting mean velocity profile is consistent throughout the entire array of jets. Velocity fluctuations over the mean velocity profile are quantified using the RMS of u, represented as error bars. The experimental maximum crossflow velocity reaches $U_{\infty,\,\mathrm{max}} = 1.55$ m/s. Excluding the effect of Δt on the bulk flow velocity (see subsection 3.2.3), the discrepancy between this experimental value and the analytical crossflow velocity U_∞, arises from the development of the boundary layer, which reduces the effective flow area and accelerates the fluid locally. By accounting for these effects through spatial integration, the mean measured crossflow velocity is $U_{\infty,\,\mathrm{exp}} = 1.27$ m/s.

To characterize the bulk velocity profile, several analytical fits were tested. The classical n-power law, $u(z) = z^{1/n}$, commonly applied to fully developed laminar channel flows, fails to capture the measured crossflow profile, due to the high Re_∞. A significantly better agreement is obtained using a hyperbolic tangent formulation, inspired by analytical descriptions of crossflow profiles in cylindrical chambers [106], and adapted here to match the square-channel configuration :

$$u(z) = U_{\infty,\,\mathrm{max}} \tanh\left(e\frac{z}{H}\right), \tag{3.10}$$

where e controls the slope steepness and $H = 50.8$ mm corresponds to the duct height. A least-squares fitting algorithm is applied, and a value $e = 8.9$. The boundary-layer thickness δ is defined here as the height at which the mean velocity reaches 99% of the bulk crossflow velocity U_∞. The boundary layer thickness at the jet exit reaches $\delta_{99\%} = 13.3d = 9.3$ mm.

Additionally, turbulence intensity can be evaluated from the velocity profiles. It quantifies the relative magnitude of velocity fluctuations in the flow, providing insight into local mixing and

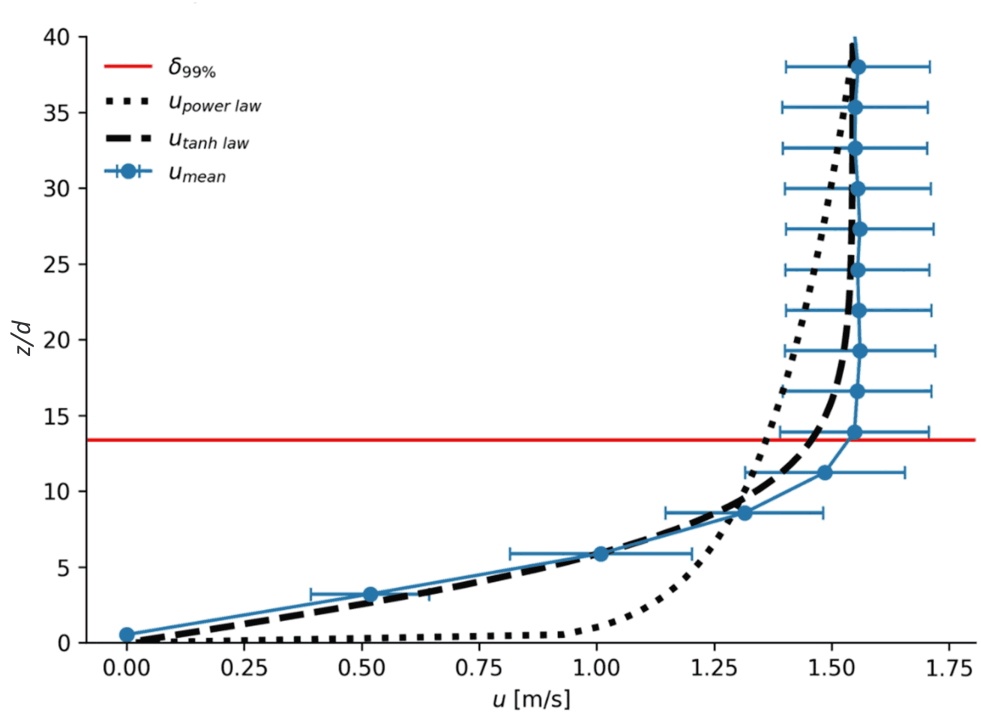


Figure 3.10 Measured crossflow velocity profile at the jet exit and averaged along the linear array, with analytical fits (power law and hyperbolic tangent) and the boundary-layer thickness $\delta_{99\%}$ at 99% of bulk velocity

momentum exchange. Higher turbulence levels have been shown to enhance jet penetration and jet–mainstream mixing [107], while reducing film cooling effectiveness due to increased mixing [108]. Turbulence intensity is defined as $I_{turb} = u'/\overline{u}$, where $\overline{u}$ is the mean flow velocity and u' is the RMS of the velocity fluctuations. It is highly sensitive to local perturbations, especially near jet exits, where it can reach 30–50% [42]. In the present configuration, the stabilization chamber is designed to damp turbulence. The measured turbulence intensity in the xz-plane is comparatively low, with $I_{turb} \approx 10\%$. In practice, this level is sufficient to slightly enhance shear-layer roll-up and small-scale vortical structures, promoting moderate mixing between the jet and the crossflow, while not significantly altering the overall jet penetration or the bulk velocity profile [107].

3.3.2 Advection and diffusion regimes

To assess whether tracking helium advection through droplet displacements is sufficient to characterize the mixing, the contribution of diffusion must be evaluated. Under the present flow conditions, the Péclet number based on a characteristic length scale on the order of the

jet diameter is defined as :

$$Pe = \frac{U_\infty d}{D_{\text{He-Air}}}, \quad \text{with } D_{\text{He-Air}} \approx 0.7 \text{ cm}^2/\text{s}.$$

Using typical crossflow velocities, this yields $Pe \approx 12 > 1$, indicating that advection dominates over diffusion. Taking a more conservative approach, the low-speed region in the boundary layer is considered. At $z/d = 3$, corresponding to the lower limit of the laser sheet, the local crossflow velocity is $U_\infty \approx 0.5$ m/s (see Fig. 3.10), and the small displacements observed in the PIV images (4 pixels ≈ 0.2 mm) correspond to $Pe \approx 1.4$. This indicates that advection remains the primary mixing mechanism, but diffusion can no longer be neglected. At even smaller length scales or lower velocities, diffusion becomes the dominant mixing mechanism, highlighting the intrinsic limitations of the present study.

3.4 Postprocessing techniques

Recorded images from the high-speed camera are treated with custom Python scripts to extract relevant jet trajectory and mixing metrics, and the LaVision DaVis 8.4.0 software for velocity–based metrics, such as velocity profiles, recirculation zones and Proper Orthogonal Decomposition (POD) analysis.

3.4.1 Frame intensity correction

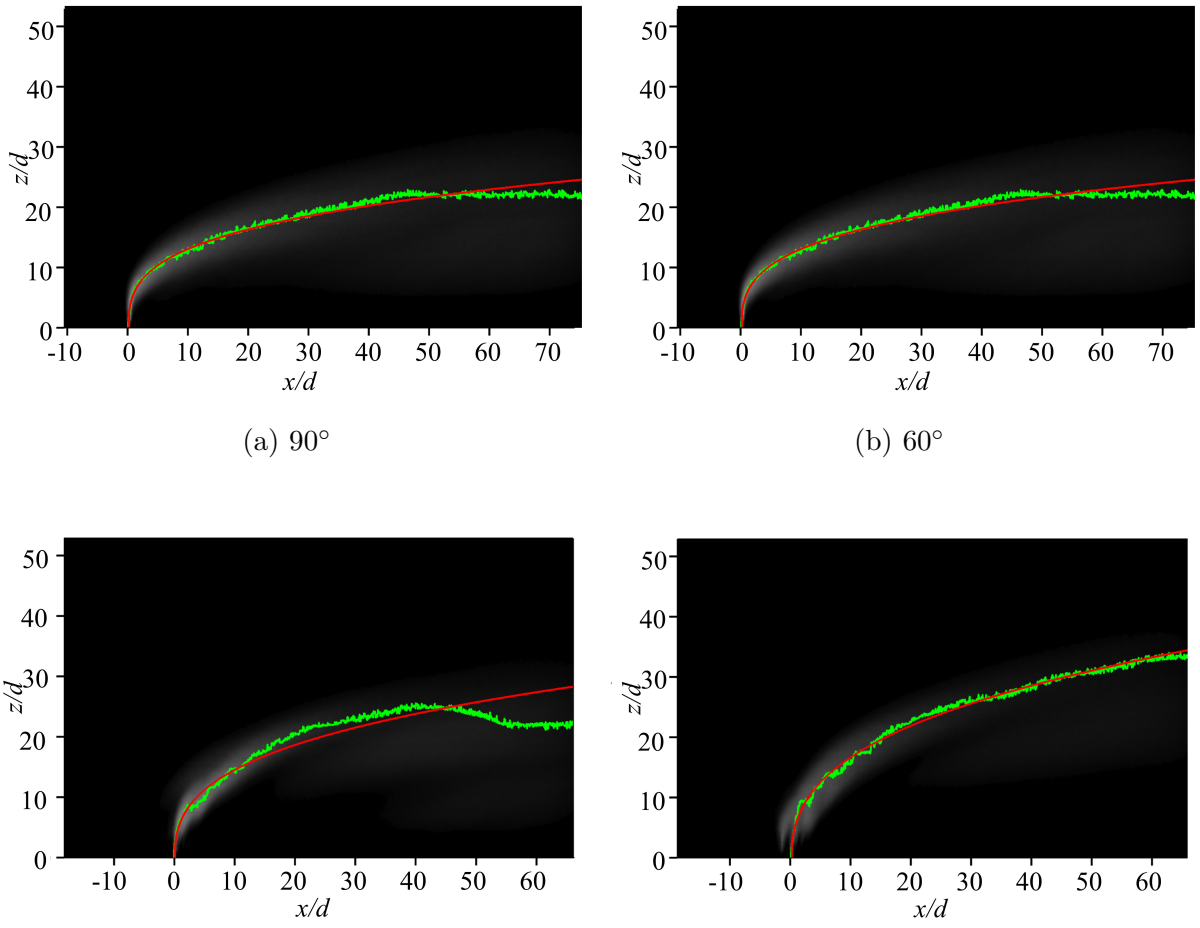
The acquired images are affected by several factors that may degrade data quality, particularly for quantitative mixing analysis. To reduce the influence of background illumination, an averaged background image $I_{\text{background}}$ over a 1 000 instantaneous background images is first subtracted from the raw intensity field I_{raw}. The resulting images are then corrected for spatial non-uniformities of the laser sheet (Fig. 3.6) by normalizing with the measured laser intensity profile I_{laser}. The correction procedure is expressed in Eq. 3.11.

$$I = \frac{I_{\text{raw}} - I_{\text{background}}}{I_{\text{laser}}} \tag{3.11}$$

3.4.2 Operations on images

The corrected images are analyzed to extract the jet trajectory (penetration), the spread, and the concentration decay. Figure 3.11 illustrates the operations performed on a time-averaged JICF for the centerline calculation, for all angle configurations at $J = 25$. The jet trajectory is extracted by identifying the position of maximum light intensity (green curve) within the

vertical slices of the images, starting from the jet exit and going downstream (to the right of the images). To reduce measurement errors, particularly those induced by the CVP, which can transport illuminated particles below the nominal jet trajectory, the maximum intensity is searched within the local neighborhood, thus avoiding large jumps in position. For example, Figs. 3.11a, 3.11b, and 3.11c exhibit the centerline calculation going down in the far field due to the intensity brought by the CVP. In the near field, jet-jet interactions induces centerline miss calculation due to close jet proximity (Figs. 3.11c and 3.11d).



(a) 90° (b) 60°

(c) 45° (d) 30°

Figure 3.11 Centerline extraction from time-averaged velocity fields for all array angles at the 5$^{\text{th}}$ jet exit ($J = 25$). The jet trajectory obtained from the maximum intensity (green) is fitted to the JICF scaling law (red)

To minimize these deviations, a fitted curve (red) is calculated along the maximum intensity centerline (green). This curve is obtained using a least-squares fit to the jet trajectory

(Eq. 2.5) and is subsequently used for comparing the different cases.

Jet spread is evaluated along directions perpendicular to the fitted centerline, as shown in Fig. 3.12. The local tangent to the centerline is first determined from the fitted trajectory, after which intensity profiles are extracted along the corresponding normal directions to quantify the jet width across downstream positions. A new local coordinate system is defined along the centerline, where ξ stands for the centerline direction and w for the orthogonal direction. Additional image corrections are applied to account for variations in droplet size and prevent misrepresentation of the mixing, as detailed in subsection 3.4.4.

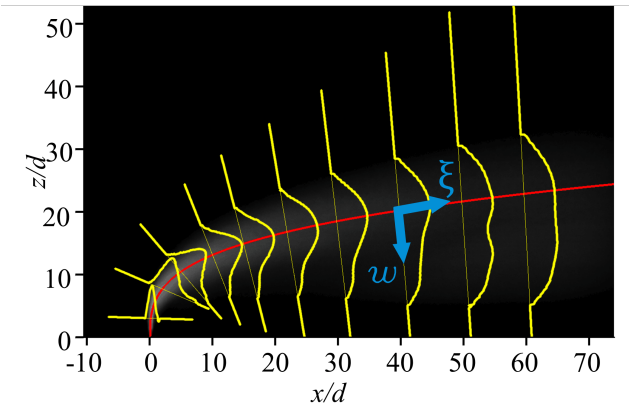


Figure 3.12 Centerline extraction from time-averaged intensity fields for the 90° case on a plane passing through the 5$^{\text{th}}$ jet exit and $J = 25$. Local coordinate system is aligned on the centerline direction (ξ) and the intensity distribution is calculated on the perpendicular branches (yellow) from the centerline, following the w-axis

Since advection dominates over diffusion in the mixing process, the large scale mixing can be estimated from the light intensity of the oil droplets, which accurately follow the flow. Accordingly, the mixing rate is evaluated from the decay of intensity along the jet centerline. To account for potential discrepancies between the fitted centerline and the actual location of peak intensity, the maximum intensity is extracted along each perpendicular line crossing the centerline.

3.4.3 3D Reconstruction

As described in Sec. 3.1.1, The final optical elements used to deliver the laser sheet to the test section are mounted on a translation mechanism to enable precise positioning relative to the jet exit. The acquired data are then used to reconstruct the jets, yielding a comprehensive 3D visualization of the jet-crossflow structures.

For this reconstruction, the processed images correspond to time-averaged flow fields aligned with the jet exits and the mid-planes between adjacent jets. The specific laser beam positions locations are detailed in Table 3.3. To ensure smooth rendering, intensity fields are processed with linear interpolation. This process results in a total of 8 planes aligned with the jets, 9 intermediate planes (including one at each boundary), and 16 interpolated virtual planes across the 8-jet linear array. The 30° configuration is an exception, where intermediate planes are omitted due to the close proximity of the jets in the spanwise (y) direction. The entire reconstruction is implemented using the PyVista Python module.

3.4.4 Unmixedness parameter

To evaluate mixing based on the dispersion of seeded oil droplets in the jets, images are first corrected. Because light intensity depends on particle size, which can vary due to seeding distribution or air friction, an initial binarization is performed to detect individual particles regardless of their size or emitted light. A sliding-average correction (4 pixels wide) is then applied to reconstruct a continuous intensity field, replacing the discrete black-and-white representation and allowing intensity decay evaluation and variance-based metrics, such as the unmixedness parameter, to reflect true advection part of mixing rather than being artificially maximized by purely black-and-white pixels. Consequently, variations in light intensity reflect local droplet density and, assuming negligible molecular diffusion, can be interpreted as variations in helium concentration.

The unmixedness parameter $\mathcal{U}$ quantifies mixing; the normalized variance captures the degree of inhomogeneity. After introducing the global form of $\mathcal{U}$ in Eq. 2.3, the detailed procedure for its evaluation at each cross section is :

$$\mathcal{U}_{yz} = \frac{1}{L_y L_z} \int_{L_y} \int_{L_z} \frac{\left(I - \overline{I}\right)^2}{\overline{I}\left(1 - \overline{I}\right)} \, \mathrm{d}y \, \mathrm{d}z, \tag{3.12}$$

where I denotes the pixel intensity normalized by the maximum intensity I_0 over the instantaneous image of size (L_y, L_z), and $\overline{I}$ represents the spatial mean intensity over the image. This global metric relies on the variance of the intensity relative to a common reference $\overline{I}/I_0$. To correctly compare different datasets, particularly when additional fuel mass is injected at varying J, images are padded with zero-intensity pixels to match the common intensity reference, following the methodology of Gevorkyan et *al.* [38]. Consequently, the unmixedness parameter, evaluated at different yz-plane cross-sections and over time, provides a quantitative measure of spatial mixing.

3.4.5 POD and spectral analysis

To further analyze the large amount of velocity field data obtained from PIV, Proper Orthogonal Decomposition (POD) is applied. POD is a statistical tool that decomposes the velocity fields into a set of orthogonal spatial modes, ranked by their energy content.

This method reduces the noise and small-scale fluctuations by retaining only the most energetic modes. It provides spatial eigenmodes across times, highlighting the energetic flow structures such as shear layers, recirculation regions, or vortex shedding, which govern mixing and jet trajectory. Finally, by taking into account only the most energetic modes, POD provides a compact representation of the flow dynamics, as illustrated in Fig. 3.13 [109].

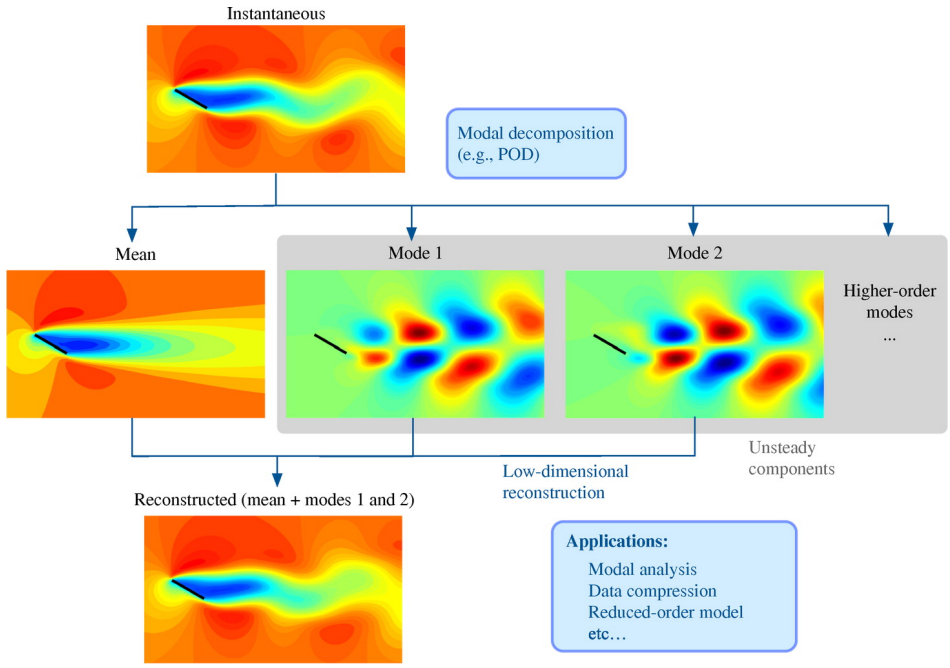


Figure 3.13 Concept of Proper Orthogonal Decomposition (POD): decomposition of an instantaneous flow field into dominant modes and reconstruction of an approximate flow using a truncated set of modes [109]

In the present study, POD is employed not only to extract coherent structures from the jet–crossflow interaction, but also to complement scalar-based mixing metrics by linking the identified velocity modes to regions of enhanced or hindered mixing. A frequency analysis is performed on the temporal coefficients of the spatial eigenmodes to quantify the characteristic eigen frequencies. These temporal coefficients are multiplied by a Hann window to reduce spectral leakage and enhance the clarity of peaks before performing a Fast Fourier Transform (FFT), which is applied to real, positive frequencies only. Given the acquisition frequency of 1 kHz, the analysis is limited to 500 Hz to prevent aliasing effect in accordance with the

Nyquist–Shannon theorem. Yet, additional experiments have been conducted at 4 kHz for the $yz-$plane of view to extend the spectral analysis up to 2 kHz. To reduce the amount of data to be analyzed, the investigation focuses on the most energetic spatial eigenmodes containing key phenomena, such as CVP and shear layer instabilities.

3.5 Parameter space covered

The jet-to-jet and jet-to-crossflow interactions were visualized from three perspectives: front ($yz-$plane), profile ($xz-$plane), and top ($xy-$plane) views. To capture the full flow dynamics, a series of 2D measurements was performed within these three planes. The positions of the measurement slices, expressed in jet diameters (d), are summarized in Table 3.3. For the front and profile views, measurements were taken both directly at the jet positions (represented by the 8 gray boxes corresponding to the 8 jets, numbered from the first jet encountered by the crossflow, $x/d = 0$, as shown in Fig. 3.4b) and in the inter-jet regions. Additional planes were included for the front view to improve spatial resolution. The top view was investigated extensively for the 30° jet array configuration and more coarsely for the remaining angles. Two seeding strategies were employed in this study. In the first configuration, only the jets were seeded in order to perform mixing analyses. In the second configuration, both the jets and the crossflow were seeded to enable the computation of velocity fields in the different planes of view.

Table 3.3 Slice positions for front, profile and top planes of view with their corresponding normals, respectively x/d, y/d, and z/d, for different injector angles (values converted to jet diameters, $d = 0.7$ mm, rounded to 1 decimal). Jet positions are indicated by shaded boxes

Views	Front (x/d)				Profile (y/d)				Top (z/d)			
Angles	30°	45°	60°	90°	30°	45°	60°	90°	30°	45°	60°	90°
Slice positions	0.0	0.0	0.0	0.0	-1.0	-0.7	-0.9	-1.0	0.0	0.0	0.0	0.0
	0.8	0.6	0.5	1.2	0.0	0.0	0.0	0.0	0.7	0.7	0.7	0.7
	1.6	1.3	0.9	3.0	1.0	0.6	0.9	1.0	2.1	2.1	2.1	2.1
	2.6	2.1	1.5	4.8	2.0	1.3	1.7	2.0	3.6	3.6	3.6	3.6
	3.5	2.9	2.0	8.5	3.0	2.0	2.6	3.0	5.0	5.0	5.0	5.0
	4.3	3.5	2.5	13.9	4.0	2.7	3.4	4.0	6.4	8.6	8.6	8.6
	5.1	4.3	3.0	21.2	5.0	3.4	4.3	5.1	7.9	12.1	12.1	12.1
	6.0	5.0	3.5	/	6.0	4.2	5.2	6.2	9.3	15.0	15.0	15.0
	6.7	5.6	4.0	/	7.0	4.9	6.0	7.1	10.7	/	/	/
	7.7	6.4	4.5	/	8.0	5.6	6.9	8.1	12.1	/	/	/
	8.6	7.1	4.9	/	/	6.2	7.7	9.1	13.6	/	/	/
	9.5	7.7	5.4	/	/	6.9	8.6	10.0	15.0	/	/	/
	10.3	8.4	5.9	/	/	7.6	9.4	11.0	16.4	/	/	/
	11.2	9.1	6.4	/	/	8.3	10.3	12.0	19.3	/	/	/
	11.9	9.9	6.9	/	/	9.0	11.1	13.0	22.1	/	/	/
	12.5	10.5	7.5	/	/	9.7	11.8	13.9	25.0	/	/	/
	13.2	11.2	8.1	/	/	10.5	12.7	14.9	/	/	/	/
	15.0	12.9	9.9	/	/	/	/	/	/	/	/	/
	16.8	14.9	11.8	/	/	/	/	/	/	/	/	/
	20.5	18.5	15.4	/	/	/	/	/	/	/	/	/
	25.9	23.8	20.8	/	/	/	/	/	/	/	/	/
	33.2	31.1	28.1	/	/	/	/	/	/	/	/	/

CHAPTER 4 RESULTS & DISCUSSION

4.1 Qualitative assessment of the jets–crossflow interaction

The interactions of linear arrays of 8 jets with the crossflow are described for each array angle configurations. Analyses are crossed through three complementary planes of view, providing a qualitative description of the flow structures.

4.1.1 Profile view

The profile view, commonly investigated for single JICF configurations, provides a side perspective of the jet from its injection in the channel to its downstream development within the crossflow. In the present study, the middle jets (4^{th} and 5^{th} in the array, see Fig. 3.4b) are mainly studied as they are the least affected by boundary effects. Figure 4.1 shows a typical profile view of the instantaneous image for the 5^{th} jet in the 90° array at $J = 10$, highlighting the main flow structures: the Counter-rotating Vortex Pair (CVP) consisting of two adjacent vortices with opposite rotation forming downstream of the jet exit on leeward side and Kelvin-Helmholtz (KH) instabilities due to velocity gradients in the shear layer on the windward side. Often referred to as Von Kármán-like structures in jet wakes, these

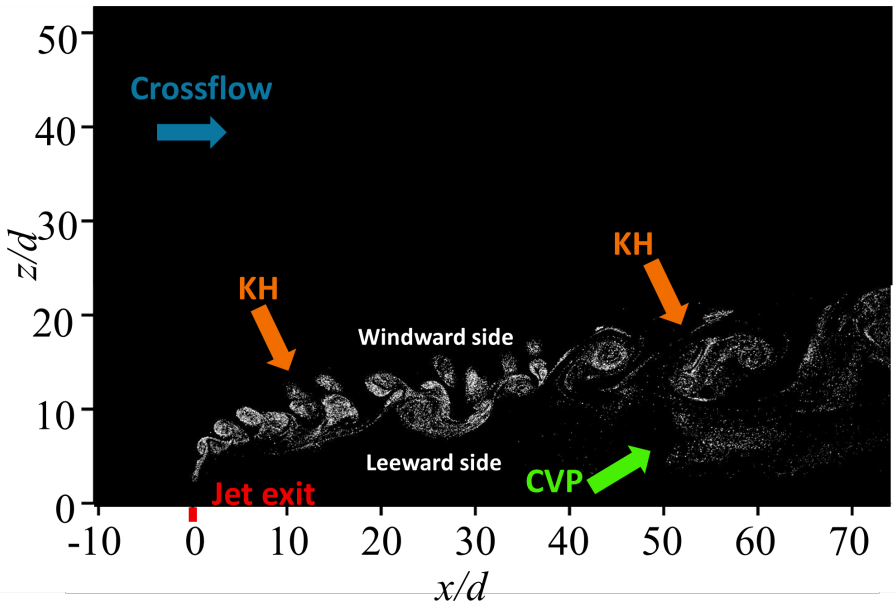


Figure 4.1 Typical profile view of JICF for the 5th jet of the 90° angle array. Positions of KH instabilities and the CVP are shown qualitatively

structures are located on the upper left regions of the images. Additionally, the density ratio S being strongly different than unity in the configurations studied here, contributes to shear-layer instabilities related to the Rayleigh–Taylor (RT) mechanism. In practice, these instabilities are difficult to distinguish clearly from KH instabilities and will, therefore, be discussed collectively as shear-layer instabilities.

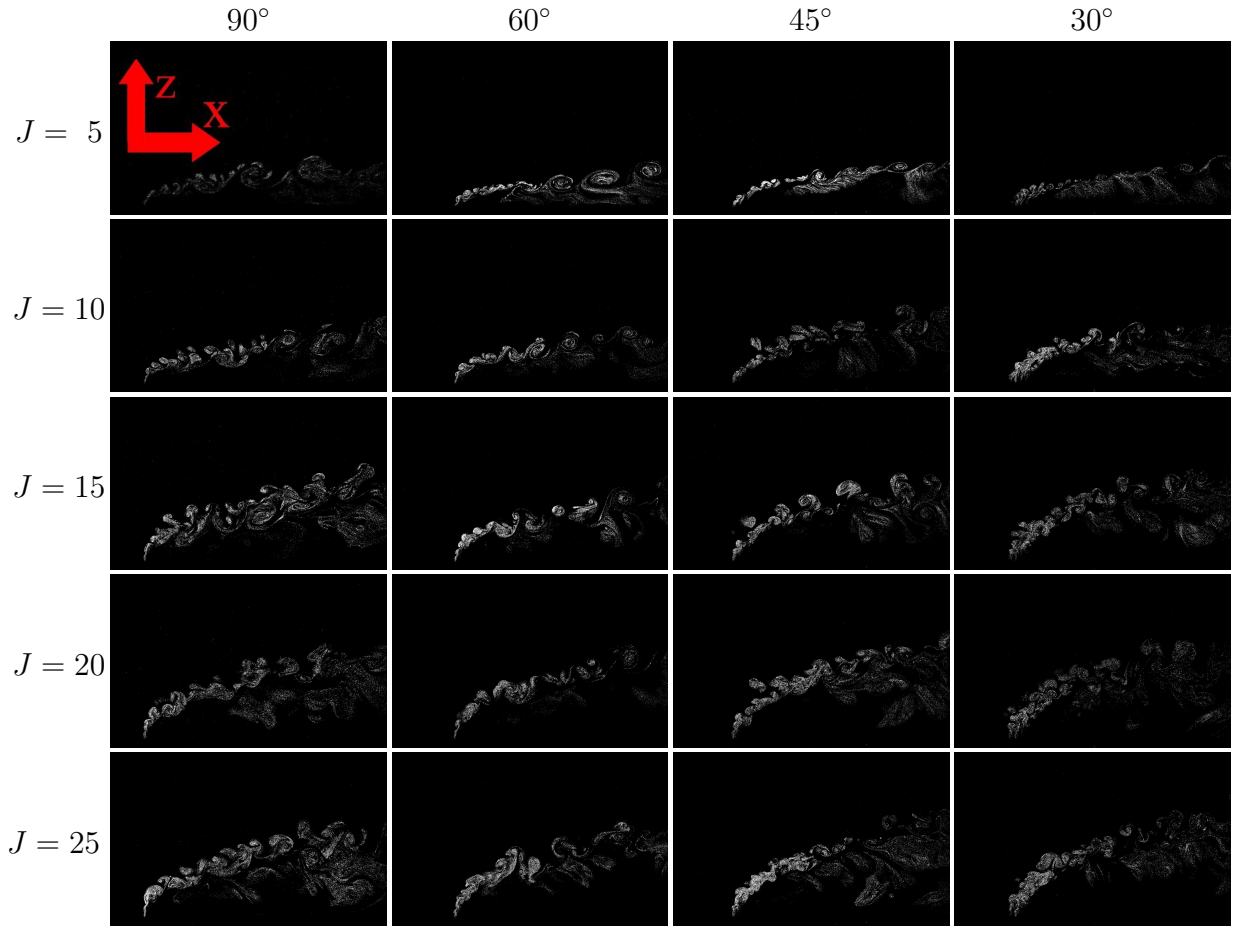


Figure 4.2 Instantaneous flow profiles in the xz-plane for different array angles and momentum flux ratios (J). Variations in jet penetration, vortical structures, and the extent of unmixed regions beneath the jet trajectory are observed across the array configurations and J values.

The JICF for different values of J and array angles is shown in Fig. 4.2, with columns representing array angles and rows corresponding to the jet-to-crossflow velocity ratio J. The crossflow bends the jet trajectory, leading to increased penetration into the crossflow as J increases. At $J = 5$, the jets remain close to the wall, within the boundary layer, characterized by $\delta_{99\%}/d = 13.3$ at the jet exit. In contrast, higher values of J result in a significant vertical displacement of the jet core. The influence of the array angle on jet penetration at a given J remains unclear, as no consistent trend is observed.

The interaction between the jet and the CVP in the far field promotes vertical spreading of the jet and seems to increase with J, as the mixing zone becomes wider. It is consistent with the jet regime classification proposed by Karagozian [55]: jets with $J \leq 5$ are typically associated with film-cooling applications, while jets with $J \geq 20$ are characteristic of mixing-dominated configurations.

Yet, a systematically black region, corresponding to an unmixed zone persists on the leeward side of the jet in the near field. Its extent increases with the momentum ratio J and more pronounced flow separation at higher J. This behavior is associated with the development of a recirculation zone that limits scalar exchange in this region.

Additionally, increasing J enhances turbulence and promotes the breakdown of flow structures. At low J, coherent vortices form on the windward shear layer. Near the jet exit, small-scale structures develop and, as they interact with the jet core, merge into larger coherent vortices, particularly evident for $J = 5$. As J increases, these structures become less distinct and progressively break down into smaller scales due to the higher turbulence (higher Re_j).

These structures are also influenced by the array angle, with lower angles promoting the breakdown of large-scale vortices. Pronounced shear layer instabilities are observed for all angles at $J = 5$, whereas at $J = 10$, only the 90° and 60° cases retain distinct large-scale structures. For $J > 10$, these differences become less pronounced. This behavior is linked to the reduction in spanwise jet spacing s_y as the array angle decreases (see Tab. 3.2). In particular, the 30° configuration ($s_y/d = 1$) exhibits additional jets directly at the exit for all J in Fig. 4.2, shortening the interaction distance between adjacent jets and promoting earlier jet-to-jet interactions, which enhances turbulence.

4.1.2 Top view

Figure 4.3 presents instantaneous top-view visualizations of the four configurations at $J = 10$, highlighting the breakdown of large-scale structures as a function of the array angle. The images are taken at three elevations above the injection plane: $z = 2$, 5, and 7.5 mm (corresponding to $z/d = 2.8$, 7.1, and 10.7, respectively). Jet array holes are visible in the background to indicate jet positions. For clarity, only 8 jets are shown in each configuration: in the angled arrays, the used jets lie along the 16-hole linear array, while in the 90° case, they correspond to the first row (left side) of the grid of injection holes.

The angled configurations (30°, 45°, and 60°) introduce pronounced asymmetry in the flow, unlike the symmetric 90° case. The CVP leg on the leading-jet side (upper part of the images)

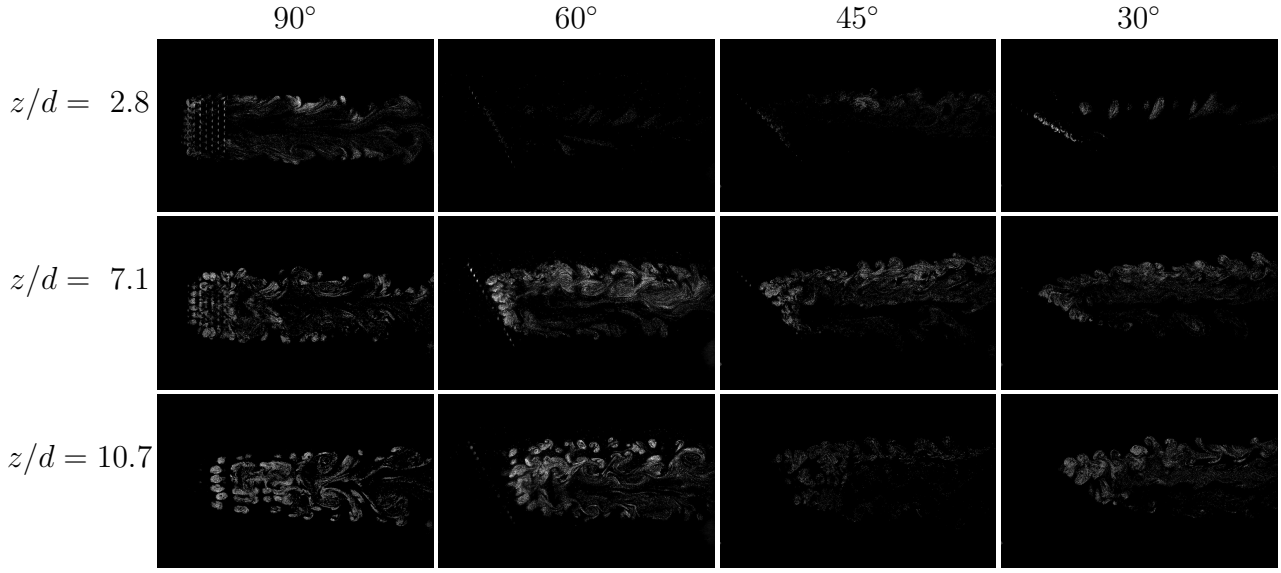


Figure 4.3 Instantaneous top view ($xy-$plane) at various heights for different array angles at $J = 10$

is consistently stronger and lower than its trailing-jet counterpart. In the 30° and 45° cases, one leg appears at $z/d = 2.8$ while the other emerges at $z/d = 7.1$; at 60°, the trailing leg is barely visible at low elevation. This asymmetry also affects the global orientation of the jet array: at $z/d = 10.7$, the 90° case shows a symmetric spanwise spread about $y = 0$, whereas smaller angles produce enhanced spreading along the array direction and reduced spreading in the opposite direction, indicating that the jet array progressively aligns with the array orientation rather than the purely axial trajectory.

The array angle also promotes the breakdown of large-scale coherent structures, as initially observed in the profile view analysis. For the perpendicular jet array (90°), the jet-crossflow interaction at high elevations ($z/d = 10.7$) is dominated by KH vortices forming along the windward shear layer, visible as distinct bubble-like patterns. However, as the array angle decreases, these KH structures progressively weaken and ultimately vanish, signaling the disruption of large-scale coherence in favor of smaller-scale turbulence.

At $z/d = 2.8$ for the 90° case and at $z/d = 7.1$ for the other array angles, an unmixed region is systematically observed downstream of the jet exit, in the near field region. Depending on the array angle, this region may be centered between adjacent jets (such as the 90° case) or slightly shifted laterally, highlighting the strong influence of jet orientation on the near-field flow topology.

4.1.3 Front view

Figure 4.4 presents cross-sectional views of the jet array for the four array-angle configurations (columns) at several downstream locations (rows), ranging from a plane passing through the 5^{th} jet to a location $x/d = 13.9$ downstream of the last jet.

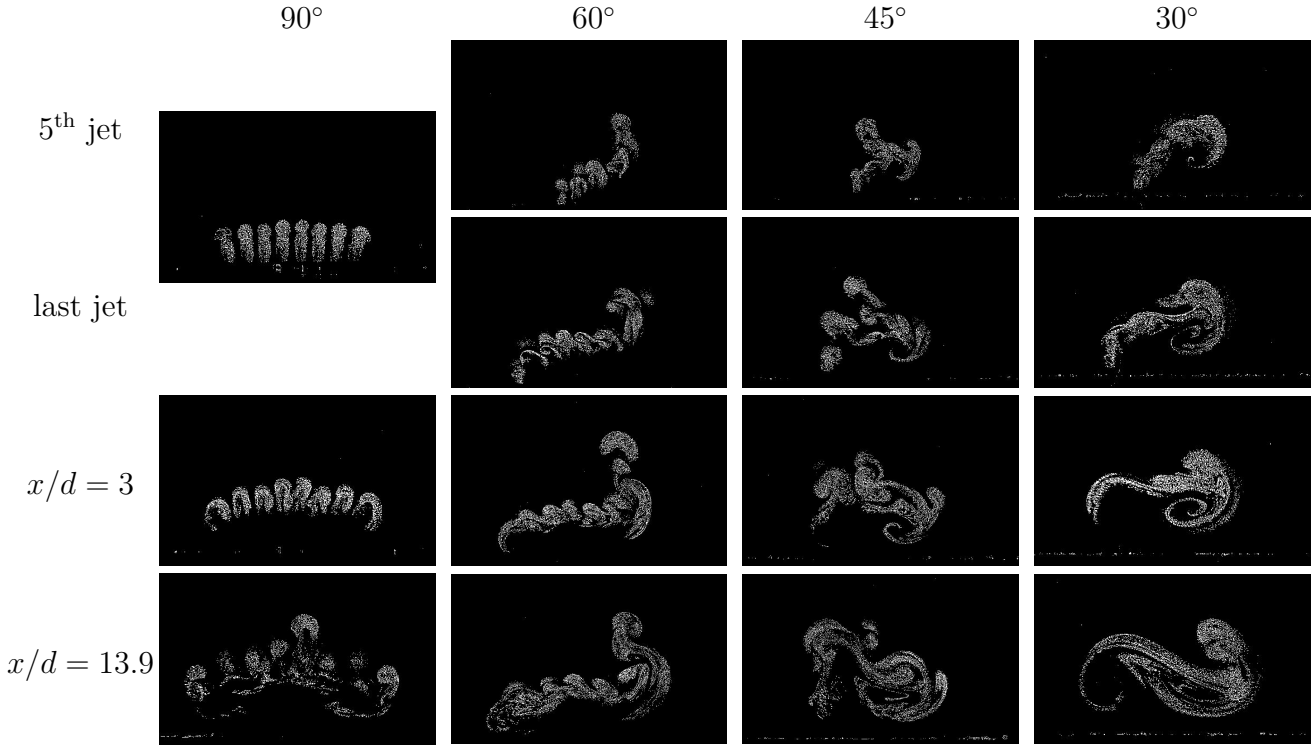


Figure 4.4 Instantaneous front views at various axial positions for different array angles at $J = 10$.

The angle degrades the organized flow structure where for the reference configuration (90°), individual jets remain clearly distinguishable even at $x/d = 3$. Further downstream ($x/d = 13.9$), the eight jets preserve a relatively organized structure compared to other angles. For the 60° configuration, the jets begin to merge as early as $x/d = 3$, and progressively lose their individual structure further downstream. At larger downstream distances, the jet structures become difficult to distinguish, indicating enhanced jet-to-jet interactions. For lower array angles (45° and 30°), the frontal jet-to-jet spacing becomes sufficiently small to induce strong interactions within the array itself. As a result, individual jets are no longer identifiable shortly downstream of the injection.

As the array angle decreases, asymmetry with respect to the xz center plane becomes increasingly pronounced. While the 90° configuration remains nearly symmetric, lower angles show early formation of the right CVP leg (leading-jet side, $y > 0$), appearing around $x/d = 3$

for 60° and already within the array for smaller angles (see 5$^{\text{th}}$ jet row). This imbalance strengthens the right vortex, causing a progressive lateral deflection of the jet and an S-shaped far-field trajectory.

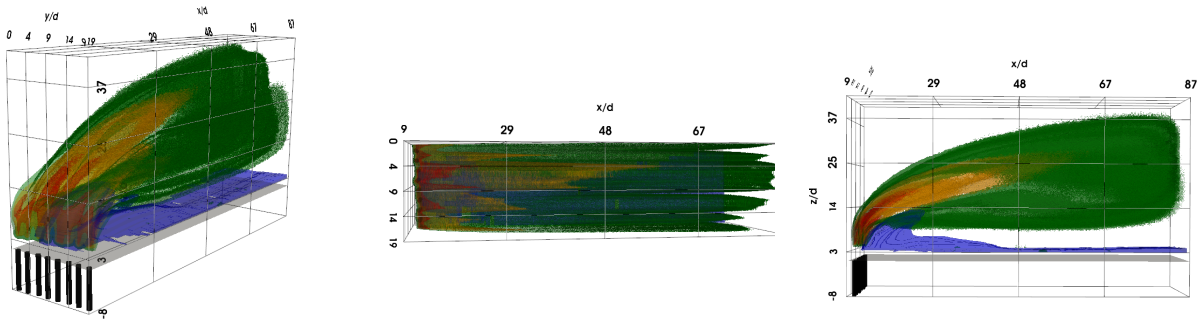
4.2 3D reconstruction

A sweep of the laser sheet position is performed to reconstruct the flow field in three dimensions. At each spanwise (y) location, time-averaged images are acquired and subsequently assembled and interpolated to obtain the full 3D reconstruction of the flow. Figure 4.5 presents the three-dimensional distribution of the normalized light intensity field for different array angles across J. Red, yellow, and green isosurfaces correspond to normalized light intensity levels of $I = 0.8$, 0.5, and 0.3, respectively, following Eq. 3.11. Since the light intensity is directly related to the concentration of seeded particles within the jets, these isosurfaces provide a representation of the helium distribution and mixing. The recirculation zone, defined by regions where the axial velocity satisfies $u < 0$ m/s, is shown in blue; jet locations are represented by black tubes; and the test section floor by a grey plate. A gap of approximately 2–3d between the floor and data is visible, corresponding to the region close to the bottom surface not illuminated to avoid reflection. The 3D reconstructions are displayed from three perspectives: isometric, top, and profile views.

All configurations exhibit a region of high intensity near the jet exits (red), corresponding to peak scalar concentration. As the jets mix with the crossflow, the concentration decreases downstream, transitioning from high-intensity regions (red/yellow) to more diluted zones (green). Greater dilution is observed in the far field at lower array angles, particularly for the 30° case, as seen in the profile views of the 3D representations where the less opaque green regions indicate a more uniform mixture. This earlier dilution suggests enhanced turbulence that breaks down large-scale structures, consistent with the previous profile, front, and top views. A quantitative analysis of this decay is provided in the following sections.

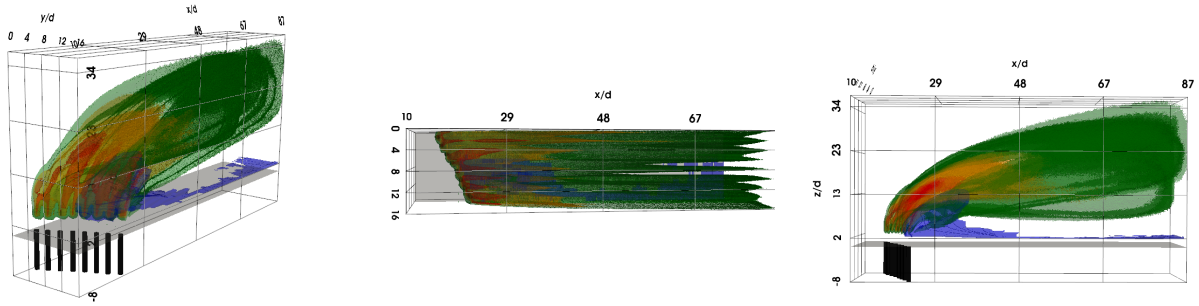
For the 90° array, the top and profile views show a symmetric intensity distribution, while the isometric view highlights greater penetration of the central jets compared to the boundary jets. As the array angle decreases, the flow becomes increasingly asymmetric. The isometric views further reveal a downstream shift of maximum penetration, from the 4$^{\text{th}}$–5$^{\text{th}}$ jets in the 90° case to the 5$^{\text{th}}$–6$^{\text{th}}$ jets at lower angles.

Additionally, the CVP leg on the side of the first jet is lower than that on the opposite boundary. This behavior is particularly pronounced for the smallest angle (30°), where the heights of the two CVP legs differ by $\Delta z/d \approx 11$ at the furthest downstream location shown



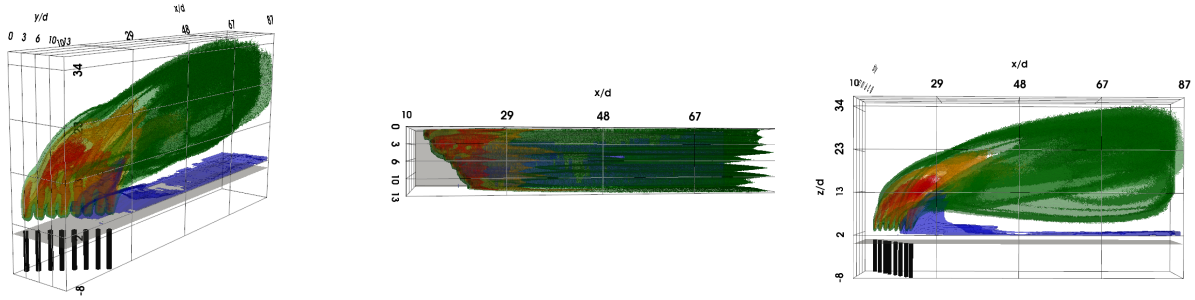
Isometric view | Top view | Profile view

Angle 90°



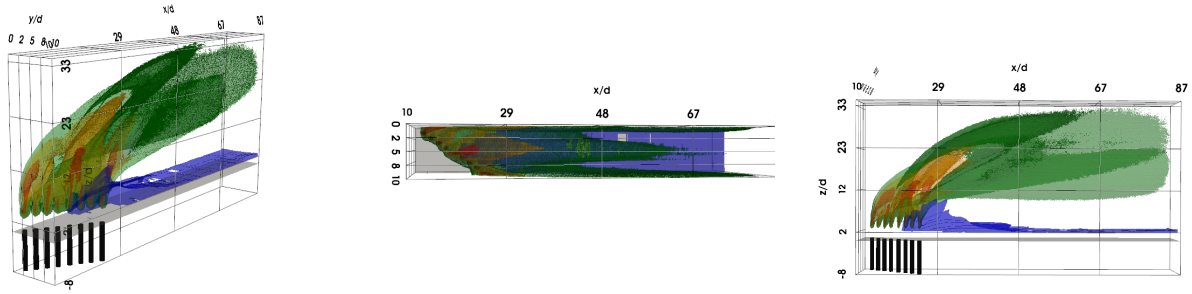
Isometric view | Top view | Profile view

Angle 60°



Isometric view | Top view | Profile view

Angle 45°



Isometric view | Top view | Profile view

Angle 30°

Figure 4.5 3D reconstruction of the time-averaged intensity fields and corresponding recirculation zones at $J = 25$ for all array angles, shown from isometric, top, and profile views. Red, yellow, and green isosurfaces represent normalized intensity levels of $I = 0.8$, 0.5, and 0.3, respectively, while the blue region highlights the recirculation zone.

in the 3D profile view plot.

In addition to the jet–crossflow mixing, the recirculation zone is highlighted in the 3D reconstructions (blue). This region is attached immediately downstream of the jet exit for all configurations. The profile views indicate that higher array angles (90° and 60°) produce a more extended recirculation region in the spanwise direction. This is attributed to the larger spanwise jet spacing, which increases flow blockage and enhances crossflow deviation around the jets. A detailed analysis of the influence of J and the array angle on the size of the recirculation is provided in section 4.4.

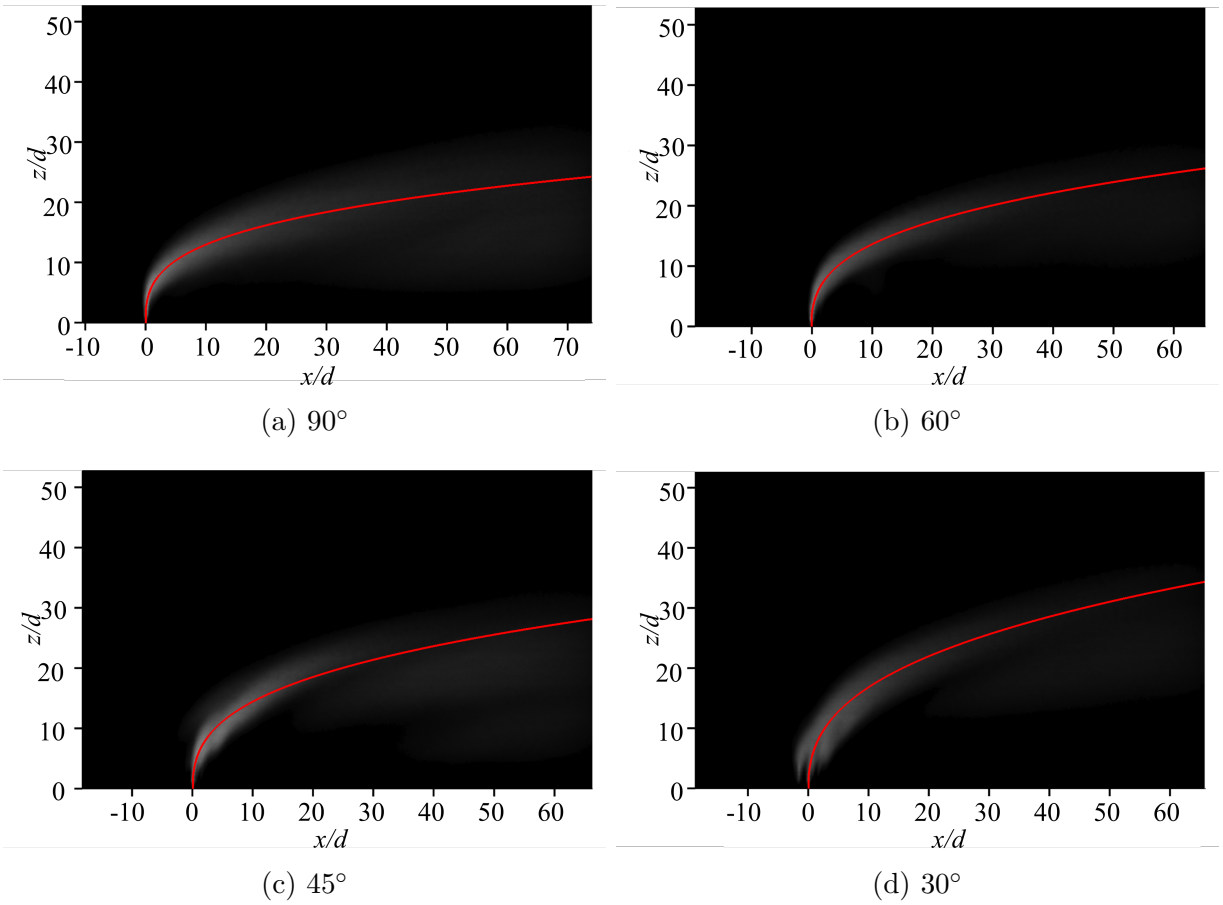
4.3 Jet penetration

Controlling the trajectory of jets within the combustion chamber of gas turbines is a critical aspect of the design of jet-in-crossflow (JICF) mixing systems. Jet penetration directly governs the spatial distribution of fuel and oxidizer, the resulting mixing efficiency, and the risk of undesirable phenomena such as jet impingement on the combustor walls. Understanding how the jet trajectories are modified by the jet pattern, injection angle, and operating conditions is therefore essential to assess both mixing performance and mechanical constraints.

The jet centerline trajectories are analyzed within the framework of scaling laws developed for a single jet in crossflow (SJICF), following Eq. 2.5. Figure 4.6 shows an example of the fitted jet centerline (red) superimposed on the time-averaged image on a plane passing through the 5^{th} jet in the array at $J = 25$, for each array angle configuration. These time-averaged images provide insight into the jet–jet interactions, which are particularly evident for the lower array angles (45° and 30°). The close proximity between jets induces additional flow components that modify the jet structures, including changes in the windward and leeward sides due to the influence of the upstream and downstream jets, respectively. These interactions can lead to merging and the formation of complex three-dimensional jet trajectories. Therefore, the analysis focuses primarily on the penetration of the jet array at a representative location rather than on individual jet trajectories.

4.3.1 Penetration along the arrays

The effect of the asymmetry introduced by the array angle can first be assessed by examining the jet penetration along the array. Figure 4.7 presents the jet centerline penetration measured in profile planes across the arrays for all angle configurations at $J = 25$. To enable comparison of the penetration at equal downstream distances from the jet exit x_j, the penetration curves were collapsed onto a single reference point: the jet exit. This correction is



(a) 90° (b) 60°

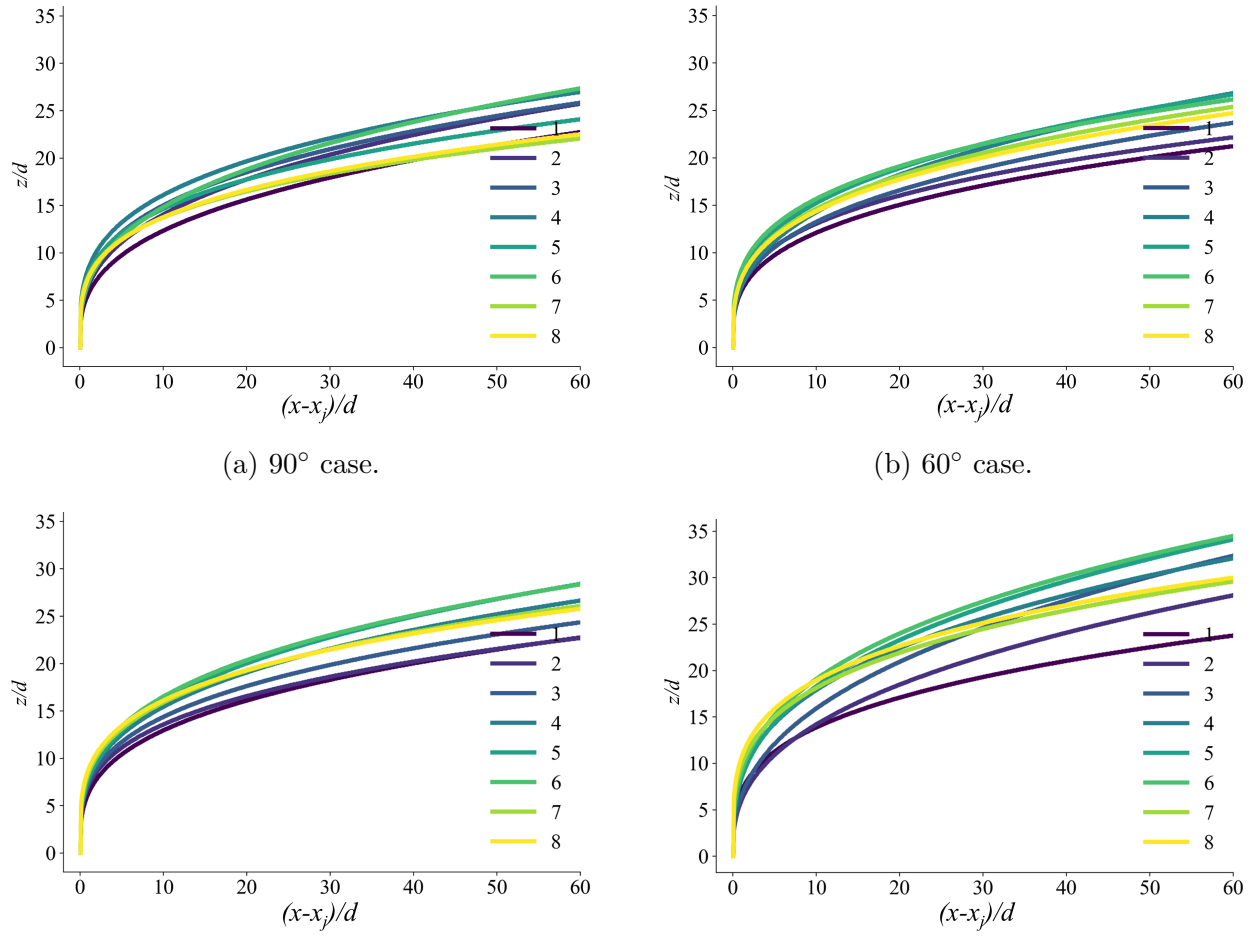
(c) 45° (d) 30°

Figure 4.6 Time-averaged images of the 5$^{\text{th}}$ jet of the array for different injection angles at $J = 25$. The solid red line indicates the fitted jet centerline extracted from intensity levels.

required for array angles other than 90°, for which $s_x \neq 0$.

For the 90° configuration, jet trajectories are highly symmetric about the array centerline. Jets located symmetrically about the mid-plane follow nearly identical paths, with similar penetration heights and downstream evolution (e.g., jets #1–#8, #2–#7). This symmetry agrees with the instantaneous top- and front-view observations in Figs. 4.3 and 4.4. Maximum penetration occurs for the central jets, suggesting a symmetric deflection of the crossflow toward the array boundaries. As the array angle decreases, asymmetry develops between jets. The leading jet (#1) exhibits reduced penetration, while the trailing jet (#8) penetrates further. This behavior resembles tandem jet configurations reported in the literature, where upstream jets partially shield downstream jets from the crossflow, effectively increasing their local momentum ratio and penetration [71–73].

Consequently, the location of maximum penetration shifts from the central jets (#4–#5)



(a) 90° case.

(b) 60° case.

(c) 45° case.

(d) 30° case.

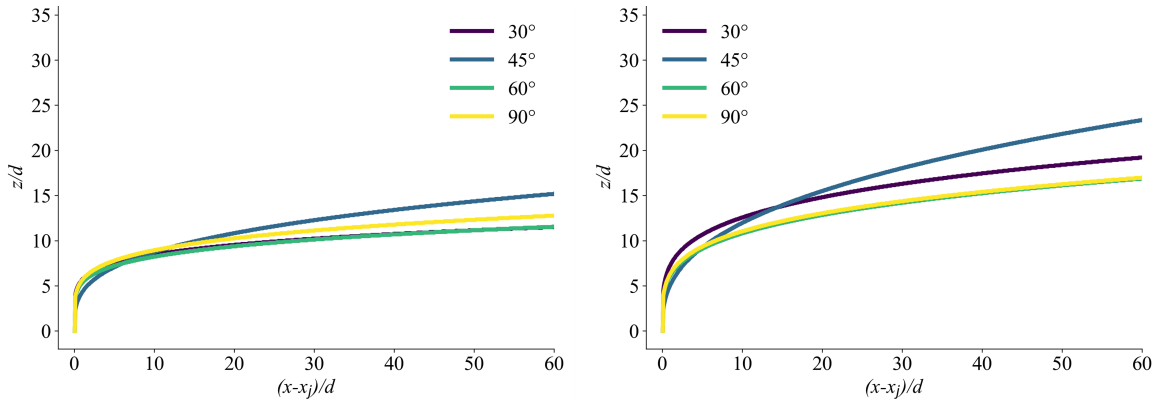
Figure 4.7 Fittings of the jet centerline penetration measured at each jet exit (#) for the (a) 90° and (b) 60° (c) 45° and (d) 30° configurations at $J = 25$

in the 90° case toward jets #5–#6 at lower angles. To ensure consistent comparison while minimizing boundary effects, the penetration analysis, therefore, focuses on jet #5 across all array angles and momentum ratios J.

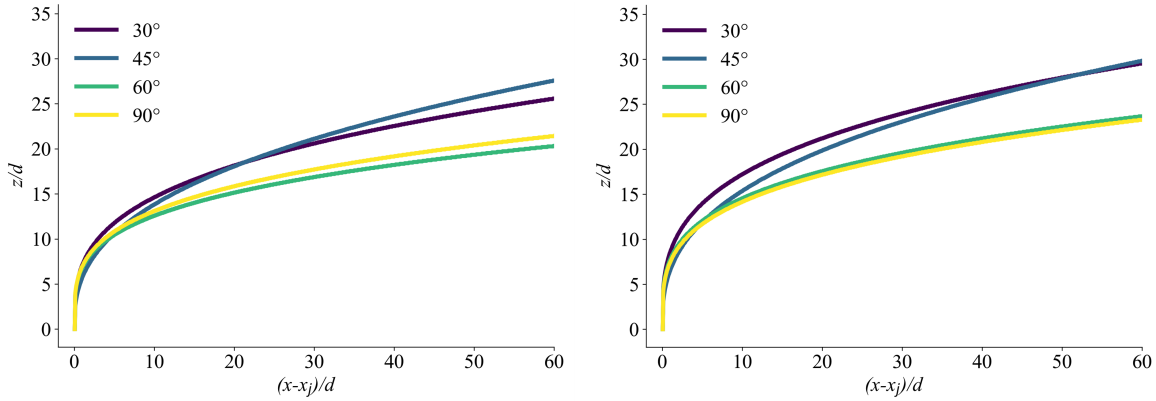
4.3.2 Influence of the array angle

The effect of the array angle is analyzed by comparing the penetration on a plane passing through jets at different J as shown in Fig. 4.8.

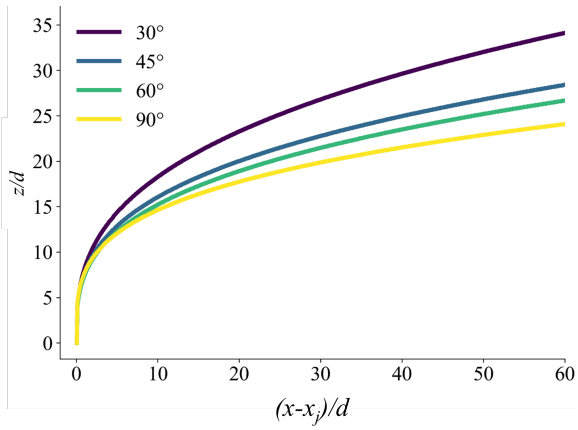
The influence of the array angle becomes increasingly pronounced at high J. At $J = 25$, the trajectories corresponding to different angles are clearly separated, whereas this distinction diminishes as J decreases. At low J (e.g., $J = 5$), the jet trajectories nearly collapse.



(a) $J = 5$ (b) $J = 10$



(c) $J = 15$ (d) $J = 20$



(e) $J = 25$

Figure 4.8 Comparison of centerline trajectories in the plane aligned with jet #5 for different array angles and momentum flux ratios ($J = 5$ to 25)

Lower array angles systematically promote greater penetration across all J. The 30° configuration exhibits the highest penetration at $J = 25$, significantly exceeding that of the other geometries. In contrast, the 45°, 60°, and 90° configurations result in progressively lower penetration, with a slight additional reduction at larger angles. For lower J, this trend is not strictly monotonic, as the 45° configuration can exhibit comparable or even greater penetration than 30°, particularly for $J \leq 15$.

This behavior is attributed to the reduced frontal jet-to-jet spacing, s_y, at lower injection angles, which enhances shielding effects and effectively decrease the local crossflow momentum experienced by downstream jets. The merging of trajectories between array angles at low J can be explained by the insufficient momentum imparted by the leading jet to sustain a significant shielding effect on the downstream jets. In back-to-back configurations, the leading jet is typically strong enough to induce such effects for $R \gtrsim 2$ [72, 73]. In the present case, although $R = 6$ for the low-J condition, the injection angle reduces the effective interaction between jets, limiting the development of shielding and leading to similar trajectories across all configurations.

The non-monotonic penetration observed for the 45° array can be attributed to differences in jet-merging behavior across array angles. As shown in Fig. 4.4, the lowest angle (30°) promotes early jet merging within the array, leading to a coherent cross-sectional structure. In contrast, for the 90° configuration, merging occurs only farther downstream, maintaining distinct jet structures over a longer distance. At intermediate angles, partial merging produces localized jet reinforcement. For instance, in the 60° case, the leading jets are reinforced, whereas in the 45° configuration an additional lifted structure appears near the center of the array. This behavior suggests that circulation between adjacent jets can persist, lifting the merged structures and increasing penetration. Further analysis is required to fully characterize the underlying physical mechanisms.

4.3.3 Influence of the momentum flux ratio

The influence of J is examined for the 5^{th} jet of the array. Figure 4.9 shows the centerline trajectories measured in the profile plane aligned with the 5^{th} jet exit for the 30° array, for momentum flux ratios ranging from $J = 5$ to $J = 25$. A clear increase in jet penetration with increasing J is observed, consistent with classical single-jet behavior.

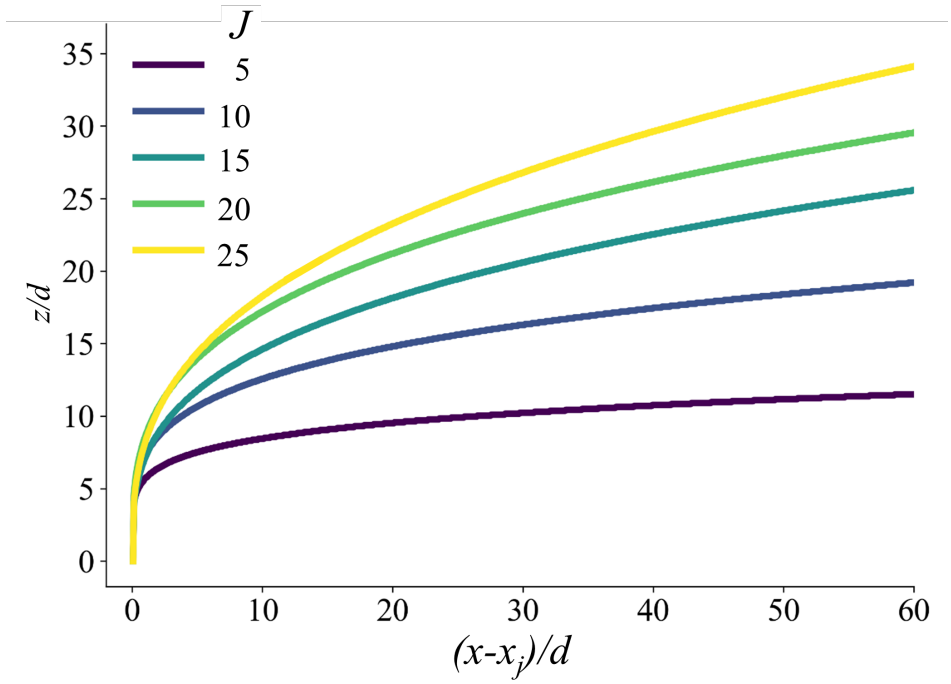


Figure 4.9 Centerline trajectories in the plane aligned with jet #5 for the 30° array, for momentum flux ratios $J = 5$–25

Scaled trajectory laws

To further investigate the influence of J on the jet trajectory for the different array angles, the coefficients of the fitted power-law are analyzed. The evolution of the scaling coefficient A and the exponent B is plotted as a function of J for the different trajectory scalings (d, Rd, and Jd) introduced previously in Section 2.2.2 (note that for a constant density ratio S, the velocity ratio satisfies $R \propto \sqrt{J}$). This approach allows identification of the non-dimensional parameter that most strongly governs the jet-array trajectory.

Rather than recalculating the trajectory coefficients for each scaling, the coordinate axes are rescaled accordingly. Based on the d-scaled trajectory law (Eq. 2.5), the relationships between the different scalings can be written as:

$$\frac{z}{d} = A_d \left(\frac{x}{d}\right)^{B_d} = R\, A_{Rd} \left(\frac{x}{Rd}\right)^{B_{Rd}} = J\, A_{Jd} \left(\frac{x}{Jd}\right)^{B_{Jd}}. \tag{4.1}$$

Here, A_d, A_{Rd}, and A_{Jd} denote the scaling coefficients associated with the d-, Rd-, and Jd-scalings, while B_d, B_{Rd}, and B_{Jd} represent the corresponding exponents.

Since the equality holds for all x, the coefficients can be identified term by term, yielding the

following relationships between the scaling coefficients:

$$A_d = A_{Rd} R^{1-B} = A_{Jd} J^{1-B}, \qquad B_d = B_{Rd} = B_{Jd} = B. \tag{4.2}$$

Using these relationships to rescale the trajectory centerlines, the results are shown in Fig. 4.10: (a) for the d-scaling (similar to Fig. 4.8); (b) for the Rd-scaling; and (c) for the Jd-scaling.

As expected, the d-scaling does not collapse the trajectories, with penetration increasing for higher J. In contrast, the Rd-scaling provides a good collapse for the 45° and larger array angles, while the 30° array still shows higher penetration at large J, indicating under-scaling. The Jd-scaling exhibits an inverted trend: lower J appears to penetrate deeper, reflecting over-scaling for the larger angles, including 45°. For the 30° array, the Jd-scaled data also show this inversion but are more collapsed than with the Rd-scaling. Overall, the Rd-scaling appears to offer the most consistent collapse across the array angles, consistent with the literature [43, 54, 55].

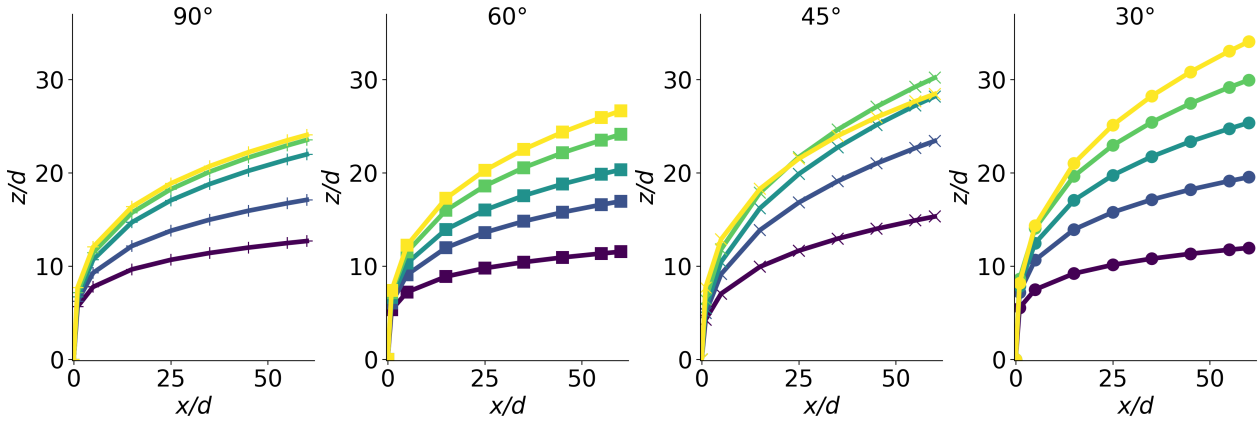
A quantitative assessment of the trajectory coefficients is presented to evaluate the effectiveness of each scaling and the corresponding trajectory laws. Figure 4.11 shows the evolution of the coefficients with J for all array angles: (a) the scaling coefficient A and (b) the exponent B. A fit curve is included for each scaling group, obtained by averaging the coefficients across all angles at each J, to highlight the overall scaling trend.

Three distinct trends emerge for the coefficient A (Fig. 4.11a). For the d-scaling, A_d increases with J, indicating a stronger apparent penetration when no additional normalization is applied. For the Rd-scaling, A_{Rd} remains nearly constant, exhibiting only a weak linear dependence on J. For the Jd-scaling, A_{Jd} decreases nonlinearly as J increases. The fitted trends for each group of scalings (averaged over all array angles) are given by:

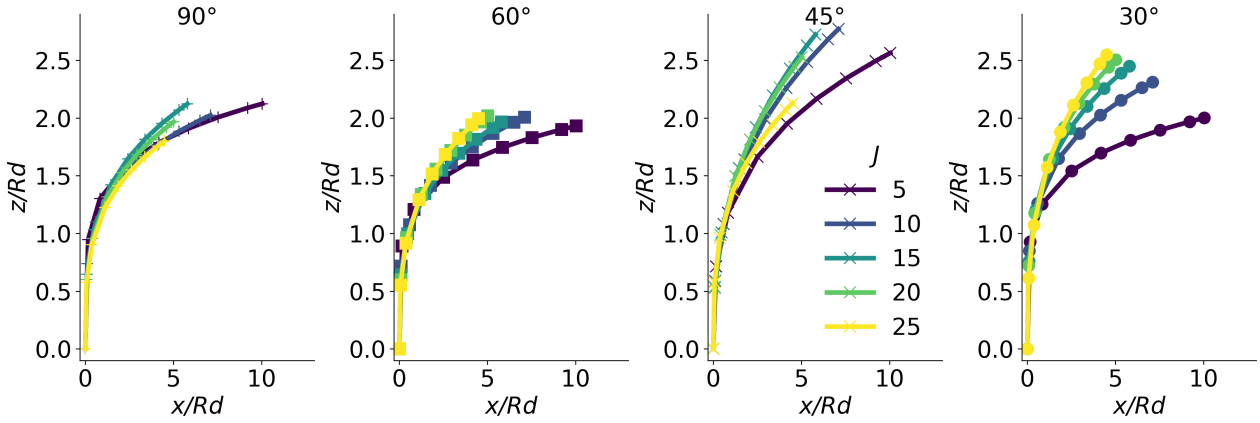
$$\begin{aligned} A_d &= -3.0 \times 10^{-3} J^2 + 2.1 \times 10^{-1} J + 4.3, \\ A_{Rd} &= 9.1 \times 10^{-3} J + 1.2, \\ A_{Jd} &= 2.0 \times 10^{-3} J^2 - 7.4 \times 10^{-2} J + 1.8. \end{aligned} \tag{4.3}$$

Among the three scalings, the Rd-scaling is characterized by an almost negligible quadratic contribution ($\ll 10^{-3}$) and a relatively small linear coefficient. This very weak dependence on J suggests that scaling with Rd efficiently compensates for variations in momentum ratio, yielding a more universal form of the trajectory law.

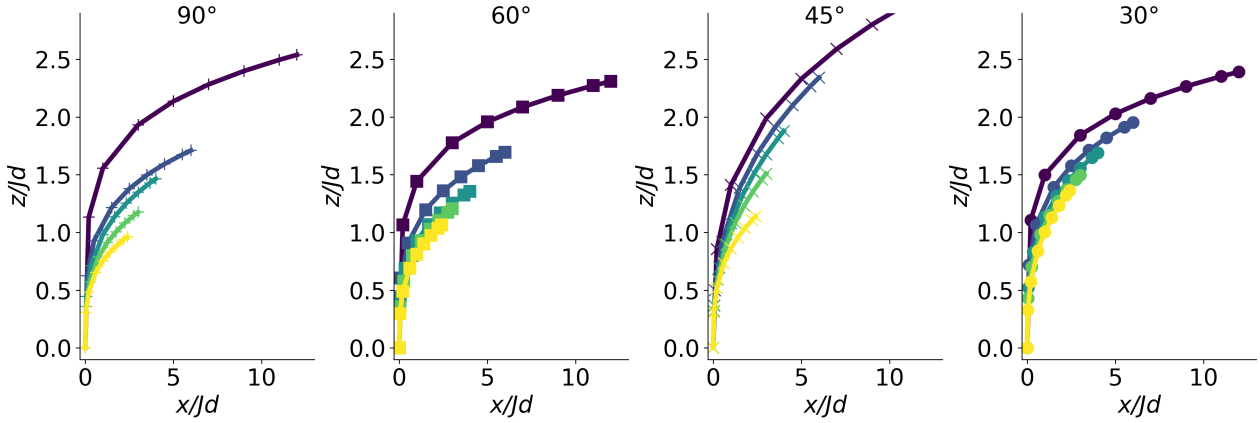
Within each scaling, the 30° configuration consistently exhibits the highest A values, while



(a) d-scaling.

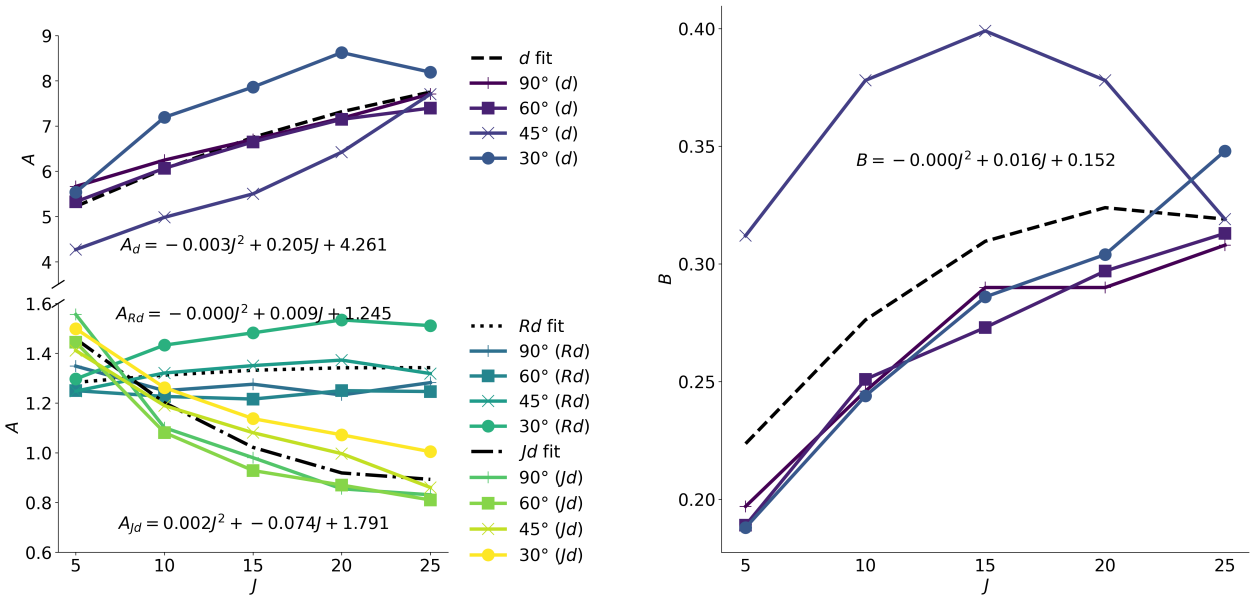


(b) Rd-scaling.



(c) Jd-scaling.

Figure 4.10 Scaled trajectories of the 5$^{\text{th}}$ jet across different array angles and momentum ratios J (a) d-scaling; (b) Rd-scaling; (c) Jd-scaling



(a) Scaling coefficient A

(b) Scaling exponent B

Figure 4.11 Evolution of the scaling coefficients A and B for the different trajectory scalings (d, Rd, Jd) as functions of the array angle and J. Polynomial fits are applied to each scaling and shown as black curves.

larger angles show lower values (except for the d-scaled 45° case, discussed below). Physically, the coefficient A governs the overall penetration amplitude: larger A corresponds to deeper jet penetration into the crossflow. This trend aligns with the trajectory profiles previously reported, where the 30° array produces the strongest penetration.

The exponent B governs the curvature of the trajectory: larger values of B correspond to a weaker bending of the jet trajectory. On the one hand, the increase of B until $J \leq 15$, therefore, implies to a reduced bending of the trajectory, which is consistent with the stronger jet momentum relative to the crossflow. On the other hand, the 45° configuration produces jets that are less deflected by the crossflow compared with the other angles. However, this configuration also exhibits a smaller scaling coefficient A (see the d-scaling in Fig. 4.11a), indicating a lower penetration strength near the jet exit. This behavior is consistent with the trajectories shown in Fig. 4.8, where the 45° case displays a lower vertical trajectory near the jet exit together with a reduced curvature. At $J = 25$, the coefficients A and B become similar for all angles, which explains the nearly identical trajectories observed at this momentum ratio. As discussed previously in Subsection 4.3.2, this distinctive behavior likely results from differences in jet merging and crossflow circulation, which modify the lifting and interaction of the jet structures.

A global fit of the exponent evolution across the array angles, therefore, yields the following relationship:

$$B = 1.6 \times 10^{-2} J + 0.16. \tag{4.4}$$

Overall, the R_d scaling provides the best agreement with the experimental results and can be expressed as follows :

$$\frac{z}{Rd} = A\left(\frac{x}{Rd}\right)^B, \qquad A = 9 \times 10^{-3} J + 1.245 \text{ and } B = 1.6 \times 10^{-2} J + 0.152. \tag{4.5}$$

4.4 Velocity field analysis

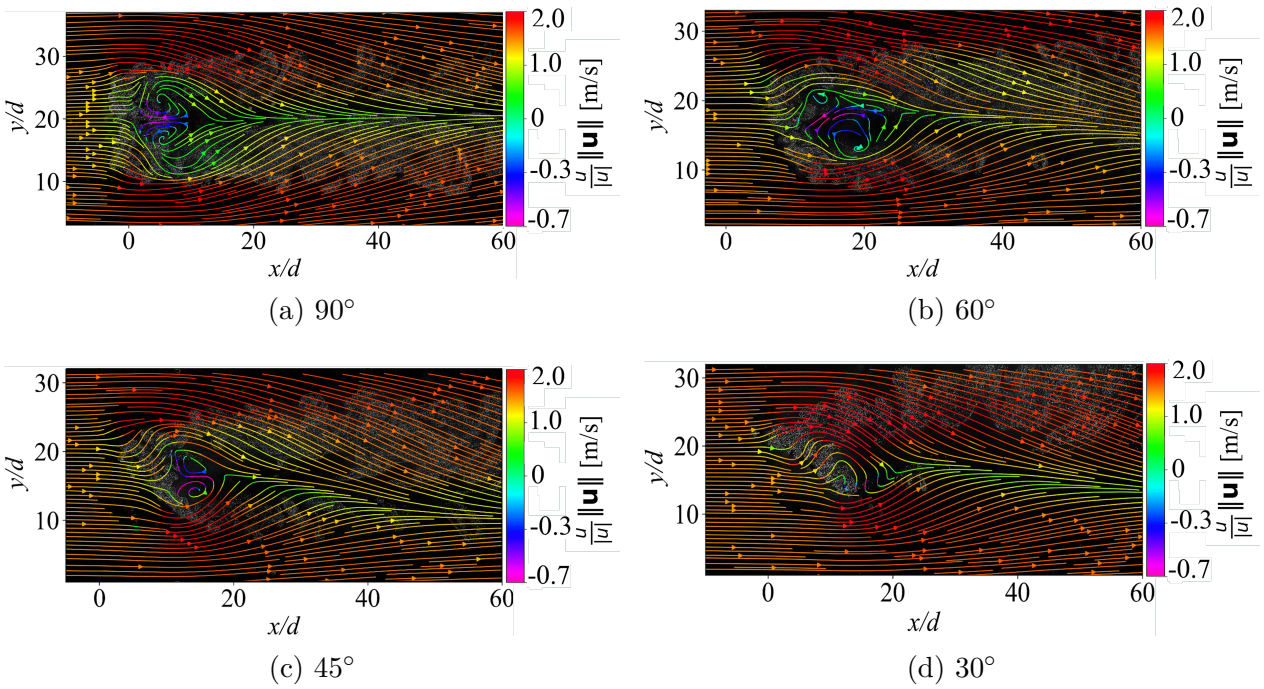
The array angle significantly alters the flow behavior, leading to notable variations in jet penetration. In particular, the central jet within the array interacts with a deflected crossflow on the windward side due to shielding effects, while a recirculation zone develops on the leeward side. These combined effects strongly influence the jet trajectory and overall mixing characteristics. The following section aims to quantify the velocity fields in order to better understand the underlying flow mechanisms governing these interactions, with a particular focus on the shielding effect and the recirculation zone and their impact on jet penetration and mixing.

4.4.1 Streamlines of the flow

The influence of the array angle on the flow is analyzed though Fig 4.12, which shows the top-view time-averaged streamlines of the flow overlaid on an instantaneous image at $z/d = 7$ for $J = 25$ and all array angles. The streamline color map represents the velocity magnitude in the xy-plane, $\|\mathbf{u}\| = \sqrt{u^2 + v^2}$, with the sign given by the axial velocity component u.

The asymmetry induced by the array angle significantly affects the streamlines of the flow and, therefore, its global direction. In Fig. 4.12a, the far field region remain symmetrical relatively to the jet array. As the array angle decreases, the direction of the CVP is deflected, in the same direction as the array.

The streamlines reveal the flow behavior upstream of the jet array. For the 90° configuration, the jets act as a strong frontal obstruction, causing significant crossflow deviation around the array. This deflection is accompanied by a marked reduction in the local velocity at the jet interface, dropping to $\lesssim 1.0$ m/s. As the array angle decreases, the effective frontal spacing between jets narrows, and the array becomes more streamlined relative to the crossflow. Consequently, the flow is less deflected and remains more aligned, resulting in higher local



(a) 90° (b) 60°

(c) 45° (d) 30°

Figure 4.12 Top-view time-averaged streamlines overlaid on an instantaneous image at $z/d = 7$ for $J = 25$ and all array angles. The streamline color map represents the velocity magnitude in the yz-plane, $\|\mathbf{u}\| = \sqrt{u^2 + v^2}$, with the sign given by the axial velocity component u.

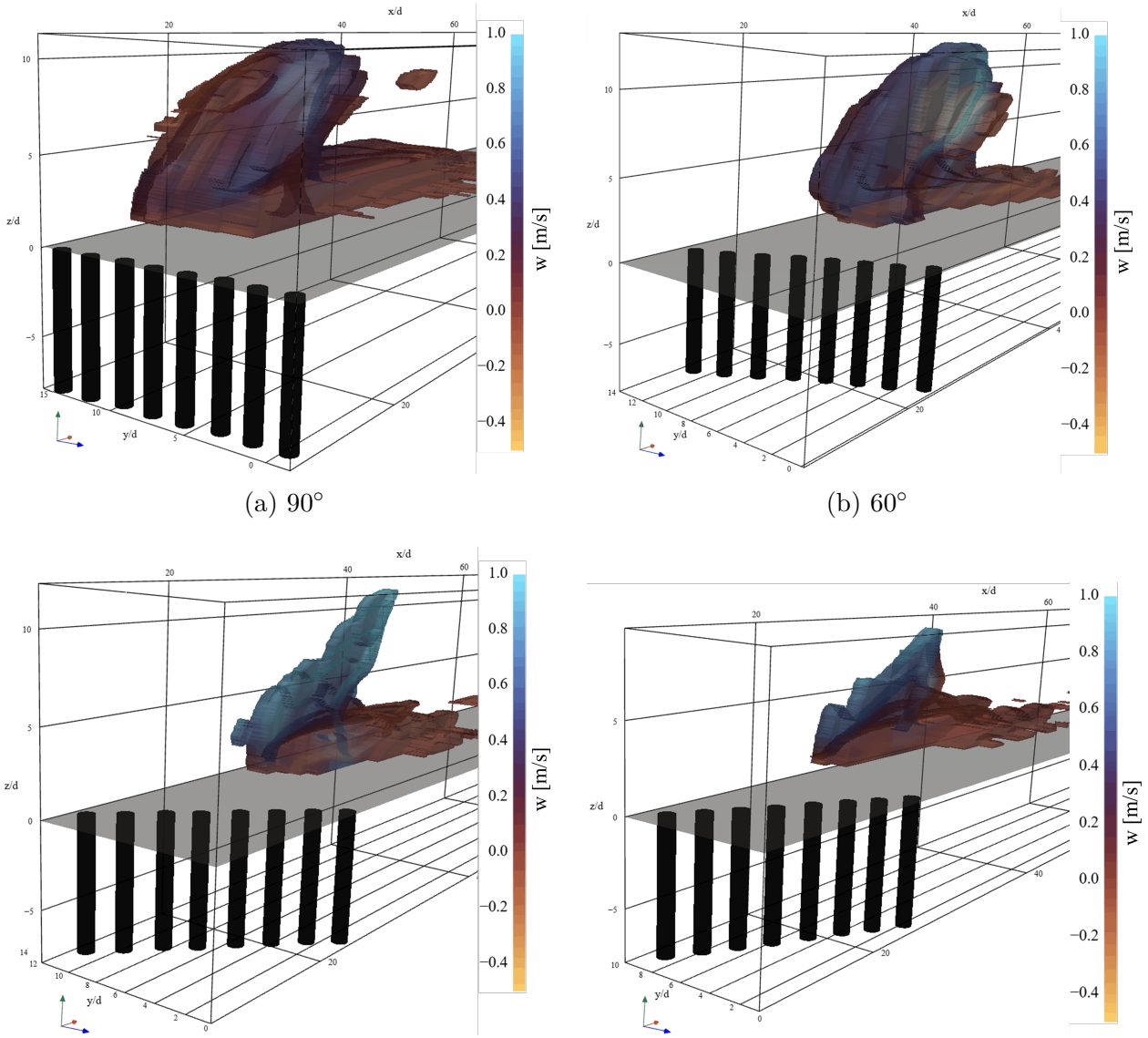
velocities at the jet interface, reaching up to 1.3 m/s for the 30° configuration.

Along a streamline, the observed velocity reduction in the 90° case reflects a conversion of kinetic energy into static pressure, associated with local deceleration and flow deflection. As the crossflow decelerates from approximately 1.55 m/s far upstream to $\lesssim$ 1.0 m/s near the center of the array, the jets experience a stronger opposing pressure field, promoting jet bending. In contrast, lower array angles induce weaker flow deceleration and reduced blockage, resulting in a less constrained crossflow environment. This allows the jets to retain more of their momentum and penetrate further into the crossflow compared to higher-angle configurations, as discussed in Sec. 4.3. This behavior can be interpreted as a form of shielding: at lower array angles, the reduced frontal exposure of the jets to the crossflow limits the effective interaction, thereby mitigating momentum loss and enhancing penetration.

4.4.2 Reverse flow and recirculation zones

In Fig. 4.12, recirculation zones (closed streamline loops) are observed for array angles larger than 30°. An asymmetry is evident in the size of the recirculating vortices, with downstream vortices being larger, while the reference 90° case exhibits a more symmetric pattern. The

smallest array angle (30°) shows only a weak reverse flow and does not form a fully closed recirculation region. This indicates that the flow reattaches quickly behind the jets, as also visible from the streamlines curving around the jet array. While such recirculation zones can contribute to flame stabilization, they correspond to unmixed regions, as evidenced by the instantaneous images shown in the background.



(a) 90° (b) 60°

(c) 45° (d) 30°

Figure 4.13 3D reconstruction of the time-averaged recirculation zone at $J = 25$ for all array angles. The color map represents the vertical velocity component, w.

To characterize these negative-velocity regions, the velocity fields are obtained from time-averaged PIV measurements in the streamwise–vertical plane of the jets (xz, profile view).

Reverse and recirculation zones are defined as areas where the streamwise velocity satisfies $u < 0$ m/s. By scanning the jet array with the laser sheet and camera, a volumetric reconstruction of the reverse region is obtained, as shown in Fig. 4.13. The color map represents the vertical velocity component, w. Jet locations are indicated by black cylinders, and the test section floor is represented by a horizontal grey plane.

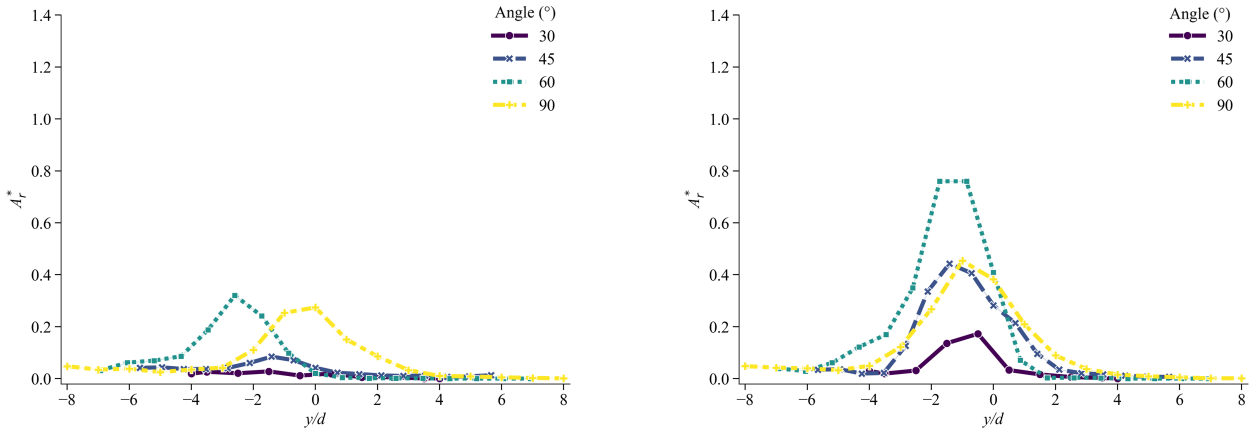
The array angle strongly influences the extent of the reverse-flow regions. Larger array angles lead to more extended recirculation zones, ellipsoid-like in shape. In contrast, the low-angle configuration (30°) exhibits a thinner recirculation region, also ellipsoid-shaped, but less elongated in the vertical (z) direction. While the width of the recirculation zones is largely determined by the frontal length of the jet array, leading to wider zones for larger array angles, the height appears influenced by the vertical momentum distribution of the jets and the interaction with the crossflow.

Interestingly, the deep penetration observed for the 30° configuration does not correspond to a taller recirculation zone along the z-axis behind the jets. Instead, it appears to result from higher local crossflow velocities and reduced upstream flow deflection, combined with the limited reverse-flow regions downstream, as discussed above.

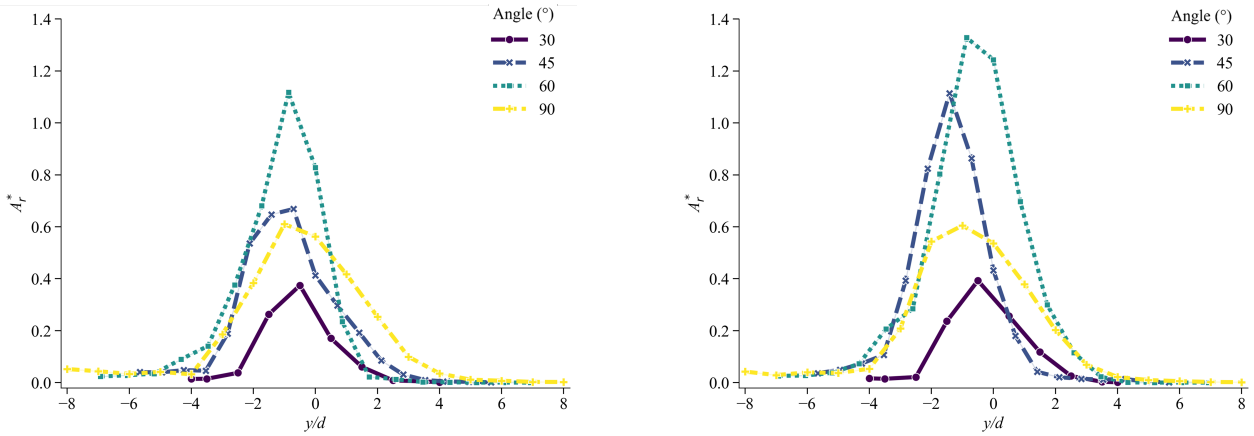
Figure 4.14 presents the evolution of the reverse zone area as a function of J and array angle, defined as the region where the axial velocity satisfies $u < 0$ m/s. The measurements are obtained in the profile view for different streamwise planes, including both jet exit planes and inter-jet planes for all array angles except 30°. The area of the recirculation zones are reported as the normalized recirculation area A_r^*, using the recirculation area of the 90° array at $J = 25$ as the reference case. A larger value of A_r^* indicates a more extended recirculation zone in the streamwise (x) and vertical (z) directions, while elevated values over a wider range reflect a broader recirculation region in the transverse (y) direction.

The recirculation zone is influenced by J and the array angles. Increasing J increases the recirculation area for all array configurations. At low momentum flux ratios, the reverse zone is more pronounced for large array angles (60° and 90°), whereas low-angle configurations exhibit either very weak or nearly absent recirculation across the array. This behavior is primarily attributed to geometric effects: low-angle arrays present a reduced frontal blockage of the crossflow, allowing it to more easily bypass the jet structure along the array edges. This trend is consistent with the top-view PIV measurements shown in Fig. 4.12.

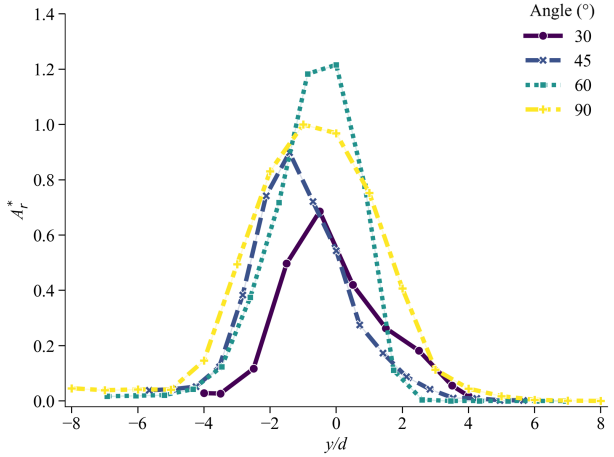
Additionally, in tandem jet configurations, the confined recirculation zone forming between successive jets is known to enhance the penetration of downstream jets by reducing their exposure to the incoming crossflow. In the present study, however, recirculation alone does not fully explain the increased penetration observed at low array angles. In particular, the 30°



(a) $J = 5$ (b) $J = 10$



(c) $J = 15$ (d) $J = 20$



(e) $J = 25$

Figure 4.14 Recirculation area in the xz-plane as a function of the spanwise position (y) for different angles and values of J. The area is normalized by that of the 90° case at $J = 25$.

configuration exhibits the weakest recirculation while simultaneously achieving the highest penetration. This behavior indicates that the enhanced penetration at low array angles is not driven by strong recirculation zones, but rather by the reduced frontal blockage presented to the crossflow. The flow is able to pass more easily around the jet array, which presents a more streamlined shape at lower angles, and reattaches rapidly downstream, thereby limiting the extent of the reverse-flow region. As discussed in the previous section, this streamlined configuration reduces momentum dissipation and allows the jets to penetrate further into the crossflow.

In contrast, the 60° configuration exhibits the most extended recirculation zone, due to a strong leading jet that penetrates deeply into the crossflow (see Fig. 4.4). As discussed in subsection 4.3.2, partial merging at intermediate angles locally reinforces the jets: for example, the 60° leading jets are strengthened, while the 45° array shows an additional lifted structure near the center. This lifting of the merged structures sustains circulation between adjacent jets, enhancing penetration and promoting significant flow blockage, which in turn generates a pronounced recirculation zone downstream, in this case starting behind the leading jet ($y < 0$) and propagating along the array as J increases.

Overall, the results show that the recirculation zone systematically grows with increasing momentum flux ratio J for all injection angles, but the array angle has a non monotonic influence on its size, with the lowest array angle inducing less recirculation. These region a particularly interesting as they can either stabilize the flame or degrading the local mixing quality.

4.5 Jet–crossflow mixing

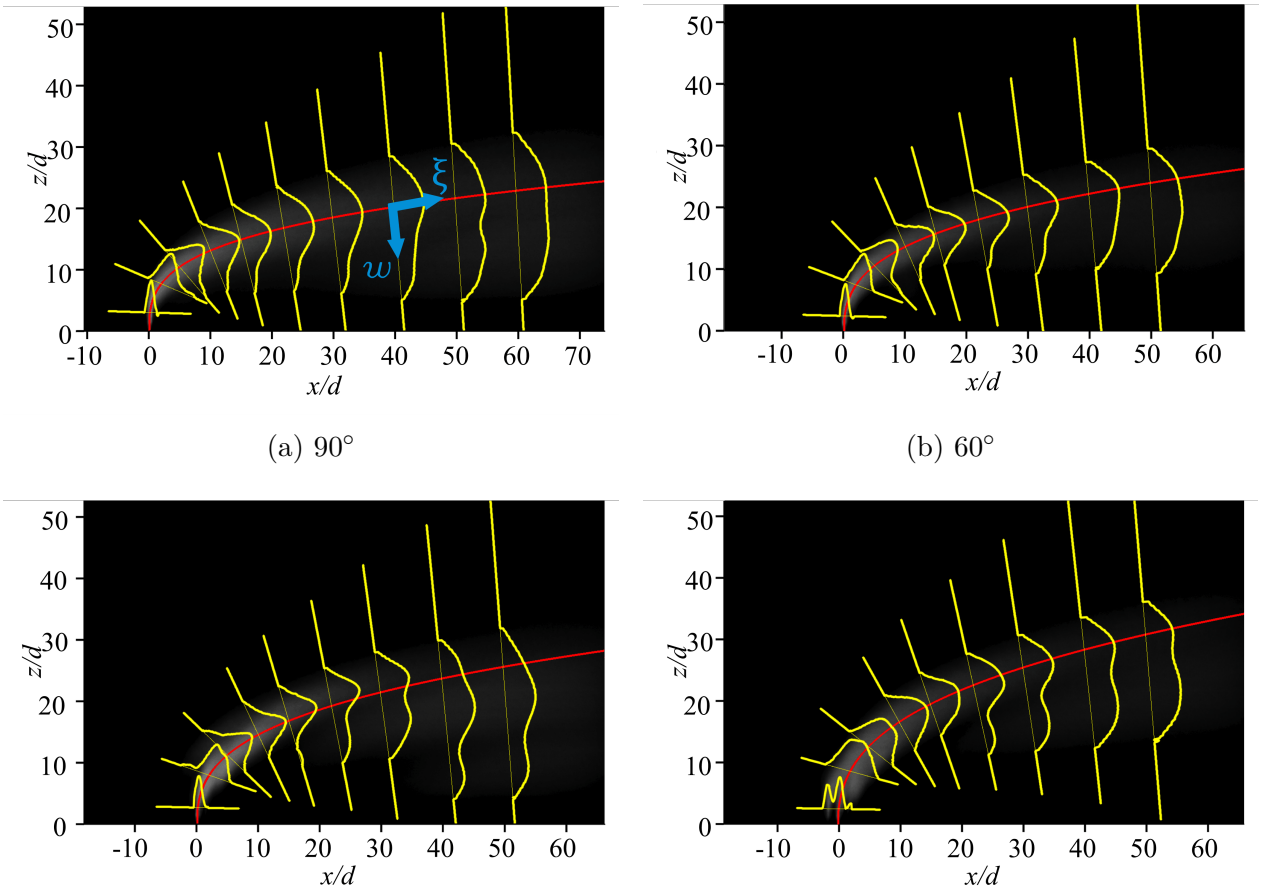
While molecular diffusion is not captured in these experiments, advective mixing is characterized using oil droplets seeded in the jets. Here, "mixing" refers to the dispersion and transport of these tracers between the jets and crossflow. The mixing field is obtained from normalized, time-averaged intensity maps in the profile view, providing droplet concentration along the jet centerlines. This allows systematic analysis of mixing evolution with array angle and momentum flux ratio J, including lateral jet spread and centerline intensity decay.

Spatial and temporal variations are also examined using the unmixedness parameter $\mathcal{U}$ (Eq. 3.12) to quantify concentration inhomogeneity. Dominant mixing dynamics are further analyzed via Proper Orthogonal Decomposition (POD), identifying energetic coherent structures and their temporal behavior, which are relevant to spatial and temporal mixing inhomogeneities observed in reacting flows.

4.5.1 Mixing field

The time-averaged profile-view intensity fields obtained on a $xz-$plane passing through the 5^{th} jet are used to characterize the mixing field for the four angled linear arrays, already shown in Fig. 4.6. Intensity distributions are extracted from these images along lines perpendicular to the jet centerline at various downstream locations, as illustrated in Fig. 4.15. Time-averaged profile views for the array angles (a) 90°, (b) 60°, (c) 45°, and (d) 30° are overlaid with normalized intensity profiles at several downstream locations, enabling direct identification of characteristic transverse mixing features and their physical origin within the intensity field. For instance, in the 30° configuration shown in Fig. 4.15 d, the near-field intensity profiles include contributions from adjacent jets, resulting in additional narrow peaks. Further downstream, the CVP induces a broader, lower-intensity peak on the leeward side ($+w/d$) of the jet, reflecting enhanced lateral spreading and entrainment of crossflow fluid.

A comparison of the transverse intensity distributions for all array angles is presented in Fig. 4.16 for the $J = 25$ case. All configurations exhibit a similar overall behavior: at the jet exit ($x/d = 0$), the intensity distribution is characterized by a narrow, high-amplitude peak with a width of approximately one jet diameter. As the downstream distance increases, this peak progressively broadens and decreases in amplitude, reflecting the gradual dilution of the JICF. Despite these common trends, marked differences are observed between array angles. For tightly angled arrays, such as 30° and 45°, additional intensity peaks appear near the jet exit as a result of interactions with closely spaced neighboring jets. These secondary peaks rapidly alter the initially narrow transverse distribution, particularly for the smallest angle configuration (30°), leading to a significantly broader profile within less than one jet diameter downstream of the exit. In the intermediate region ($1 < x/d < 14$), the transverse intensity distributions evolve toward Gaussian shapes, consistent with classical observations for a SJICF, accompanied by a reduction in peak amplitude and an increase in profile width. This behavior persists further downstream, indicating continued jet dilution within the crossflow. However, a clear distinction can be made between the regions upstream and downstream of $x/d \approx 14$. In the far field ($x/d > 14$), an additional intensity peak systematically develops on the leeward side ($+w/d$) of the jet. This feature is associated with the action of the CVP, which enhances lateral transport and increases the overall spread of the intensity distributions. A particular behavior is observed for the 45° configuration in the far field. Instead of a single broad hump induced by the CVP, the transverse profiles exhibit two successive leeward humps. Based on the cross-sectional views shown in Fig. 4.4, this behavior is attributed to the development of more complex and chaotic flow structures downstream of the jets, arising from enhanced jet–jet interactions at this intermediate injection angle.



(a) 90°

(b) 60°

(c) 45°

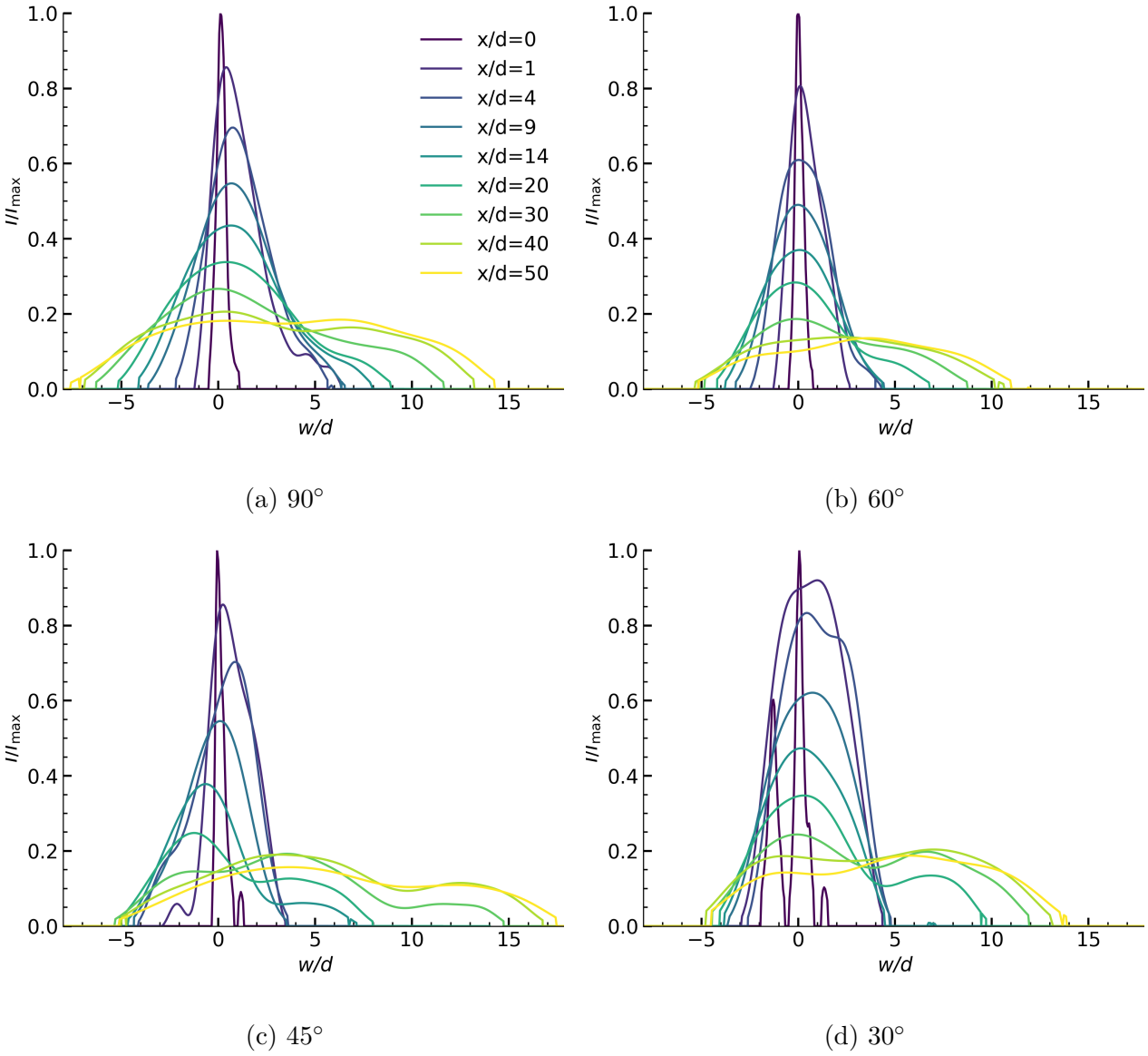
(d) 30°

Figure 4.15 Time-averaged images of the 5$^{\text{th}}$ jet exit plane at $J = 25$ for the different array angles. The jet centerline (red) and the intensity distributions measured along the normals to the centerline (yellow) are shown for $J = 25$.

Evolution of the spread

A quantitative analysis of the spread of the intensity distributions along the jet centerlines is presented in Fig. 4.17. The spread is characterized using the FWTM of the normalized intensity distributions, scaled by d. This metric is plotted in Fig. 4.11 as a function of the downstream distance x/d, with the origin aligned at the 5$^{\text{th}}$ jet exit. The figure highlights the influence of both the array angle (analyzed first) and J (analyzed subsequently) on the spread.

The array angle strongly influences the spatial evolution of the spread. As the array angle decreases, the evolution of the spread becomes increasingly step-like. The largest angle (90°) exhibits a relatively smooth and gradual increase of the spread along the downstream



(a) 90°

(b) 60°

(c) 45°

(d) 30°

Figure 4.16 Intensity distributions measured at $J = 25$ along the normals to the centerline of the 5^{th} jet for all array angles. The transverse coordinate w is centered on the jet centerline.

direction. A similar behavior is observed for the 60° array, although some perturbations appear, including a sudden increase around $x/d = 10$. For lower angles (45° and 30°), the spread evolution shows more abrupt variations occurring both in the near field and farther downstream. For instance, around $x/d = 15$, a rapid increase in spread is observed. Referring back to Fig. 4.15, this location corresponds to the emergence of the CVP. The appearance of the CVP in the image therefore increases jet dispersion in the xz-plane and enhances mixing. In general, the stronger the CVP, the larger the resulting spread.

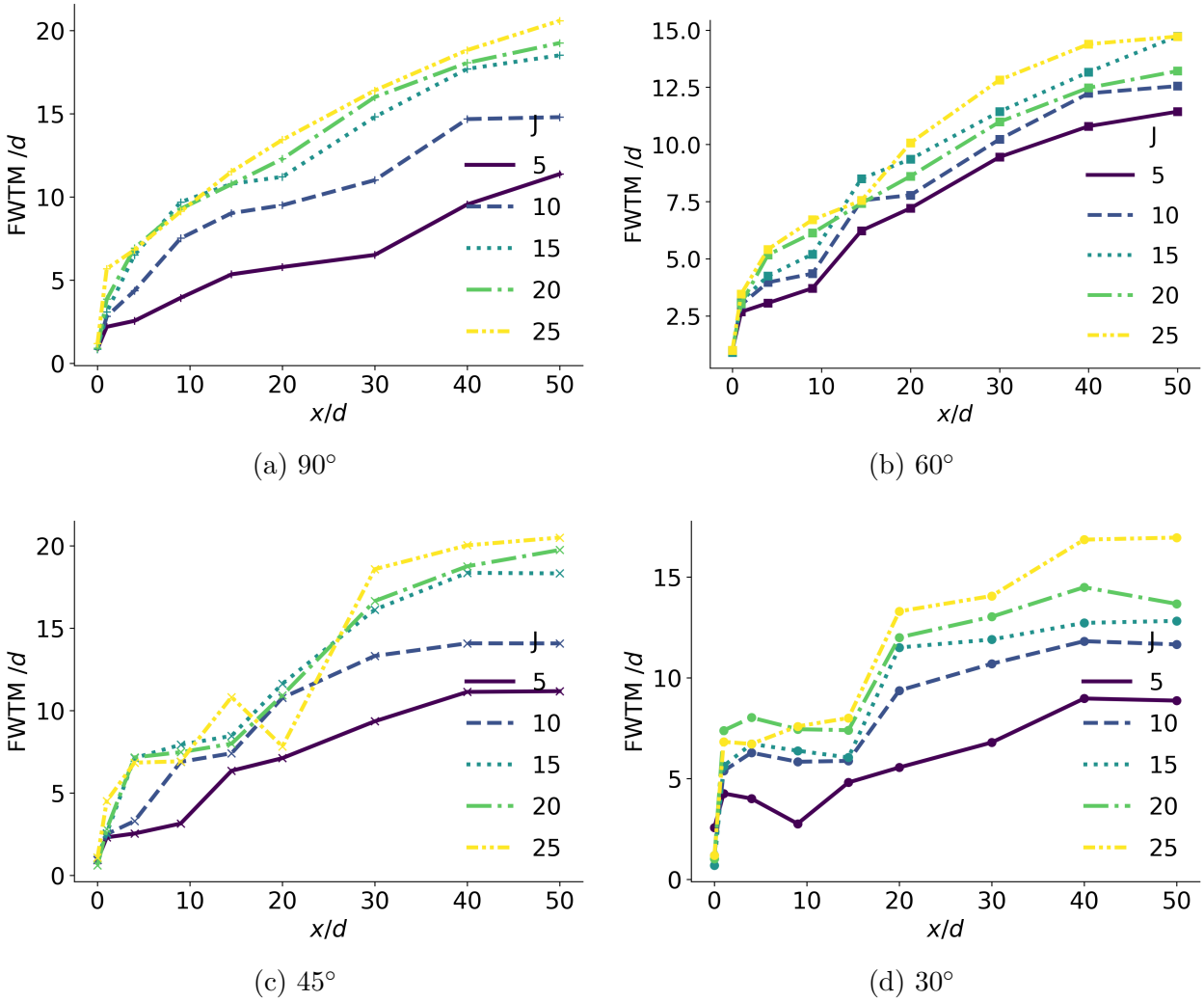
In particular, the 90° and 45° configurations exhibit larger spreads than the other two configurations by approx 30% due to stronger CVP structures. In the 90° case, the large frontal exposure of the jets promotes stronger interaction with the crossflow, leading to the formation of a more intense CVP and additional jet dispersion. In contrast, the larger spread observed for the 45° configuration primarily originates from the double broad peak structure visible in Fig. 4.16. This feature systematically produces larger spreads than the other configurations over most of the downstream distance, except in the near field ($x/d < 10$). For example, the 45° case at $J = 15$ exhibits a wider spread than the 60° case at $J = 25$.

Additionally, the near-field region is strongly influenced by the array angle. For smaller angles, the apparent initial spread at the jet exit is larger; however, this is primarily an artifact of the laser capturing multiple adjacent jets rather than true lateral mixing. Consequently, although the intensity profiles seem broader in the near field, the actual jet dispersion remains limited until the CVP forms, typically between $x/d = 15$ and 20. In this region, the observed widening of the intensity distribution reflects the superposition of neighboring jets rather than enhanced mixing or dilution. A detailed analysis of the intensity profiles is provided in the next section to support this interpretation.

Finally, a deep penetration does not necessarily correspond to a larger spread. The 30° array, which penetrates deeper into the crossflow (Fig. 4.8), exhibits a smaller vertical spread than the other configurations. This observation recalls back-to-back jet configurations, where the downstream jet also shows reduced spreading [70]. It further suggests that both jet penetration and lateral displacement in the spanwise (y) direction must be balanced to achieve efficient mixing. These findings are in agreement with the results of Holdeman [54], who demonstrated that optimal mixing occurs when a balance is achieved between jet penetration and lateral spreading, which is strongly influenced by the frontal jet spacing and, therefore, by the array angle. In the present configuration, wider array angles (e.g., 90°) promote mixing more effectively than smaller angles (e.g., 30°), despite the shielding effect present in the latter.

Concerning the effect of J on the spread, a larger jet dispersion is observed for higher values of J across all array configurations. This trend confirms that high J promotes jet dispersion and mixing, whereas lower J conditions are more suitable for film-cooling applications, where jet attachment to the surface is desired [55].

As the jet trajectory is strongly governed by R, its influence on the spread is analyzed in Fig. 4.18, where the spread is normalized by $Rd \propto \sqrt{J}\,d$. This normalization collapses the spread curves for all array angles, except for the 60° case, suggesting that the spread follows the scaling FWTM $\propto R \propto \sqrt{J}$. Regarding the 60° configuration, scaling by Rd leads to an



(a) 90°

(b) 60°

(c) 45°

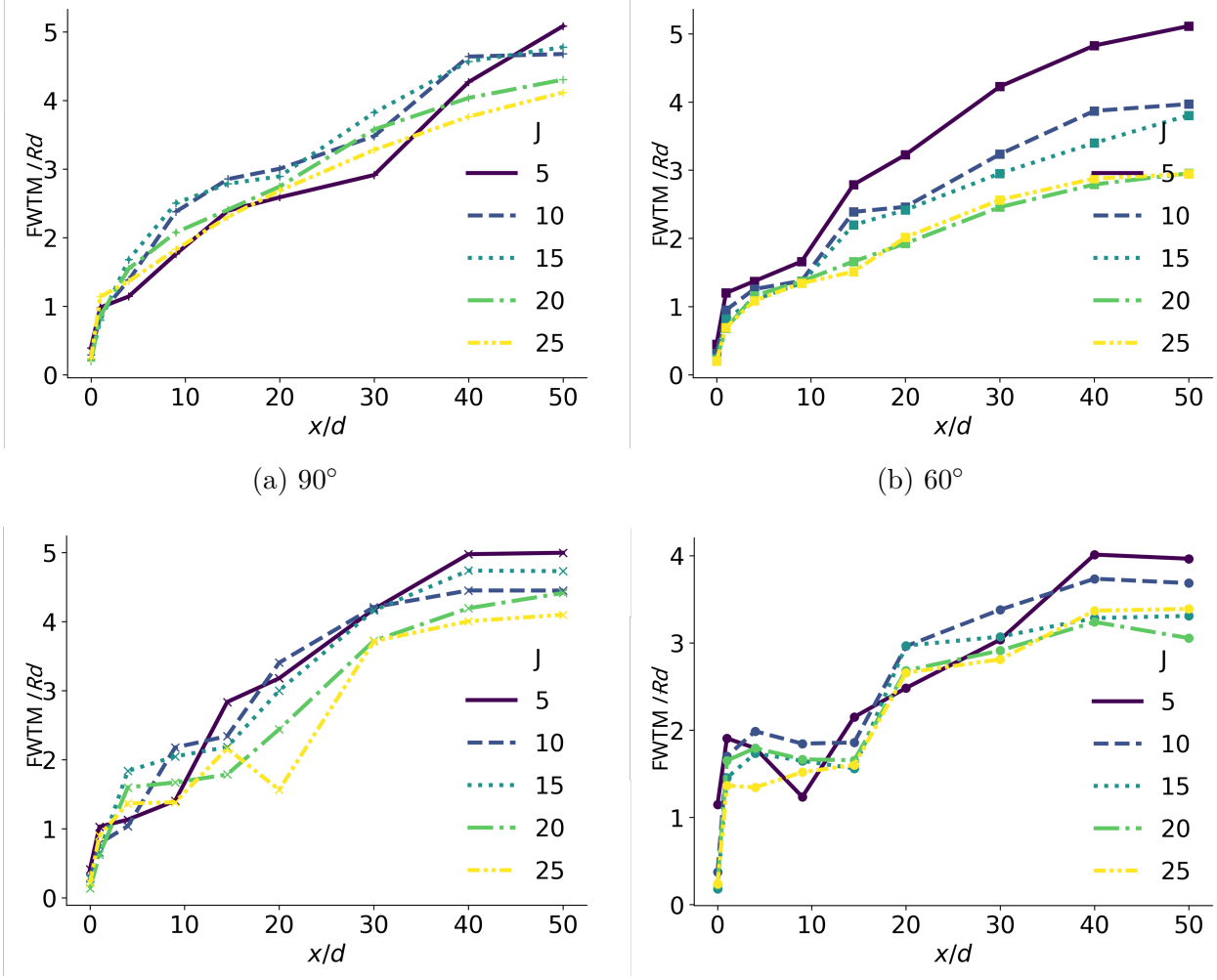
(d) 30°

Figure 4.17 Spread along the downstream distance for angles and J

inversion of the trend, with lower J cases exhibiting a larger normalized spread than higher J cases. This behavior indicates an over-normalization. A better agreement is obtained when the spread is scaled by $J^{1/3}$, for which the curves corresponding to different J values collapse.

Intensity decay along the centerline

The mixing process is analyzed through the intensity decay, complementing the previous geometrical study based on the spread analysis. The evolution of the local maximum intensity along the jet centerline is presented in Fig. 4.19. These local maxima correspond to the maximum intensity measured along the normals to the centerline to account for potential discrepancies between the fitted centerline and the actual location of peak intensity.



(a) 90°

(b) 60°

(c) 45°

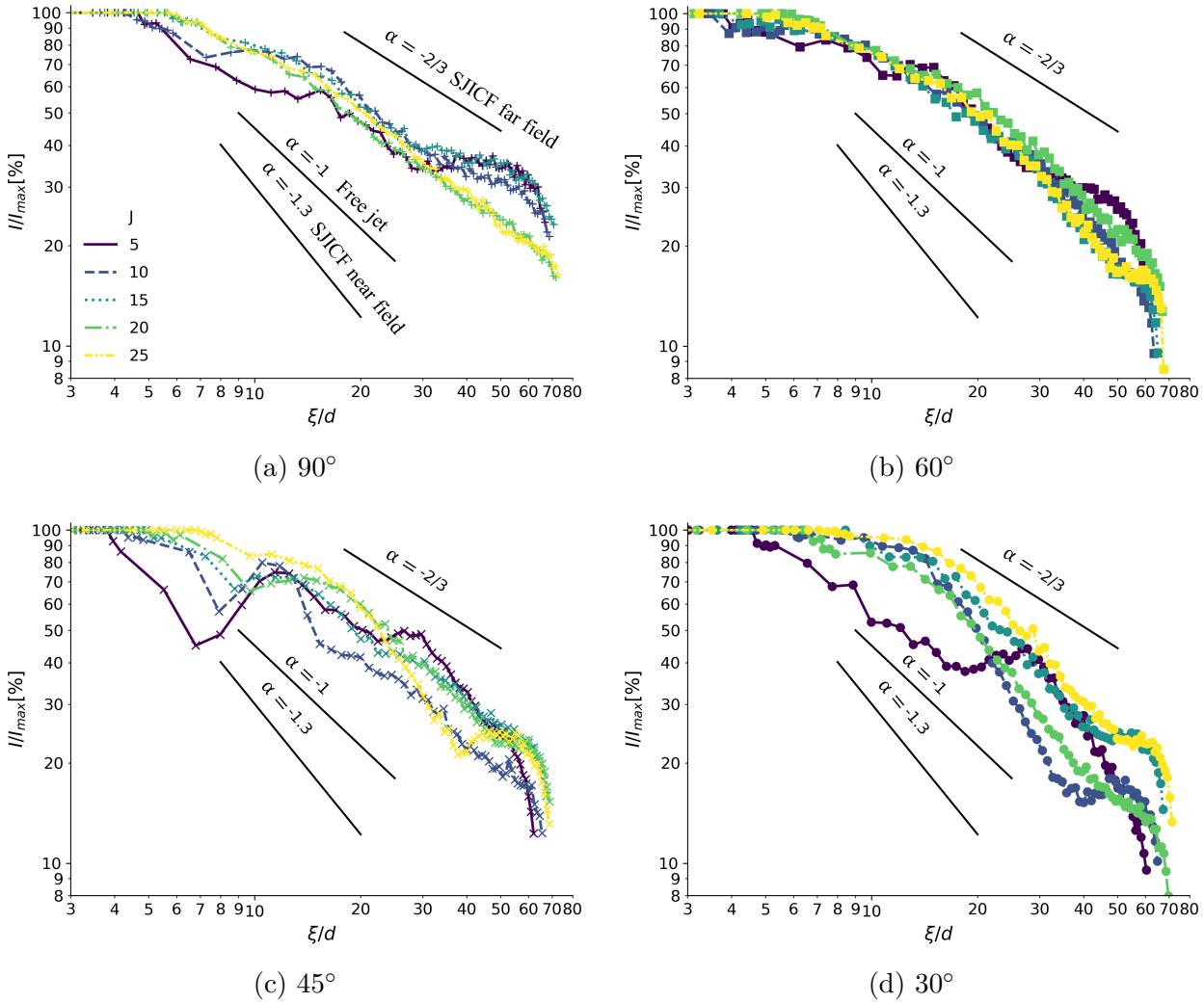
(d) 30°

Figure 4.18 $Rd-$scaled spread along the downstream distance for angles and J

The local maximum intensities I are normalized by the global maximum intensity at the jet exit, I_{max}. Their downstream evolution is expressed as a function of the centerline coordinate ξ, following the framework proposed by Smith and Mungal [50]. It has been shown that the concentration decay (i.e., the intensity decay in the present study) follows the relationship $I/I_{max} \propto (\xi/d)^{\alpha}$, where α is the decay rate. Accordingly, the figure is plotted on a logarithmic scale and includes three reference slopes ($\alpha = -1$, $\alpha = -1.3$, and $\alpha = -2/3$), corresponding respectively to the characteristic decay rates of the centerline concentration for three specific configurations: a free jet (without crossflow), the near field of a SJICF, and the far field of a SJICF [50].

The evolution of the normalized centerline intensity reveals distinct regimes that are consis-

tently observed across all configurations. These include a core region, where the intensity remains close to its maximum value near the jet exit and one or several branch points associated with abrupt changes in the decay behavior. Such transitions may correspond, for instance, to the change from the near-field decay rate ($\alpha = -1.3$) to the far-field decay rate ($\alpha = -2/3$) reported for SJICF [50]. The influence of the array angle and the momentum flux ratio J primarily manifests through modifications of the extent of these regions and through shifts in the locations of the transitions between them.



(a) 90° (b) 60°

(c) 45° (d) 30°

Figure 4.19 Evolution of the normalized maximal intensity per branch along the centerline coordinate ξ

First, the jet core is defined as the region where the normalized centerline intensity remains approximately equal to the jet exit intensity ($I/I_{max} \approx 100\%$), reflecting the initial jet strength. As shown in Fig. 4.19, all array angles exhibit a jet core. To quantify the effect

of J and the array angle on the jet core, its length L is introduced, corresponding to the distance from the jet exit to the centerline coordinate where the intensity begins to decay ($I/I_{max} < 99\%$). Typically, L varies from $L/d \approx 4$ to 9. The potential core length increases with J for all array angles, as higher jet momentum delays the onset of mixing within the jet core. For instance, in the 90° configuration, L increases from $4.3d$ at $J = 5$ to $5.7d$ at $J = 25$. In the 45° case, L evolves as $L_{J=5}/d = 3.8$, $L_{J=10}/d = 4.2$, $L_{J=15}/d = 5.0$, $L_{J=20}/d = 4.9$, and $L_{J=25}/d = 6.8$. This trend confirms that higher J values strengthen the jet momentum and delay mixing, thereby extending the potential core. Although L generally increases with J, this evolution is not strictly monotonic. Instead, the data tend to cluster into groups, with low J cases generally exhibiting shorter potential cores than high J cases, while still supporting the overall trend of increasing L with J.

The potential core length also depends on the array angle, with lower angles exhibiting longer cores. For instance, at $J = 25$, the potential core lengths are $L_{90°}/d = 5.7$, $L_{60°}/d = 5.3$, $L_{45°}/d = 6.8$, and $L_{30°}/d = 7.9$, indicating that the potential core length increases as the array angle decreases. A similar trend is observed for other values of J, although with smaller differences. Smaller array angles lead combined jet intensity, extend the potential core and reduced near-field mixing. This confirms that, although the spread may be wider for low angles, the high centerline intensity demonstrates that this region remains largely unmixed.

Second, once the intensity decay starts, after the potential core, the rate of decay can be described by a power law such as $I/I_{max} = \xi/d^{\alpha}$ [50]. Significant change in the decay rate (α) occur at branch points. They indicate transitions between different dominant mixing mechanisms and reflect the influence of jet-to-jet interactions as well as the formation, strengthening, or reorganization of the CVP. For example, in the 90° array, low J cases exhibit branch points at $\xi/d \approx 7$, 18, and 30, while higher J values show fewer or no branch points, indicating a smoother decay as the jets mix more uniformly with the crossflow. This trend is reflected in the smooth spread evolution observed at $J = 25$ (Fig. 4.17).

The array angle primarily affects the local decay rate α. Wider angles (90° and 60°) exhibit slower decay rates. For the 90° configuration, α ranges from approximately -0.6 in the near field to about -1.0 in the far field. Similarly, the 60° configuration shows a non-constant decay rate, $\alpha = \alpha(\xi)$, evolving from $\alpha \approx -0.6$ in the near field to $\alpha \approx -1.3$ in the far field. In contrast, smaller angles (30° and 45°) exhibit stronger local decay rates, with α reaching values as low as -1.8 for the 30° array. These smaller array angles, therefore, promote faster dilution of the jet. This observation is consistent with the 3D reconstruction of the flow (Fig. 4.5), where the 30° configuration exhibits more rapid mixing compared to the other angles.

While J does not significantly affect the decay rate α, it strongly influences the location of the bifurcations in the intensity decay. The latter occur where the CVP legs merge with the leeward side of the jets. Although the CVP broadens the jet and promotes lateral dilution, the intensity transported by the CVP into the main body of the jet can delay the decay of the centerline intensity, producing plateaus in the decay evolution. For example, in the 90° configuration at low J, a CVP-induced plateau occurs at $\xi/d \approx 30$, delaying the intensity decay by an additional $\Delta\xi/d \approx 30$. As J increases, the location of this plateau shifts downstream or eventually disappears. For instance, in the 90° case the plateau moves from $\xi/d \approx 30$ at $J = 5$ to no observable plateau at $J = 25$. Similarly, the plateau location shifts from $\xi/d \approx 33$ at $J = 5$ to $\xi/d \approx 50$ ($J = 25$) for the 60° configuration, from $\xi/d \approx 21$ to $\xi/d \approx 38$ for 45°, and from $\xi/d \approx 15$ to $\xi/d \approx 50$ for 30° as J increases. These locations correspond to the appearance of the CVP in the 5^{th} jet measurement plane, as illustrated in the averaged jet images (Fig. 4.6) and by the hump observed on the leeward side in the intensity distributions (Fig. 4.16). Overall, the CVP-induced plateaus shift downstream as J increases and delays the intensity decay by $\Delta\xi/d \approx 10$–20, and up to about 30 depending on the case, without a clear dependence of the plateau width on either the array angle or J.

Additionally, the 45° array exhibits the largest number of branch points, resulting not only from the formation of the CVP but also from strong jet–jet interactions. In the near field, an sudden decay of intensity appears around $\xi/d \approx 7$ for low J, shifting to $\xi/d \approx 10$ for $J = 25$. This phenomena results from a strong lateral deviation of the jets, as illustrated by the instantaneous cross-sectional views in Fig. 4.4. At 45°, the jet trajectories are strongly three-dimensional due to the combined effects of neighboring jets and the crossflow. As a result, some jets temporarily deviate away from the measurement plane, leading to a local reduction of the measured centerline intensity (see section 4.3.2). Downstream, a local peak appears at $\xi/d \approx 11$, corresponding to the reappearance of neighboring jets intersecting the measurement plane with higher intensity. This complex three-dimensional jet motion explains the multiple branch points observed in the intensity decay for the 45° configuration.

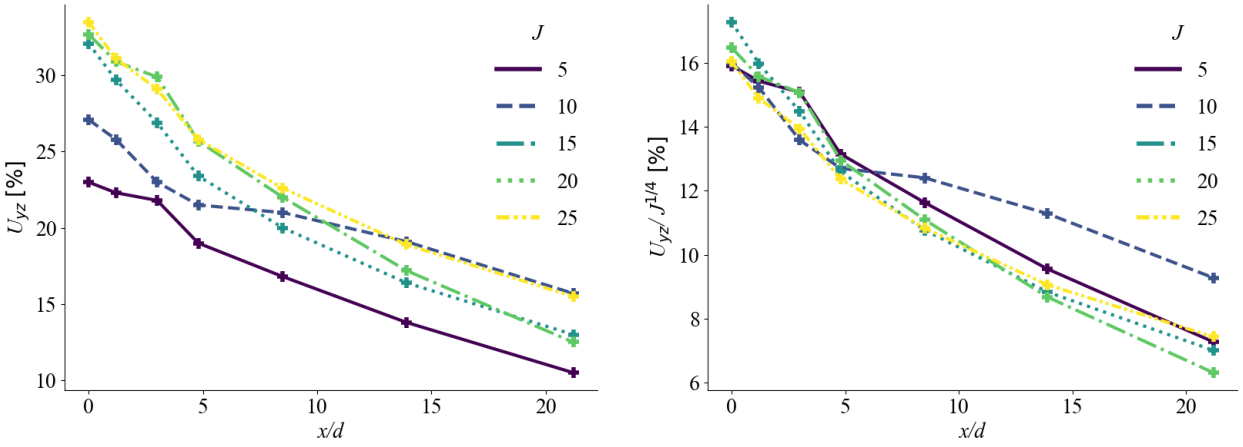
Finally, The array angles reach different normalized intensity levels at the end of the decay, i.e., after the plateau region. The final intensity ranges are $I/I_{max} = 22\% - 16\%$ for 90°, $15\% - 9\%$ for 60°, $15\% - 12\%$ for 45°, and $14\% - 8\%$ for 30°. Overall, a clear trend is observed: as the array angle decreases, the final normalized intensity at the end of the fixed observation window of length $70d$ also decreases. This indicates that smaller angles promote stronger dilution in the far field.

4.5.2 Mixing Variation

The analysis of time-averaged intensity distributions along the jet centerline, including intensity decay and jet spread, reveals that local mixing, a highly time-dependent process, can significantly deviate from the maximum intensity profile. These variations between the ambient air and the seeded jets are quantified both spatially and temporally.

Spatial Mixing

Poor local mixing leads to the formation of fuel-rich or fuel-lean pockets, whereas homogeneous mixing results in smoother concentration gradients and improved combustion stability. Spatial variations in mixing are quantified using the unmixedness parameter $\mathcal{U}_{yz}$ (Eq. 3.12) computed from instantaneous front-view images ($yz-$planes), allowing the evolution of the mixing degree to be characterized. Figure 4.20 presents the spatial evolution of the time-averaged $\mathcal{U}_{yz}$ at various downstream cross-sections for (a) the 90° configuration at different momentum flux ratios J, and (b) different array angles. The averaging is performed over 1 s at a sampling frequency of 1 kHz. Overall, the unmixedness decreases with downstream distance, consistent with the intensity measurements presented above and with observations reported in the literature [110]. The decay curves of unmixedness are generally ordered ac-



(a) Unscaled evolution of $\mathcal{U}_{yz}$ for all J

(b) Scaled evolution of $\mathcal{U}_{yz}$ using $J^{1/4}$

Figure 4.20 Spatial evolution of the time-averaged unmixedness parameter $\mathcal{U}_{yz}$ computed over cross-sections in the yz-plane for the 90° array configuration : (a) Raw (unscaled) values of $\mathcal{U}_{yz}$ for all momentum ratios J; (b) Collapse of the data obtained by scaling $\mathcal{U}_{yz}$ with the best-fit factor $J^{1/4}$

cording to J, with lower unmixedness observed for smaller J. This indicates that higher J

values correspond to increased local inhomogeneity. This trend is consistent with previous observations: higher J produces a longer potential core, leading to stronger spatial intensity gradients, whereas the intensity decay begins earlier at low J, promoting earlier mixing and more uniform distribution.

Additionally, when the unmixedness decay is scaled by $J^{1/4}$, the curves corresponding to different momentum ratios collapse onto a more consistent trend for all J in the 90° configuration. This collapse indicates that the cross-sectional unmixedness follows approximately $\mathcal{U}_{yz} \propto J^{1/4}$.

In Fig. 4.21, the mixing quality for each linear array is evaluated from the 5$^{\text{th}}$ jet exit to several downstream positions, with the origin set at the 8$^{\text{th}}$ jet exit, to refer downstream measurements to a common origin. The results show that unmixedness generally increases with J for all array angles, with the notable exception of the 60° configuration. For this case, higher J actually produces a smoother spatial mixing distribution. This behavior may be related to the interplay between jet penetration and lateral spreading: at higher J, the jets penetrate further but also spread more uniformly, reducing local intensity gradients and the measured unmixedness. Yet, the physical origin of this observation is not fully understood.

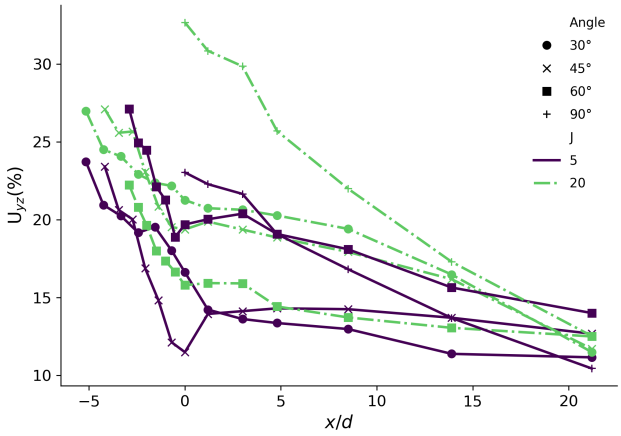


Figure 4.21 Spatial evolution of the time-average unmixedness parameter, $\mathcal{U}_{yz}$, calculated over cross sections (yz-plane) for all array angles at $J = 5$ and 20

Array angle also strongly affects unmixedness. Excluding the 60° case at $J = 20$, smaller angles (30° and 45°) exhibit lower unmixedness, indicating better spatial mixing. This is likely due to the closer spacing of neighboring jets, which promotes early jet–jet interactions and more rapid homogenization of the flow in the near field. The penetration also plays a role with higher depth reached by low array angles and therefore a wider spatial distribution.

Moreover, for array angles smaller than 90°, the unmixedness exhibits two distinct regimes: a

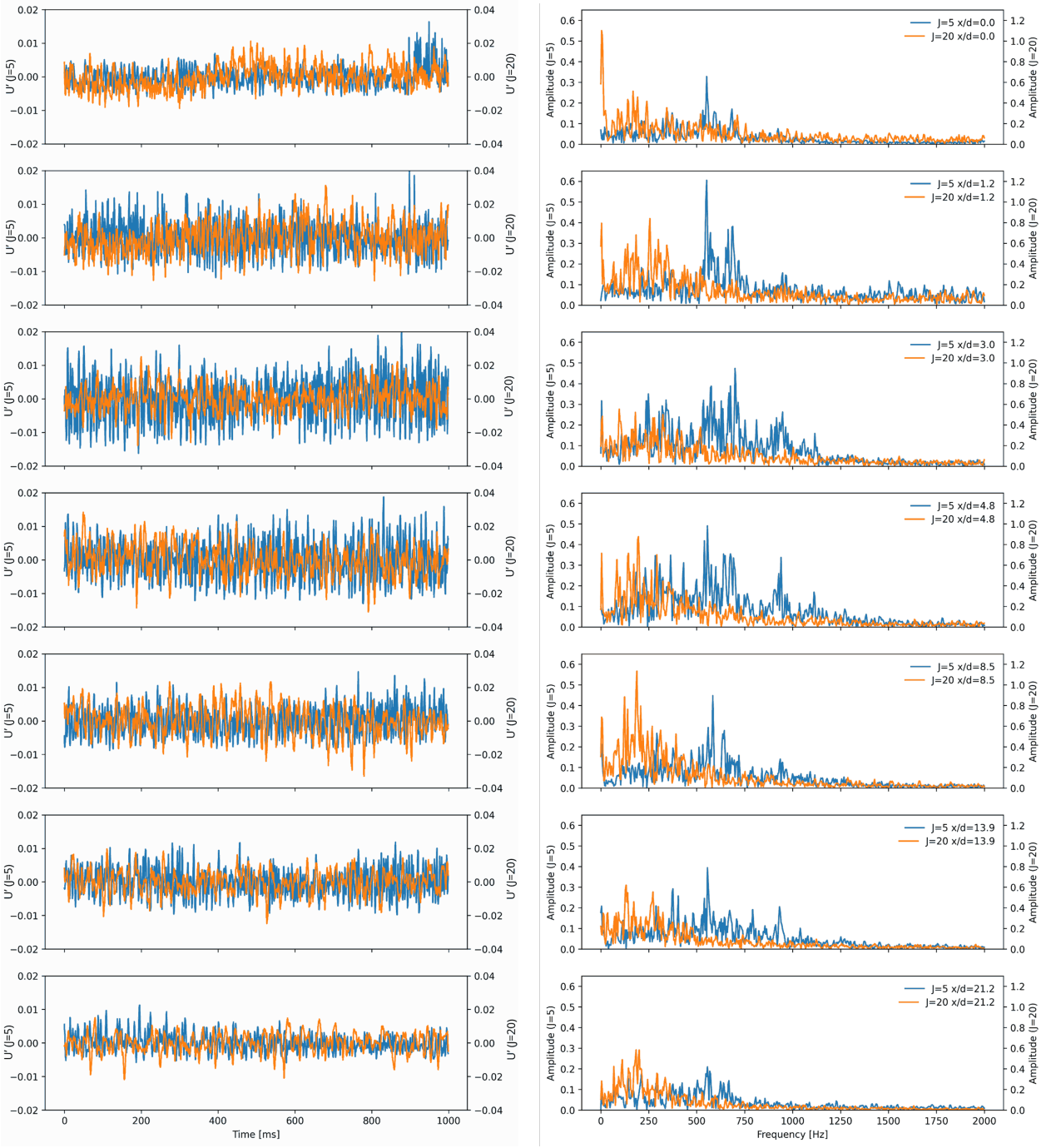
rapid decrease within the array itself ($x/d < 0$) and a more gradual decay downstream of the last jet exit ($x/d > 0$). This distinction arises from the location relative to the array. Within the array, newly injected jets temporarily increase the unmixedness. However, in angled arrays, preceding jets have sufficient time to mix before subsequent jets are introduced, leading to a net reduction of U in the far field. The rapid decrease within the array is caused by the addition of new jets, which locally increase unmixedness but simultaneously generate a broader lateral spread a short distance downstream. Further downstream, outside the array, the unmixedness decreases more slowly as the flow continues to mix and homogenize.

Temporal Variations

Temporal variations are particularly critical in reacting flows, as intermittent peaks in species concentration can locally influence chemical processes, such as NO_x formation. To analyze the temporal evolution of mixing, a spectral analysis was performed on the unmixedness parameter using a 4 kHz acquisition frequency. Figure 4.22 shows (a) the temporal variations of the unmixedness parameter $\mathcal{U}'_{yz}(t) = \mathcal{U}_{yz}(t) - \langle \mathcal{U}_{yz} \rangle_t$ and (b) the corresponding frequency spectrum (via FFT) of these fluctuations for the 90° angled configuration at momentum ratios $J = 5$ and 20, evaluated at various downstream positions (x/d).

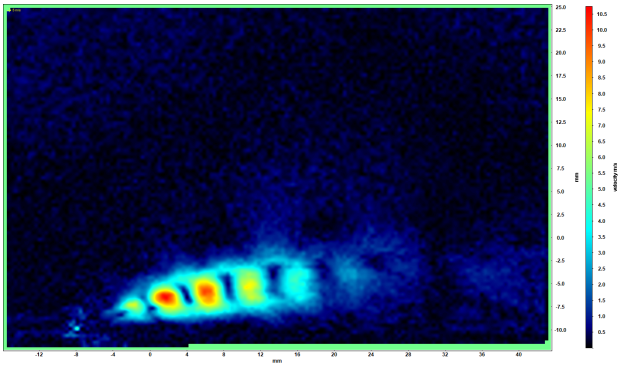
The temporal evolution reveals fluctuations around the mean value, with characteristic frequencies identified in the spectrum. For $J = 5$, the spectrum systematically exhibits peaks near 530 Hz, corresponding to a Strouhal number of $St = fd/U_\infty = 0.3$ based on the crossflow velocity. This value is consistent with shear layer instabilities typically observed in jets in crossflow [65]. Additional prominent frequencies for $J = 5$ include $f \approx 680$ Hz and 910 Hz, associated with rapid variations in the unmixedness parameter. In the intermediate field ($x/d = 3$ to 8.5), peaks are observed between 270 Hz and 310 Hz, shifting to lower frequencies (80–100 Hz) in the far field ($x/d > 13.9$). In contrast, the $J = 25$ case exhibits low-frequency instabilities with amplitudes approximately twice those of the $J = 5$ case. The dominant frequency across the entire domain is 240 Hz, with additional peaks at lower frequencies, notably $f = 80$ Hz and 130 Hz in the far field.

To relate the characteristic frequencies of the unmixedness parameter to the dominant flow modes, a Proper Orthogonal Decomposition (POD) analysis is employed. POD establishes a correspondence between the temporal evolution of spatial modes and the main flow structures. When applied to the profile view in Fig. 4.23, the POD reveals the spatial modes associated with the most energetic structures, ranked in descending order. Although the ordering of modes is sensitive to experimental design, the frequencies linked to these spatial modes can be extracted and associated with specific jet-crossflow interactions.

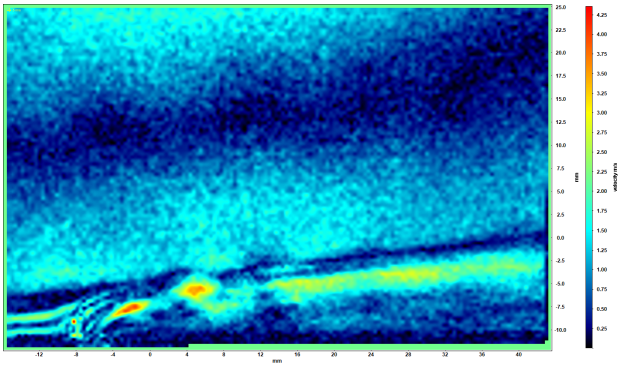


(a) Temporal fluctuations $\mathcal{U}'_{yz}(t)$ (b) Spectrum of $\mathcal{U}'_{yz}(t)$

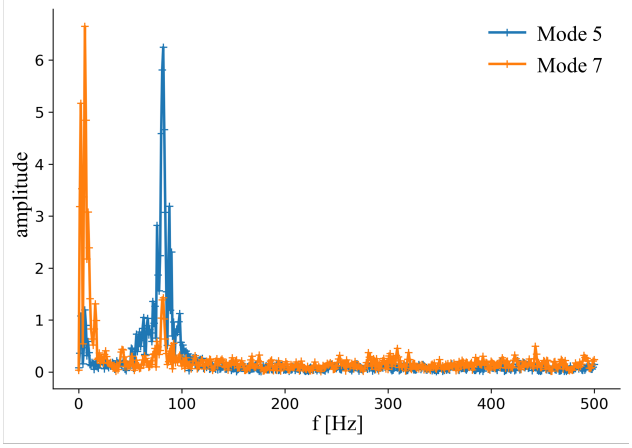
Figure 4.22 Temporal fluctuations and the associated spectrum of the unmixedness parameter evaluated at various downstream positions for the 90° configuration and for $J = 5$ and 20



(a) 5^{th} energetic mode



(b) 7^{th} energetic mode



(c) Spectrum of the KH instabilities mode (5) and the CVP mode (7)

Figure 4.23 POD spatial modes with their associated spectrum for the 90° array at $J = 5$ from a profile view

For example, Fig. 4.23 presents the two dominant modes measured at $J = 5$ for the 90° configuration: (a) 5^{th} energetic mode and (b) 7^{th} energetic mode, along with (c) their corresponding spectrum. The spectra highlight two main frequencies: a low frequency of $f \approx 85$ Hz for mode 5, and $f \approx 7$ Hz for mode 7. Spatial mode 5 corresponds to KH instabilities, while mode 7 is associated with the leeward side of the mean flow path, where the far-field structure corresponds to the CVP. Thus, KH instabilities manifest as periodic structures at 85 Hz, whereas the CVP exhibits nearly steady behavior over time, comparing to higher frequencies involved in the flow.

Consequently, the temporal variations of the unmixedness parameter align with the frequencies of KH instabilities, corresponding to the large vortex structures shown in Fig. 4.4. This leads to the formation of alternating rich and poor mixing pockets. Similarly, other mixing

frequencies can be linked to spatial jet-crossflow interactions, such as KH instabilities predominant in the near field and vibrating at 530 Hz. Generally, shear layer instabilities are associated with high-frequency mixing (680 Hz and 910 Hz), while low frequencies are linked to large-scale structures. The analysis of these frequencies provides insight into the temporal evolution of the mixing degree.

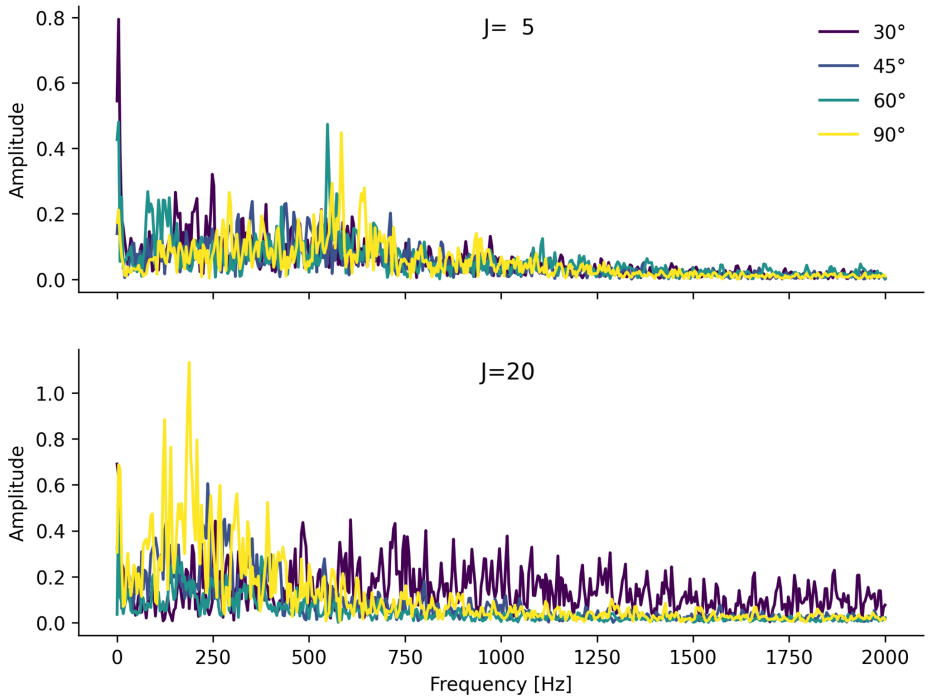


Figure 4.24 Spectrum of the unmixedmess parameter evaluated on the cross section $x/d = 8.5$ for $J = 5$ and 20 across all configurations

Figure 4.24 shows the spectrum of the unmixedness parameter at $x/d = 8.5$ downstream of the 5^{th} jet exit for all injection configurations for $J = 5$ and $J = 20$. Large array angles (90° and 60°) exhibit distinct peaks around 530 Hz, corresponding to KH instabilities on the windward side of the jet. In contrast, lower array angles (30° and 45°) do not display clearly dominant frequencies, although the 45° case shows a slight amplitude increase in the $[250, 500]$ Hz band and the 30° case in the $[140, 250]$ Hz band. These observations are consistent with the influence of tightly spaced jets in JICF: close frontal spacing (s_y) promotes the interaction of shear-layer vortices and suppresses globally unstable modes, thereby enhancing mixing [21].

Reducing the momentum flux ratio J leads to a noisier spectrum, with no distinct frequencies observed for the 30° configuration. This behavior suggests a complete breakdown of coherent structures, implying that mixing occurs predominantly at small turbulent scales, with a

more temporally homogeneous distribution, thereby preventing the formation of alternating mixed and unmixed regions. For higher array angles, low-frequency components become more prominent, particularly for the 90° configuration, which exhibits a strong response at $f \approx 200$ Hz. The 45° and 60° configurations follow in terms of amplitude.

Overall, these observations indicate that both the momentum flux ratio and the array angle strongly influence the temporal coherence of the flow, with lower J and smaller angles promoting rapid, small-scale mixing, while higher angles sustain larger-scale, low-frequency structures.

CHAPTER 5 CONCLUSION

5.1 Summary

Rising energy demand and pollution call for greener electricity production solutions, such as hydrogen gradually replacing natural gas in gas turbines. However, challenges such as flashback would benefit from increased use of diffusion flames in combustors, reducing mixing quality and thus an increased potential for pollutant formation. Although fundamental research has explored the JICF, it remains limited to simple jet arrangements (side-by-side and back-to-back configurations), mostly numerical only, and not using low density gas and sub-millimeter jets.

This study investigated the influence of the jet-to-crossflow momentum ratio J and the array angle on the flow structure; the velocity field; the jet penetration and spreading; and mixing characteristics of jet arrays in crossflow. The results highlight the strong coupling between geometric configuration and momentum ratio in controlling the development of coherent structures, jet trajectories, and ultimately the mixing performance.

First, the global flow structure is strongly affected by both the momentum flux ratio J and the array angle. Increasing J enhances jet penetration and progressively shifts the dominant mechanism from cooling-type attached jet behavior at low J toward strong jet–crossflow mixing at high J. At low array angles, the flow becomes highly asymmetric, with a stronger CVP developing on the leading-jet side. The proximity of the jets promotes strong jet–jet interactions that rapidly break them down and generate complex three-dimensional trajectories. These interactions modify the coherent structures developing in the shear layer. At high J, the coherent structures progressively break down and are replaced by smaller-scale turbulence.

Jet penetration is primarily controlled by J and follows the expected Rd scaling. However, the array angle introduces a shielding effect. Lower array angles promote higher penetration because the jet array forms a reduced frontal obstacle to the crossflow. Velocity field measurements show that the crossflow is therefore less deflected at the jet exits. In contrast, larger array angles create stronger crossflow deviation and higher local pressure near the jets. The resulting crossflow deviation partially shields downstream jets in low array angles, similarly to the shielding mechanism observed in back-to-back configurations. However, unlike those configurations, the recirculation zone behind the jets does not appear to significantly influence jet penetration. Larger array angles generate wider recirculation zones, whereas

the smaller frontal spacing at low angles allows the crossflow to pass around the jets and reattach rapidly downstream.

Mixing is first evaluated through the vertical spreading of the jets. The CVP plays a dominant role in far-field spreading, particularly at low array angles where the spreading evolves in a stepwise manner due to the interaction between the CVP and the jet trajectories within the array plane. In contrast, larger array angles produce a smoother spreading evolution. Increasing J systematically increases the spreading proportionally to R.

The analysis of intensity decay provides insight into the mixing rate. Low array angles combined with high J maintain a strong potential core that delays mixing in the near field. However, these configurations also exhibit higher decay rates farther downstream, ultimately producing lower scalar intensity levels and therefore stronger mixing in the far field compared with the 90° case. The CVP also generates a plateau in the decay curve, delaying mixing further downstream as J increases.

Finally, the variability of the mixing is further analyzed in both space and time. Increasing J tends to reduce spatial mixing quality, as indicated by higher unmixedness levels following approximately $\mathcal{U} \propto J^{1/4}$. Low array angles promote earlier mixing due to strong jet–jet interactions and rapid breakdown of large structures, together with earlier formation of the CVP. However, farther downstream, larger array angles achieve comparable spatial mixing quality because their stronger lateral spreading enhances scalar homogenization across the flow. The temporal mixing characteristics reveal that increasing J enhances turbulence and breaks down large-scale coherent structures, producing a broader and noisier frequency spectrum. Large array angles favor periodic shear-layer instabilities that induce oscillations in unmixedness and degrade temporal mixing quality. In contrast, the closer frontal spacing between jets at low array angles promotes earlier jet–jet interactions that disrupt these coherent structures, leading to more stable temporal mixing behavior.

5.2 Design rules for enhanced mixing

Based on the combined analysis of flow dynamics, spreading, and mixing metrics, several design guidelines can be proposed for optimizing jet-array configurations in crossflow:

- **Use moderate momentum ratios.** While increasing J enhances jet penetration and turbulence levels, excessively large J reduces spatial mixing efficiency by increasing unmixedness and delaying scalar homogenization.
- **Promote jet–jet interactions.** Reducing the array angle promotes earlier jet–jet

interactions, accelerating the breakdown of coherent structures and improving temporal mixing stability, while also enhancing dilution in the far field.

- **Leverage CVP-driven spreading.** Configurations that maintain sufficiently strong CVP, such as 45° or 90° arrays, enhance lateral transport and improve spatial homogenization while maintaining stable temporal behavior. In addition, larger array angles are less sensitive to flame anchoring effects because the spreading develops more gradually compared with the stepwise spreading observed at lower array angles.
- **Control recirculation zones.** Large recirculation regions at high J can help stabilize the flow and support flame anchoring, but they also delay mixing in the near field. Adjusting the array angle and jet spacing allows control of the size of these recirculation zones with lower recirculation area for lower array angles.

Overall, the results demonstrate that optimal mixing performance emerges from a balance between jet momentum, and vortex dynamics, highlighting the importance of combined aerodynamic and geometric design in jet-in-crossflow systems.

5.3 Future Research

To further improve the assessment of fuel-air mixing quality and better meet industrial requirements, several extensions of the present study can be considered:

- **Continuous annular array:** The finite number of jets (8) introduces significant boundary effects on the jet–crossflow dynamics. Studying larger configurations, such as annular jet arrays, would help bridge the gap between fundamental studies and practical applications. Such configurations would also enable further analysis of the relationship between angled linear arrays in straight crossflow and swirling flow systems.
- **Reactive flow conditions:** Extending the study from helium to hydrogen injection, and from non-reactive to reactive flows, would enable the investigation of flame behavior. In particular, this would allow the analysis of the influence of recirculation zones on flame anchoring, as well as the impact of mixing variability on combustion stability and pollutant emissions.
- **High-pressure conditions:** Performing experiments at elevated pressures representative of industrial burners would improve the relevance of the results. High-pressure conditions are known to affect pollutant formation mechanisms and should therefore be considered in future work.

- **Laser Induced Fluorescence (LIF) measurements:** Mixing has been investigated only through its advective component. In regions of low turbulence, however, diffusion becomes dominant and can be quantified using LIF measurements.

REFERENCES

[1] Energy Institute, "Statistical review of world energy 2025," *Energy Institute*, 2025.

[2] M. Crippa *et al.*, "GHG emissions of all world countries," Publications Office of the European Union, Luxembourg, JRC138862, 2024.

[3] World Meteorological Organization, "WMO greenhouse gas bulletin 2024," World Meteorological Organization, Tech. Rep., 2024.

[4] World Bank, "The global health cost of ambient pm2.5 air pollution," World Bank, Tech. Rep., 2020, license: CC BY 3.0 IGO.

[5] K. Rennert *et al.*, "Comprehensive evidence implies a higher social cost of CO_2," *Nature*, vol. 610, no. 7933, pp. 687–692, 2022.

[6] National Center for Environmental Economics, Office of Policy, Climate Change Division, Office of Air and Radiation, "Report on the social cost of greenhouse gases: Estimates incorporating recent scientific advances," U.S. Environmental Protection Agency, Washington, DC, Tech. Rep., 2023, ePA 430-R-23-004.

[7] Environment and Climate Change Canada, "Social cost of greenhouse gas estimates – interim updated guidance for the government of canada," 2022.

[8] International Energy Agency (IEA), "Global energy review 2025," *IEA*, 2025.

[9] United Nations Economic Commission for Europe (UNECE), "1999 protocol to abate acidification, eutrophication and ground-level ozone to the convention on long-range transboundary air pollution, as amended on 4 may 2012," *UNECE*, 2012.

[10] J. Incer-Valverde *et al.*, ""colors" of hydrogen: Definitions and carbon intensity," *Energy Conversion and Management*, vol. 291, p. 117294, 2023.

[11] IEA, "Global hydrogen review 2022," IEA, Tech. Rep., 2022.

[12] Y. Liu *et al.*, "Review of modern low emissions combustion technologies for aero gas turbine engines," *Progress in Aerospace Sciences*, vol. 94, pp. 12–45, 2017.

[13] Z. labidine Messaoudani *et al.*, "Hazards, safety and knowledge gaps on hydrogen transmission via natural gas grid: A critical review," *International Journal of Hydrogen Energy*, vol. 41, no. 39, pp. 17 511–17 525, 2016.

[14] P. J. Linstrom, "NIST Chemistry WebBook," NIST Office of Data and Informatics, 2021, nIST Standard Reference Database Number 69.

[15] M. R. Usman, "Hydrogen storage methods: Review and current status," *Renewable and Sustainable Energy Reviews*, vol. 167, p. 112743, 2022.

[16] Organisation for Economic Co-operation and Development, *Risk-based Regulatory Design for the Safe Use of Hydrogen*. Paris: OECD Publishing, 2023.

[17] H. H.-W. Funke *et al.*, "Numerical and experimental characterization of low nox micromix combustion principle for industrial hydrogen gas turbine applications," in *Proceedings of the ASME 2012 Turbo Expo: Power for Land, Sea, and Air*, vol. Volume 2: Combustion, Fuels and Emissions, Parts A and B, 06 2012, pp. 1069–1079.

[18] Z. Shi *et al.*, "Burner, combustion characteristic and flame stabilization mechanism in micromix combustion: A review," *Renewable and Sustainable Energy Reviews*, vol. 225, p. 116164, 2026.

[19] A. Abdelhafez *et al.*, "Effects of jet diameter and spacing in a micromixer-like burner for clean oxy-fuel combustion in gas turbines," *Energy*, vol. 228, p. 120561, 2021.

[20] H. H.-W. Funke *et al.*, "Experimental characterization of low NO_x micromix prototype combustors for industrial gas turbine applications," in *Proceedings of the ASME 2011 Turbo Expo: Turbine Technical Conference and Exposition*, vol. Volume 2: Combustion, Fuels and Emissions, Parts A and B, 2011, pp. 343–353.

[21] G. Dodier, "Experimental study of low density micro jets in crossflow for hydrogen injection in gas turbines," Master's thesis, Polytechnique Montréal, Montréal, Canada, 2024.

[22] D. Valero and D. B. Bung, "Sensitivity of turbulent Schmidt number and turbulence model to simulations of jets in crossflow," *Environmental Modelling & Software*, vol. 82, pp. 218–228, 2016.

[23] G. He, Y. Guo, and A. T. Hsu, "The effect of Schmidt number on turbulent scalar mixing in a jet-in-crossflow," *International Journal of Heat and Mass Transfer*, vol. 42, no. 20, pp. 3727–3738, 1999.

[24] C. M. Spadaccini, J. Peck, and I. A. Waitz, "Catalytic combustion systems for microscale gas turbine engines," in *Proceedings of ASME Turbo Expo 2005: Power for Land, Sea and Air*, ASME. Reno-Tahoe, Nevada, USA: ASME, 2005, paper GT2005-68382.

[25] Z. Chea *et al.*, "Three dimensional features of convective heat transfer in droplet-based microchannel heat sinks," *International Journal of Heat and Mass Transfer*, vol. 84, pp. 460–470, 2015.

[26] F. P. Incropera and D. P. DeWitt, *Fundamentals of Heat and Mass Transfer*, 6th ed. Hoboken, NJ: John Wiley & Sons, 2007.

[27] W. Massman, "A review of the molecular diffusivities of H_2O, CO_2, CH_4, CO, O_3, SO_2, NH_3, N_2O, NO, and NO_2 in air, O_2 and N_2 near STP," *Atmospheric Environment*, vol. 32, no. 6, pp. 1111–1127, 1998.

[28] S. B. Pope, "The vanishing effect of molecular diffusivity on turbulent dispersion: implications for turbulent mixing and the scalar flux," *Journal of Fluid Mechanics*, vol. 359, pp. 299–312, 1998.

[29] S. B. Pope, "Turbulent flows," *Measurement Science and Technology*, vol. 12, no. 11, pp. 2020–2021, 2001.

[30] P. E. Dimotakis, "Turbulent mixing," *Annual Review of Fluid Mechanics*, vol. 37, pp. 329–356, 2005.

[31] H. Tennekes and J. L. Lumley, *A First Course in Turbulence*. MIT Press, 1972.

[32] A. Hewes and L. Mydlarski, "Quantifying mixing in flows transporting multiple scalars: New mixing metrics describing three-scalar mixing," *International Journal of Heat and Fluid Flow*, vol. 116, p. 109934, 2025.

[33] P. V. Danckwerts, "The definition and measurement of some characteristics of mixtures," *Applied Scientific Research, Section A*, vol. 3, pp. 279–296, 1952.

[34] K. Kling and D. Mewes, "Two-colour laser induced fluorescence for the quantification of micro- and macromixing in stirred vessels," *Chemical Engineering Science*, vol. 59, no. 7, pp. 1523–1528, 2004.

[35] J. Aubin *et al.*, "Characterization of the mixing quality in micromixers," *Chemical Engineering & Technology*, vol. 26, pp. 1262–1270, 2003.

[36] D. S. Liscinsky, B. True, and J. D. Holdeman, "Crossflow mixing of noncircular jets," in *33rd Aerospace Sciences Meeting and Exhibit*, American Institute of Aeronautics and Astronautics. Reno, Nevada, USA: NASA Lewis Research Center, 1996, p. 13, AIAA Paper 95-0732, NASA-TM-106865.

[37] T. F. Fric, "Effects of fuel-air unmixedness on NO_x emissions," *Journal of Propulsion and Power*, vol. 9, no. 5, pp. 708–713, 1993.

[38] L. Gevorkyan *et al.*, "Transverse jet mixing characteristics," *Journal of Fluid Mechanics*, vol. 790, pp. 237–274, 2016.

[39] R. Y. Wiranegara *et al.*, "Numerical study of radiation and fuel–air unmixedness on the performance of a dry low NO_x combustor," *ASME Open Journal of Engineering*, vol. 1, p. 011051, 2022.

[40] A. C. Rossitto, "Villarrica volcano in chile," 2024, free to use (Pexels Licence). [Online]. Available: https://www.pexels.com/photo/villarrica-volcano-in-chile-25526004/

[41] Pexels, "Industrial chimneys emitting smoke in rural landscape," 2025, free to use (Pexels Licence). [Online]. Available: https://www.pexels.com/photo/industrial-chimneys-emitting-smoke-in-rural-landscape-35074435/

[42] T. F. Fric and A. Roshko, "Vortical structure in the wake of a transverse jet," *Journal of Fluid Mechanics*, vol. 279, p. 1–47, 1994.

[43] S. Megerian *et al.*, "Transverse-jet shear-layer instabilities. Part 1. Experimental studies," *Journal of Fluid Mechanics*, vol. 593, pp. 93–129, 2007.

[44] Y. Kamotani and I. Greber, "Experiments on a turbulent jet in a cross flow," *AIAA Journal*, vol. 10, pp. 1425–1429, 1972.

[45] S. D. Peterson and M. W. Plesniak, "Evolution of jets emanating from short holes into crossflow," *Journal of Fluid Mechanics*, vol. 503, pp. 57–91, 2004.

[46] B. Morton and A. Ibbetson, "Jets deflected in a crossflow," *Experimental Thermal and Fluid Science*, vol. 12, no. 2, pp. 112–133, 1996.

[47] R. M. Kelso and A. J. Smits, "Horseshoe vortex systems resulting from the interaction between a laminar boundary layer and a transverse jet," *Physics of Fluids*, vol. 7, no. 1, pp. 153–158, 1995.

[48] V. Nair *et al.*, "Near-field evolution and scaling of shear layer instabilities in a reacting jet in crossflow," *Journal of Fluid Mechanics*, vol. 960, p. A13, 2023.

[49] R. J. Margason, Ed., *Fifty years of jet in cross flow research*, April 1993.

[50] S. H. Smith and M. G. Mungal, "Mixing, structure and scaling of the jet in crossflow," *Journal of Fluid Mechanics*, vol. 357, p. 83–122, 1998.

[51] S. Muppidi and K. Mahesh, "Study of trajectories of jets in crossflow using direct numerical simulations," *Journal of Fluid Mechanics*, vol. 530, p. 81–100, 2005.

[52] T. H. New, T. T. Lim, and S. C. Luo, "Effects of jet velocity profiles on a round jet in cross-flow," *Experiments in Fluids*, vol. 40, no. 6, pp. 859–875, 2006.

[53] S. Muppidi and K. Mahesh, "Direct numerical simulation of round turbulent jets in crossflow," *Journal of Fluid Mechanics*, vol. 574, p. 59–84, 2007.

[54] J. D. Holdeman, "Mixing of multiple jets with a confined subsonic crossflow," *Progress in Energy and Combustion Science*, vol. 19, no. 1, pp. 31–70, 1993.

[55] A. R. Karagozian, "The jet in crossflow," *Physics of Fluids*, vol. 26, no. 10, p. 101303, 2014.

[56] C. Wang *et al.*, "Study on the effects of stroke ratio, velocity ratio, and duty cycle on the diffusion characteristics of pulsed buoyant jets in crossflow," *Ocean Engineering*, vol. 315, p. 119893, 2025.

[57] M. Taherian and A. Mohammadian, "Buoyant jets in cross-flows: Review, developments, and applications," *Journal of Marine Science and Engineering*, vol. 9, no. 1, 2021.

[58] D. Getsinger, "Shear layer instabilities and mixing in variable density transverse jet flows," Ph.D. dissertation, University of California, Los Angeles, 2012.

[59] R. F. Davey and A. Roshko, "The effect of a density difference on shear-layer instability," *Journal of Fluid Mechanics*, vol. 53, no. 3, p. 523-543, juin 1972.

[60] K. C. Kim, S. K. Kim, and S. Y. Yoon, "PIV measurements of the flow and turbulent characteristics of a round jet in crossflow," *Journal of Visualization*, vol. 3, no. 2, pp. 157–164, 2000.

[61] B. A. Haven and M. Kurosaka, "Kidney and anti-kidney vortices in crossflow jets," *Journal of Fluid Mechanics*, vol. 352, pp. 27–64, 1997.

[62] T. H. New, T. T. Lim, and S. C. Luo, "Elliptic jets in cross-flow," *Journal of Fluid Mechanics*, vol. 494, p. 119–140, 2003.

[63] Z. M. Moussa, J. W. Trischka, and S. Eskinazi, "The near field in the mixing of a round jet with a cross-stream," *Journal of Fluid Mechanics*, vol. 80, no. 1, p. 49–80, 1977.

[64] D. R. Getsinger *et al.*, "Structural and stability characteristics of jets in crossflow," *Journal of Fluid Mechanics*, vol. 760, pp. 342–367, 2014.

[65] J. Davitian *et al.*, "Strategic control of transverse jet shear layer instabilities," *AIAA Journal*, vol. 48, no. 9, pp. 1968–1980, 2010.

[66] B. Zang and T. H. New, "Near-field dynamics of parallel twin jets in cross-flow," *Physics of Fluids*, vol. 29, no. 3, p. 035103, 2017.

[67] F. Roger *et al.*, "Numerical investigation on the reactive gas mixing through interaction between twin square jets side-by-side and a crossflow," *Chemical Engineering Journal*, vol. 238, pp. 45–55, 2014.

[68] J. D. Holdeman, D. S. Liscinsky, and D. B. Bain, "Mixing of multiple jets with a confined subsonic crossflow: Part II – opposed rows of orifices in rectangular ducts," NASA Lewis Research Center / United Technologies / CFD Research Corporation, Cleveland, OH; East Hartford, CT; Huntsville, AL, NASA Technical Memorandum / ASME Paper 97-GT-439 NASA TM-107461, 1997.

[69] J. D. Holdeman, J. R. Clisset, and J. P. Moder, "Spreadsheet calculations of jets in crossflow: opposed rows of inline and staggered round holes," *Heat and Mass Transfer*, vol. 48, pp. 413–424, 2011.

[70] E. J. Gutmark, I. M. Ibrahim, and S. Murugappan, "Dynamics of single and twin circular jets in cross flow," *Experiments in Fluids*, vol. 50, no. 3, pp. 653–663, 2011.

[71] D. Yu, M. S. Ali, and J. H. W. Lee, "Multiple tandem jets in cross-flow," *Journal of Hydraulic Engineering*, vol. 132, no. 9, pp. 971–982, 2006.

[72] P. J. Kristo and M. L. Kimber, "Time-resolved particle image velocimetry measurements of a tandem jet array in a crossflow at low velocity ratios," *Experiments in Fluids*, vol. 62, p. 67, 2021.

[73] A. C. H. Lai and J. H. W. Lee, "Multiple tandem jet interaction in a crossflow," in *Proceedings of the 9th International Conference on Hydrodynamics*, Shanghai, China, 2010, pp. 639–643.

[74] Z. Li, W. Huai, and Z. Qian, "Study on the flow field and concentration characteristics of the multiple tandem jets in crossflow," *Science China Technological Sciences*, vol. 55, no. 10, pp. 2778–2788, 2012.

[75] G. Vignat, D. Durox, and S. Candel, "The suitability of different swirl number definitions for describing swirl flows: Accurate, common and (over-) simplified formulations," *Progress in Energy and Combustion Science*, vol. 89, p. 100969, 2022.

[76] T. Watanabe *et al.*, "Direct numerical simulations of multiple swirling jets issued into a crossflow," *Physics of Fluids*, vol. 37, 2025.

[77] S. A. Ahmed and R. M. C. So, "Characteristics of air jets discharging normally into a swirling crossflow," *AIAA Journal*, vol. 25, no. 3, pp. 429–435, 1987.

[78] A. Terzis *et al.*, "Swirl jet and crossflow interaction at low velocity ratios and incrompressible flows," in *Proceedings of the 9th European Conference on Turbomachinery Fluid Dynamics & Thermodynamics (ETC09)*, Istanbul, Turkey, 2011, paper ID: ETC2011-249.

[79] O. Jobin, "Small-scale experiments for the development and characterization of novel hybrid rocket fuel systems," Ph.D. dissertation, Polytechnique Montréal, Montréal, Canada, 2023.

[80] The Engineering ToolBox. (2018) Air - diffusion coefficients of gases in excess of air. [Online]. Available: https://www.engineeringtoolbox.com/air-diffusion-coefficient-gas-mixture-temperature-d_2010.html

[81] TOPAS GmbH. DEHS seeding particles – product information. TOPAS GmbH.

[82] X. Paredes *et al.*, "Experimental density and viscosity measurements of di(2ethylhexyl)sebacate at high pressure," *The Journal of Chemical Thermodynamics*, vol. 44, no. 1, pp. 38–43, 2012.

[83] S. Scharnowski and C. J. Kähler, "Particle image velocimetry - classical operating rules from today's perspective," *Optics and Lasers in Engineering*, vol. 135, p. 106185, 2020.

[84] B. McKeon *et al.*, *Velocity, vorticity, and mach number*, ser. Springer Handbooks. Springer, 2007, pp. 215–471, publisher Copyright: © Springer-Verlag 2007.

[85] V. K. Michalis *et al.*, "Rarefaction effects on gas viscosity in the knudsen transition regime," *Microfluidics and Nanofluidics*, vol. 9, no. 4, pp. 847–853, 2010.

[86] N. Rembaut and V. Lago, "Experimental study on the aerodynamics of an oriented cube in supersonic flow at different knudsen numbers," *Acta Astronautica*, vol. 239, pp. 657–671, 2026.

[87] R. W. Barber and D. R. Emerson, "Challenges in modeling gas-phase flow in microchannels: From slip to transition," *Heat Transfer Engineering*, vol. 27, no. 4, pp. 3–12, 2006.

[88] E. Cunningham, "On the velocity of steady fall of spherical particles through fluid medium," *Proceedings of the Royal Society of London. Series A, Containing Papers of a Mathematical and Physical Character*, vol. 83, no. 563, pp. 357–365, 03 1910.

[89] C. N. Davies, "Definitive equations for the fluid resistance of spheres," *Proceedings of the Physical Society*, vol. 57, no. 4, p. 259, jul 1945.

[90] J. Horwitz and A. Mani, "Accurate calculation of stokes drag for point–particle tracking in two-way coupled flows," *Journal of Computational Physics*, vol. 318, pp. 85–109, 2016.

[91] C. Tropea *et al.*, *Springer handbook of experimental fluid mechanics*. Springer, 2007, vol. 1.

[92] N. T. Ouellette *et al.*, "An experimental study of turbulent relative dispersion models," *New Journal of Physics*, vol. 8, p. 109, 2006.

[93] V. Duke-Walker, B. J. Musick, and J. A. McFarland, "Experiments on the breakup and evaporation of small droplets at high weber number," *International Journal of Multiphase Flow*, vol. 161, p. 104389, 2023.

[94] TOPAS GmbH, "Company information and quality management certification (DIN EN ISO 9001, 12 100 11908 TMS)," 2019.

[95] H. Nobach and E. Bodenschatz, "Limitations of accuracy in PIV due to individual variations of particle image intensities," *Experiments in Fluids*, vol. 47, no. 1, pp. 27–38, 2009.

[96] J. W. Elmer, A. T. Teruya, and G. Gibbs, "Power density distributions in electron beams," *Welding Journal*, 2022, lLNL-JRNL-842038.

[97] Federal Aviation Administration, "FAA Order JO 7400.2L: Procedures for Handling Airspace Matters," 2017, effective April 27, 2017. Chapter 29: Outdoor Laser Operations, Section 1, Paragraph 29-1-5.

[98] K. Grayson *et al.*, "Laser light sheet profile and alignment effects on PIV performance," in *18th international symposium on applications of laser and imaging techniques to fluid mechanics, Lisbon, Portugal*, 2016, pp. 4–7.

[99] K. Grayson *et al.*, "Impact of mismatched and misaligned laser light sheet profiles on PIV performance," *Experiments in Fluids*, vol. 59, no. 1, p. 2, 2017.

[100] C. E. Willert and M. Gharib, "Digital particle image velocimetry," *Experiments in Fluids*, vol. 10, no. 4, pp. 181–193, 1991.

[101] J. F. Reinoso, C. León, and J. Mataix, "Estimating horizontal displacement between dems by means of particle image velocimetry techniques," *Remote Sensing*, vol. 8, p. 14, 12 2015.

[102] J. Westerweel, "Fundamentals of digital particle image velocimetry," *Measurement Science and Technology*, vol. 8, no. 12, pp. 1379–1392, 1997.

[103] A. Pizarro *et al.*, "Identifying the optimal spatial distribution of tracers for optical sensing of stream surface flow," *Hydrology and Earth System Sciences*, vol. 24, no. 11, pp. 5173–5185, 2020.

[104] J. Westerweel, "Fundamentals of digital particle image velocimetry," *Measurement Science and Technology*, vol. 8, no. 12, p. 1379, dec 1997.

[105] Altair Engineering, Inc., "Basic boundary layer theory," *Altair Engineering, Inc. website*, 2026.

[106] P. Versailles and J. M. Bergthorson, "Optimized laminar axisymmetrical nozzle design using a numerically validated thwaites method," *Journal of Fluids Engineering*, vol. 134, no. 10, p. 101203, 2012.

[107] M. Tyagi and S. Acharya, "Large eddy simulations of jets in crossflow: Free-stream turbulence effects," in *Proceedings of the 1999 3rd ASME/JSME Joint Fluids Engineering Conference, FEDSM'99*, San Francisco, California, USA, Jul. 1999.

[108] L. Fischer and M. Pfitzner, "Impact of external turbulence on film cooling designs using large eddy simulations," *International Journal of Heat and Mass Transfer*, vol. 217, p. 124623, 2023.

[109] K. Taira *et al.*, "Modal analysis of fluid flows: An overview," *AIAA Journal*, vol. 55, no. 12, pp. 4013–4041, 2017.

[110] L. Gevorkyan, "Structure and mixing characterization of variable density transverse jet flows," Ph.D. dissertation, University of California, Los Angeles, 2015.